Observationally-based Constraints of Future Climate Projections of Carbon Cycle Feedbacks and the Shift in the Austral Jet Stream

Sabrina Wenzel

Oberpfaffenhofen 2016

Observationally-based Constraints of Future Climate Projections of Carbon Cycle Feedbacks and the Shift in the Austral Jet Stream

Sabrina Wenzel

Dissertation
an der Fakultät für Physik
der Ludwig–Maximilians–Universität
München

vorgelegt von
Sabrina Wenzel
aus Weimar

München, im Dezember 2015

Erstgutachter: PD Dr. Veronika Eyring

Zweitgutachter: Prof. Dr. George Craig

Tag der mündlichen Prüfung: 5. Februar 2016

Contents

Kurzfassung

Der anthropogene Klimawandel wird vor allem durch die Emissionen von Treibhausgasen (GHG) verursacht, welche den Energiehaushalt der Erde ändern. Der Anstieg in GHG- Konzentrationen verstärkt nicht nur den strahlungsgetriebenen Treibhauseffekt, sondern beeinflusst auch die atmosphärische Zirkulation sowie biogeochemische Kreisläufe. Rückkopplungsprozesse von biogeochemischen Kreisläufen können dabei die Klimaerwärmung verstärken oder abschwächen. Aktuelle Erdsystemmodelle (ESMs) aus der fünften Phase des Coupled Model Intercomparison Project (CMIP5), beinhalten solche biogeochemische Prozesse. Diese ermöglichen die Untersuchung von biogeochemischen und Klima Feedbacks des Erdsystems. Diese Feedbacks in Klimaprojektionen unterliegen jedoch großen Unsicherheiten, da das Verständnis der zugrundeliegenden Prozessen und deren Repräsentation in ESMs oft noch unzureichend ist. Das Ziel dieser Arbeit ist zu untersuchen wie beobachtbare Eigenschaften des aktuellen Klimas genutzt werden können, um Unsicherheiten in ausgesuchten Rückkopplungsprozesse zu reduzieren.

Um den Zusammenhang zwischen der Klimasensitivität auf anthropogen verursachte Klimaänderungen und beobachtbare Eigenschaften des globalen Klimasystems besser zu verstehen, wurde die relativ neue Methode der so genannten *Emergent Constraints* verwendet. Emergent Constraints beschreiben dabei Zusammenhänge zwischen einem Aspekt der simulierten Erdsystemsensitivität und einem beobachtbaren Trend oder Variation des aktuellen Klimas. Diese Methode wurde in dieser Arbeit verwendet um Feedbacks im Kohlenstoffkreislauf sowie Änderungen in der Position des Südhemisphären (SH) Jets auf anthropogene Klimaänderungen genauer zu bestimmen. Dafür wurden neue Diagnostiken entwickelt und in das Earth System Model Evaluation Tool (ESMValTool) implementiert.

Diese erste Studie nutzt Beobachtungsdaten, um den Kohlenstofkreislauf-Klima- Feedback genauer zu bestimmen und wurde in *Journal of Geophysical Research* 2014 publiziert. In den meisten Klimaprojektionen führt eine Erwärmung des Klimas zu einer geringeren Aufnahmefähigkeit von atmosphärischem Kohlenstoff Dioxid (CO_2) durch die terrestrische Senke. Als Ergebnis bleibt mehr CO_2 in der Atmosphäre zurück wo es als GHG klimawirksam ist. Dieser Effekt beschreibt einen positiven Rückkopplungsprozess des Kohlenstoffkreislaufes zur Klimaerwärmung (γ_L) und wird durch den anteiligen Kohlenstoffverlust pro Kelvin Erwärmung quantifiziert, in Einheiten von GtC pro K. Dieser unterliegt jedoch starken Unsicherheiten in Klimaprojektionen des 21. Jahrhunderts. CMIP5 Modelle simulieren den Betrag der tropischen terrestrischen Kohlenstoffsenke, bei ausgeblendeten Klimaeinwirkungen auf den Kohlenstoffkreislauf, im Bereich von 252 ± 112 GtC für eine Verdopplung atmosphärischen CO_2 Konzentrationen. Eine gute Korrelation zwischen dem Kohlenstoffkreislauf-Klima-Rückkopplungsfaktor und der beobachtbaren Sensitivität der interannualen CO_2-Wachstumsrate auf Temperaturschwankungen ermöglicht es die Unsicherheiten in Klimaprojektionen mit Beobachtungen einzuschränken. Die beobachtete Sensitivität (-4.4 ± 0.9 GtC per year and K) reduziert dabei die Unsicherheiten zu -44 ± 14 GtC pro K um mehr als die Hälfte im Vergleich zum Multimodellmittelwert von 49 ± 40 GtC pro K. Die Ergebnisse der ersten Studie implizieren, dass mit einem Temperaturanstieg weniger Kohlenstoff in der terrestrischen Senke gespeichert wird. Dieser Effekt ist im Vergleich zum Multimodellmittel für den neu berechneten Wert geringer, was einen geringeren Anstieg der CO_2 Konzentration durch Klimaerwärmung bedeutet.

Die zweite Studie nutzt Beobachtungsdaten, um den Kohlestofkreislauf-CO_2 Feedback genauer zu bestimmen und ist in der Begutachtung bei *Nature*. Unsicherheiten in der Sensitivität des Landökosystems auf erhöhte atmosphärische CO_2 Konzentrationen tragen zusätzlich zu Unsicherheiten von Klimaprojektionen bei. CMIP5 Modelle mit interaktivem Kohlenstoffkreislauf

simulieren für einen Anstieg der atmosphärischen CO_2 Konzentration eine Erhöhung der terrestrischen Brutto Primärproduktion (GPP). Dieser Düngeeffekt wird jedoch von den CMIP5 Modellen unterschiedlich stark für eine aktuelle atmosphärische CO_2 Konzentration (ca. 400 ppmv) simuliert und ist im Bereich von 7.5 $\pm$ 7 GtC relativ zu vorindustriellen Zeiten. In dieser Studie wurde eine starke Korrelation zwischen dem Düngeeffekt von CO_2 auf GPP in höheren Breiten sowie den Extratropen und der beobachteten Änderung der CO_2 Amplitude im Jahresgangs (0.05 $\pm$ 0.001 ppmv pro ppmv) festgestellt. Mithilfe der Beobachtungen konnte für eine Verdopplung der atmosphärischen CO_2 Konzentrationen ein Düngeeffekt auf GPP in hohen Breiten von 0.14% pro ppmv und für GPP in den extratropischen Regionen von 0.12% pro ppmv ermittelt werden. Durch die Anwendung der beobachtungsbasierte Methode auf den Kohlestofkreislauf-CO_2 Feedback konnte deutliche Verringerung der Unsicherheiten des Düngeeffekts erzielt werden.

Die dritte Studie nutzt Beobachtungen um die Position des SH Jets in Klimaprojektionen genauer zu bestimmen und wurde im *Journal of Climate* 2016 publiziert. Die Zuname stratosphärischen Ozons und den Anstieg von GHG haben einen starken Einfluss auf die SH extratropische Zirkulation was eine Verlagerung der SH Jetposition zur Folge hat. Die mittlere SH Jetposition ist in CMIP Modellen in Bezug auf Beobachtungsdaten zum Äquartor verschoben und die Modelle simulieren eine Verteilung der Jetposition über 10° in der historischen Klimatologie und in Klimaprojektionen. Die Multiple Diagnostik Ensemble Regression (MDER) Methode wurde verwendet um prozess-orientierte Diagnostiken des aktuellen Klimas mit Projektionen der SH Jetposition zu korrelieren. Die MDER Methode wurde auf den Zeitraum 2015 - 2034 angewendet, wo sie aus den 20 Diagnostiken die historische Jetposition als die wichtigste Größe aussucht. Die Methode detektiert den zum Äquator hin verschobenen Bias in der historischen Jetposition und berechnet eine Korrektur von 1.5° südlich für die Vorhersage. Durch die Analyse konnte somit eine Verbesserung zum Ensemblemittelwert und dessen Unsicherheit erzielt werden.

Emergent Constraints, wie sie in dieser Arbeit untersucht wurden, können helfen Modellentwicklungen und Beobachtungen auf Prozesse zu fokussieren, die zur Größenordnung und den Unsicherheiten zukünftiger Klimavorhersagen maßgeblich beitragen.

Abstract

Anthropogenic climate change is mainly driven by increasing greenhouse gas (GHG) concentrations that alter the Earth's energy budget. Higher GHG concentrations not only result in an increase of the radiative forcing but also affect the atmospheric circulation and biogeochemical cycles. Feedbacks of biogeochemical cycles potentially amplify or dampen warming and cooling processes of the climate. State-of-the-art Earth system models (ESMs) participating in the 5th phase of the Coupled Model Intercomparison Project (CMIP5) include biogeochemical components allowing investigations of biogeochemical and climate feedbacks of the Earth system. The magnitude of these feedbacks remains a key uncertainty in climate change projections because of the lack of understanding of the underlying processes and their representation in ESMs. The aim of this work is to study how observable features of the current climate can be used to reduce uncertainties in selected key feedbacks.

In order to constrain the climate's sensitivity to anthropogenic forcings with observations, the relatively new method of emergent constraints is used. Emergent constraints are relationships between some aspect of the simulated Earth system sensitivity and an observable trend or variability in the current climate. This approach is applied in this thesis to constrain carbon cycle feedbacks and the shift in the positions of the Southern Hemispheric (SH) Jet Stream due to anthropogenically forced climate change. New diagnostics are developed and implemented into the Earth System Model Evaluation Tool (ESMValTool).

The first study uses observations to constrain the *carbon cycle-climate feedback* and has been published in a peer-reviewed publication in the *Journal of Geophysical Research* in 2014. In most climate-carbon cycle projections, climate warming reduces the efficiency of carbon dioxide (CO_2) absorption by the land. As a result more of the emitted carbon remains in the atmosphere leading to additional warming, representing a positive carbon cycle-climate feedback. The long-term sensitivity of land carbon storage to future climate warming (γ_L) can be quantified in terms of carbon loss per unit temperature change, usually given in GtC per K, and remains a key uncertainty in climate projections of the 21st century. The CMIP5 models with interactive carbon cycle simulate a spread in the tropical land carbon storage in the order of 252 ± 112 GtC at a doubling of CO_2. A good correlation between the carbon cycle-climate feedback and the (observable) sensitivity of interannual variations in the CO_2 growth rate to temperature variations was found in the CMIP5 models, enabling the projections to be constrained with observations. The observed sensitivity of CO_2 to changes in tropical temperature (-4.4 $\pm$ 0.9 GtC per year and K) narrows the range of the carbon cycle-climate feedback to -44 $\pm$ 14 GtC per K, compared to the unconstrained multi model mean of -49 $\pm$ 40 GtC per K. The results show that with increasing temperature less carbon will be stored in the terrestrial sink, but this carbon cycle-climate feedback is smaller in the constrained ensemble. This implies a less severe increase of atmospheric CO_2 concentrations with climate warming than the increase simulated by the unconstrained model ensemble.

The second study uses observations to constrain the *carbon cycle-CO_2 feedback* and is currently under review in *Nature*. Uncertainties in the vegetation response to rising CO_2 concentrations contribute significantly to the large spread in projections of future anthropogenic CO_2 and hence climate change. CMIP5 models with interactive carbon generally agree that elevated CO_2 will enhance Gross Primary Productivity (GPP), but the magnitude of this fertilization effect varies widely among the models, simulating a GPP increase for current CO_2 concentrations (approx. 400 ppmv) of 7.5 ± 7 GtC relative to pre-industrial times. The projected CO_2 fertilization effect on high-latitude and extra-tropical GPP is found to be correlated with the magnitude of the CO_2 fertilization effect on the amplitude of the CO_2 seasonal cycle (0.05 $\pm$

0.001 ppmv per ppmv), allowing this to be used as an emergent constraint. With the observational constraint the increase in GPP for a doubling of the atmospheric CO_2 concentration is estimated to be in the order of 0.14% per ppmv for high-latitude GPP and 0.12% per ppmv for extra-tropical GPP, respectively. The observational constraint on the carbon cycle-CO_2 feedback therefore significantly reduces the uncertainty and suggests that models overestimate the magnitude of the terrestrial carbon sink.

The third study uses observations to constrain the projected position in the austral jet stream and has been published in a peer-reviewed publication in the *Journal of Climate* in 2015. Stratospheric ozone recovery and increasing GHGs are expected to have a large impact on the SH extratropical circulation shifting the position of the jet stream and thus the SH storm tracks. Models participating in CMIP5 have difficulties in reproducing the observed properties of the austral jet. Typically, the position of the jet is shifted equatorward in the models and 10° spread in their historical and future climatologic meridional position. A Multiple Diagnostic Ensemble Regression (MDER) method was used to relate process-oriented diagnostics of the current climate to projections of future SH jet stream positions. MDER is targeted to constrain near-term (2015-2034) projections of the austral jet position, and selects the historical jet position as the most important of 20 diagnostics. The method essentially recognizes the equatorward bias in the past jet position, and provides a bias correction of about 1.5° southward to future projections. This constitutes an improvement of the projected jet position and also narrows the uncertainty compared to the unweighted multi model mean.

Emergent constraints of the types studied in this thesis can help guiding model development and observations onto processes crucial to the magnitude and spread of future Earth system change.

Chapter 1

Introduction

1.1 Motivation

The Intergovernmental Panel on Climate Change (IPCC) fifth assessment report (AR5, IPCC (2013)) concluded that since 1950 many of the observed changes are unprecedented for long time scales confirming the unequivocal warming of the climate system. "Each of the last decades has been successively warmer at Earth surface than any preceding decade since 1850"(IPCC, 2013), and is likely the warmest period of the last 1400 years on the northern hemisphere (IPCC, 2013). The atmosphere and oceans have warmed, sea-ice and glaciers have diminished and the sea level has risen since the pre-industrial period. Increasing emissions of greenhouse gases (GHGs) are one of the key drivers for anthropogenic climate change. For example the concentration of carbon dioxide (CO_2), which has the largest contribution (1.68 [1.33 to 2.03] W/m^2) to the total anthropogenic radiative forcing (RF) in present days (IPCC, 2013), has increased by about 40% since pre-industrial times (Le Quéré et al., 2013; Ciais et al., 2013). Depending on the degree of climate policy intervention, IPCC AR5 estimates a likely increase of global mean surface temperature of 1.5°C to 4.5°C by the end of the 21st century, relative to 1986-2005 (Collins et al., 2013).

To better understand past, present and future climate change in a multi-model context, the Coupled Model Intercomparison Project (CMIP) was established in 1995 under the auspices of the World Climate Research Programme's (WCRP) Working Group on Coupled Modelling (WGCM). Assessments of model performance from the historical period (1850 - 2005) and quantifications of the causes of the inter-model spread in future projections were made possible with a set of experiments under common protocols and forcings. In IPCC AR5, future climate projections were largely based on simulations performed with ESMs participating in the fifth phase of CMIP (CMIP5, Taylor et al. (2012)), and they also form the basis for studies in this thesis. ESMs are the current state-of-the-art models. These are based on traditional climate models, which include the physical components of the climate system (i.e., atmosphere, ocean, land, and sea ice), extended by including biogeochemical components (e.g., carbon cycle, sulphur cycle, ozone, aerosols, etc.).

The multi-model approach is now a standard technique used by the climate science community and in climate assessment reports to assess projections of specific variables and to derive robust process understanding of the Earth's climate system in combination with observations. However, models differ in terms of resolution and included processes. The spread in model simulations is therefore not a direct measure of the prediction uncertainty (Knutti et al., 2010b,a), but can help to characterize it. A realistic representation of processes is linked to the credibility of model projections and thus could form the basis for performance metrics designed to gauge projection reliability (Knutti et al., 2010a; Stephenson et al., 2012). A longstanding open scientific question is therefore the relation between present-day model performance and future projections. While evaluation of the evolving climate state and processes can be used to build confidence in model fidelity, this does not guarantee the correct response to changed forcing in the future.

The relatively new field of emergent constraint analysis, which refers to the use of observations to constrain a simulated future Earth system feedback, offers the potential to reduce

uncertainty in climate projections. Such relationships were first introduced by Hall & Qu (2006), who observationally-constrained the snow albedo feedback in future climate change scenarios. They found that large inter model variations in the seasonal cycle of the albedo between April and May are well correlated with similarly large inter-model variations in the snow albedo feedback on climatological timescales. The observable variation in the seasonal cycle of the snow albedo is a useful proxy for constraining the unobservable feedback strength to climate warming, as both are driven by the same physical mechanisms on different time scales. Emergent Constraints relate future Earth system sensitivity to an observable trend or variation of the current climate parameter across an ensemble of models. This approach is applied in this thesis to constrain carbon cycle feedbacks and the shift in the Austral Jet Stream due to anthropogenic climate change.

Changes in climate, as described above, alter key aspects of biogeochemical cycles (e.g., carbon cycle, nitrogen cycle, hydrological cycle), which recycle matter through biological, geological and chemical processes (Moses, 2012). Some parts of the system may respond faster than others. This depends on the turnover time of the considered biogeochemical cycle, with feedbacks of these cycles potentially altering warming and cooling processes of future climate (Moss et al., 2010; Cubasch et al., 2013; Flato et al., 2013). The main mechanisms that control the carbon sinks are the carbon uptake by photosynthesis and the release of carbon mainly by microbial activities. The efficiency of these two mechanisms depends on the environmental conditions. Warming enhances the release of carbon, and elevated CO_2 concentrations in the atmosphere stimulate photosynthesis, hence increasing the carbon uptake (Cox et al., 2000; Friedlingstein et al., 2001, 2003). Climate projections show that there is a large uncertainty in the future evolution of these carbon sinks (Friedlingstein et al., 2006; Arora et al., 2013). Uncertainties are largely coming from the terrestrial carbon cycle in response to climate and to atmospheric CO_2 as biological processes of the land ecosystems are less understood than the physical processes in the ocean carbon cycle. The carbon cycle-climate and carbon cycle-CO_2 feedback cannot be directly derived from observations, yet they remain a key uncertainty in climate projections of the 21st century.

Anthropogenic perturbation of the Earth's energy budget is also associated with changes in the atmospheric circulation and hence mass distribution particularly on regional scales (Kidston & Gerber, 2010). For example, a bias in the mid-latitude jet stream has implications for regional precipitation and associated storm tracks and is a driver of heat and carbon uptake into the deep ocean (Swart & Fyfe, 2012). Previous analysis of the southern hemisphere (SH) circulation generally agree that SH storm tracks tend to shift poleward as global mean temperature increases (Bengtsson et al., 2006; Gastineau & Soden, 2009; Chang et al., 2012). Temperature perturbations affecting the SH jet stream not only follows from GHG increases but also from the change of the ozone distribution, by increasing stratospheric temperature due to ozone recovery (Eyring et al., 2007; Son et al., 2010; Kidston & Gerber, 2010). A change in the meridional temperature gradient will change the SH jet stream position (O'Gorman, 2012).

All three studies aim to constrain certain processes that are relevant for the overall Earth system sensitivity.

1.2   Scientific Questions

The goal of this thesis is to use observations to better constrain selected biogeochemical feedbacks that are a major sources of uncertainty in current climate projections. The focus is on three different key uncertainties: (1) the carbon cycle-climate feedback, (2) the carbon cycle-CO_2 concentration feedback, and (3) the response mechanisms of the southern hemispheric summer jet positions to anthropogenically induced temperature perturbations. Specifically, the thesis focuses on answering the following three broad scientific questions:

Q1: How well are selected biogeochemical processes represented in state-of-the-art ESMs that determine the long-term behaviour of climate?

Q2: How can observations be possibly used to narrow down the range of plausible climate projections by providing quantitative observationally-based constraints?

Q3: What are the strengths of selected biogeochemical climate feedbacks?

1.3   Focus and Structure of Thesis

The scientific background for the thesis is given in Chapter 2, including further details on the emergent constraint method (Section 2.3) which was used throughout this thesis to analyze CMIP5 model simulations.

The methodological developments of this thesis were contributed to the first release of the ESMValTool which is documented by Eyring et al. (2015). The main purpose of the ESMValTool is to improve the understanding of climate by focuses on routine benchmarking in model evaluation. This is realized by providing a number of standard namelists addressing different scientific topics, which reproduce specific diagnostics and performance metrics that demonstrated their importance in the evaluation of ESMs in the literature. As part of this thesis, a standard namelist, *namelist_wenzel14jgr.xml*, was included into the ESMValTool (Eyring et al., 2015), reproducing the results published by Wenzel et al. (2014).

The results of the emergent constraint studies for the carbon cycle-climate feedback, the carbon cycle-CO_2 feedback, and the future shift in the Austral Jet Stream are presented in Chapters 3, 4, and 5, respectively. Each of the result chapters is based on a publication, published in 2014 in *Journal of Geographical Research - Biogeoscience* (Wenzel et al. (2014),Chapter 3), under review in *Nature* (Wenzel et al. (2015),Chapter 4), and accepted for publication in *Journal of Climate* (Wenzel et al. (2016),Chapter 5).

Chapters 3 and 4 both focus on the carbon cycle. In Chapter 3 an observation-based emergent constraint for the long-term sensitivity of land carbon storage to future climate warming is presented. This emergent constraint has previously been identified by Cox et al. (2013) across an ensemble of ESMs participating in the Coupled Climate-Carbon Cycle Model Intercomparison Project (C^4MIP). Here, also the mathematical basis for describing this emergent constraint is started to be developed and it is examined whether such a constraint also holds for a new set of eight ESMs participating in CMIP5. In Chapter 4 a new emergent constraint is proposed for large-scale CO_2-fertilization on northern high latitude GPP based on observed changes in the seasonal cycle of atmospheric CO_2 at Point Barrow and Mauna Loa (Keeling et al., 1995; Barichivich et al., 2013; Graven et al., 2013).

In a third study climate projections of the summer austral jet stream position (Chapter 5) were constrained with observationally based process-oriented present-day diagnostics from CMIP5 models. Current Atmospheric-Ocean General Circulation Models (AOGCMs) and ESMs have difficulties in reproducing the SH jet position (Eyring et al., 2013), with the

multi-model mean having an equatorward bias. Two time periods, a near- (2015-2034) and mid-term (2040-2059) climatological mean, were chosen to address the question whether the unweighted multi-model mean of the austral jet projection for a medium GHG concentration scenario can be improved by applying a process-oriented Multiple Diagnostic Ensemble Regression (MDER). To focus MDER on different time periods provides additional insight into which physical processes are important for projections at the mid-term horizon.

The work closes with a summary and outlook in Chapter 6, which provides answers to the main scientific questions outlined in Section 1.2.

Chapter 2

Scientific Background

This chapter provides the scientific background in which the context of the present thesis should be viewed. Section 2.1 gives a general introduction to state-of-the-art climate modelling describing the mechanisms of climate change, current coupled climate models, and sources of uncertainties in model simulations (Section 2.2). The Emergent constraint method is described in Section 2.3, including a literature review on related relevant studies (Section 2.3.2). Sections 2.4 and 2.5 provide an overview of the main mechanisms of the carbon cycle and the SH jet stream and their sensitivity to climate change, respectively.

2.1 Earth System Models, Simulations and Analysis

Although the equations of fluid motions that determine the atmospheric and oceanic behavior are known, numerical coupled climate models are needed to solve them. In addition, many small-scale physical, biological and chemical processes have to be implemented as parametrizations in climate models to provide a more comprehensive representation of the Earth's climate system. In many cases this is not feasible, either because of the lack of computational resources needed to simulate these processes and sufficiently high resolution, or because of the lack of understanding of the mechanisms determining these processes (IPCC FAQ 12.1 Collins et al., 2013).

A large number of alternative model realizations of the climate system exists, differing from each other in terms of resolution, included processes, parameterizations used, but also in terms of external forcings, all leading to different levels of agreement with observations (Knutti et al., 2010a). The complexity of models used in climate research ranges from simple energy balance models to complex ESMs, with the choice of models depending on the scientific question to be answered (Held, 2005; Collins et al., 2006). Within this thesis primarily two groups of climate models are used:

AOGCMs are primarily used to improve the understanding of the dynamics of the physical components of the climate system and to project future climate change under prescribed GHG concentration scenarios and aerosol forcings. These models were the standard climate model in the IPCC Fourth Assessment Report (AR4) and are continued to be used in IPCC AR5 (Flato et al., 2013). Atmospheric GHG concentrations have to be prescribed as input and follow a predefined path within the model simulation. In AOGCMs feedbacks from changes in biogeochemical cycles are not included.

ESMs are an extension of AOGCMs and additionally include the representation of various biogeochemical processes, such as an interactive carbon cycle and ozone chemistry (Flato, 2011). This enables the models to be forced with emissions rather than concentrations of anthropogenic GHGs, allowing interactions between the biogeochemical cycles, the atmosphere and climate. These models are especially useful to investigate how the biogeochemical cycles and thus their responds to climate change (Flato et al., 2013). From these models it is also possible to obtain the Transient Climate Response to cumulated CO_2 Emissions (TCRE), which is a measure of the transient global average surface temperature increase at a given cumulative CO_2 emission since pre-industrial times in units of 1000 PgC (Collins et al., 2013). TCRE is model dependent, as both the climate response and the carbon cycle response vary significantly across models.
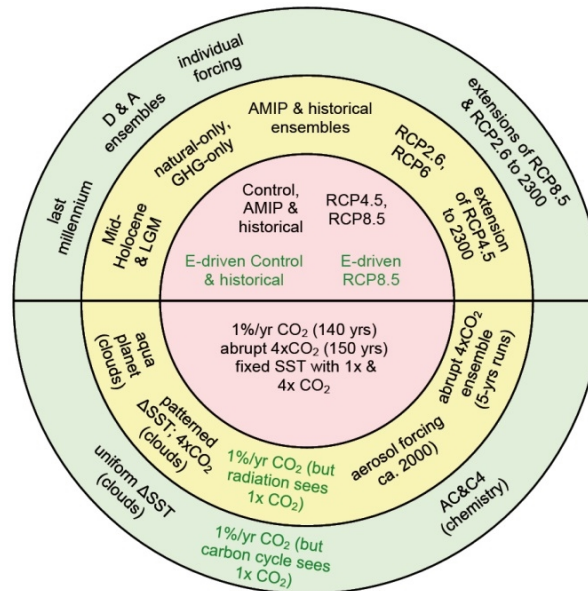
Figure 2.1: Schematic summary of CMIP5 long-term experiments with tier 1 (yellow shading) and tier 2 (green shading) experiments organized around core (red shading) experiments. Experiments with a green font can only be performed by ESMs with included carbon cycle. 'E-driven' experiments relate to emission driven. From Taylor et al. (2012), their Figure 3

The main source of data used in this thesis is the ensemble of climate models that participated in CMIP5 (Taylor et al., 2012) that supported the IPCC AR5 (IPCC, 2013), providing the most recent ensemble of state-of-the-art climate models. The experimental design of CMIP5 includes long-term simulations of the 20th-century climate and future projections (Figure 2.1) as well as simulation experiments on decadal time scales, which are performed by both, AOGCMs and ESMs (not shown).

The advantage of Model Intercomparison Projects (MIP) such as CMIP is that they provide a common set of model experiments following specific protocols and forcings, which are performed by all participating modelling groups. Model simulations that follow common experiments cannot only be compared to observations (e.g., Flato et al., 2013; Bindoff et al., 2013) but also to other models, helping to explore and isolate model differences (e.g., Kirtman et al., 2013; Collins et al., 2013).

The CMIP5 historical simulation covers the time period 1850 to 2005 and includes all known natural and anthropogenic forcings. While natural aerosol forcings (e.g., dust) differ in the models, the historical anthropogenic forcings (e.g., GHGs and aerosols emissions, land use) are identical in the historical model simulations. This allows the CMIP5 ensemble to be relative homogeneous with common time series of forcings (Taylor et al., 2012). For AOGCMs the time evolution of GHGs and aerosol species are prescribed as concentrations rather than emissions, because this group of models does not include chemical and biogeochemical cycles which are necessary to calculate concentrations from emissions. For ESMs, these forcings are prescribed as concentrations or emissions (Hibbard et al., 2007), depending on the simulation experiments. The CO_2, emission driven simulations are denoted as "E-driven simulation" in Figure 2.1.

The historical simulations are extended by four realisations of future Representative Concentration Pathways (RCP), defined by their approximate total radiative forcing in 2100 relative to 1750 (van Vuuren et al., 2011): 2.6 W m-2 for RCP2.6 (van Vuuren et al., 2007); 4.5 W m-2 for RCP4.5 (Clarke et al., 2007; Smith & Wigley, 2006; Wise et al., 2009); 6.0 W m-2 for RCP6.0 (Fujino et al., 2006; Hijioka et al., 2008) and 8.5 W m-2 for RCP8.5 (Riahi et al., 2007). They cover the period between 2006 and 2100. The lowest concentration scenario (RCP2.6),
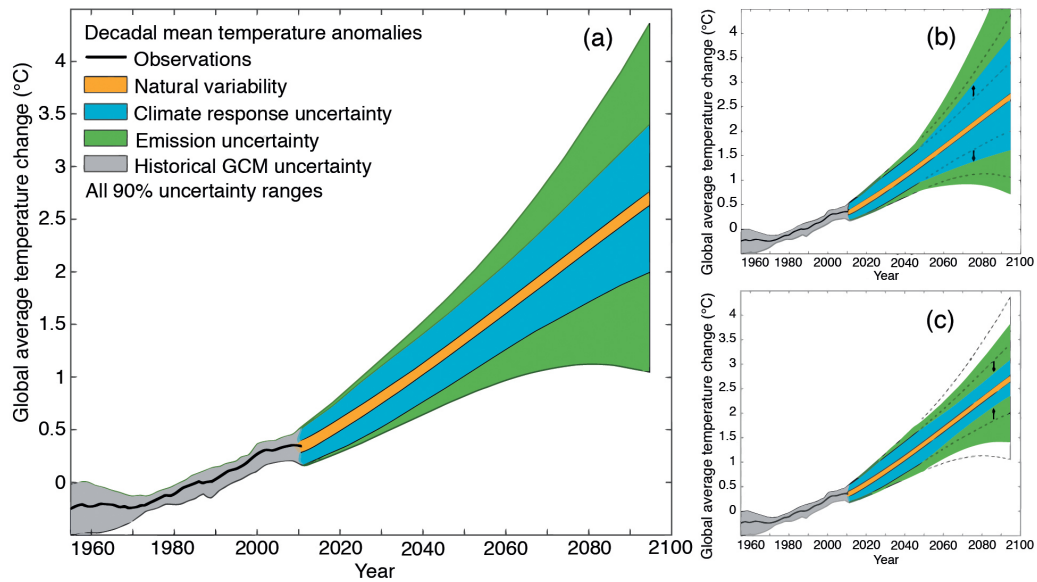
Figure 2.2: Schematic illustrating the different sources of uncertainty on the basis of global averaged temperature change between 1950 and 2100 relative to 1986-2005. From LeTreuth et al. (2013) FAQ1.1, their Figure 1.1.

leading to around 2.6 W m-2 of forcing in 2100, peaks and starts declining before the year 2100 in its radiative forcing. From the two stabilization scenarios RCP4.5 and RCP6.0 only the first stabilizes radiative forcing by the year 2100. The latter as well as the RCP8.5 scenario have a radiative forcing that continues to increase beyond 2100. These four RCP scenarios can be seen as a range of possible future development policies for the 21st century.

Additional experiments are included in the set of CMIP5 simulations addressing specific scientific questions. Of particular interest to this work is the set of idealized simulation experiments, in which the CO_2 concentrations start at conditions of year 1850 (285 ppmv) and then increase by 1% per year. These 1% increase simulations enable investigating uncertainties related to carbon cycle feedbacks. These simulations are only forced by changing CO_2 concentrations, whereas other forcings remain constant at the 1850 level.

2.2 Uncertainties in Climate Projections

Multi-model ensembles are powerful tools to assess uncertainties in future climate projections in various ways. They do not only provide a basis to estimate the projection uncertainty, but also help to determine why similarly forced models produce a large range of climate responses to the imposed forcing (Räisänen, 2007; Taylor et al., 2012).

Projecting climate change is different from forecasting the weather of the next days or weeks since different sources of uncertainty play a role on the longer timescale in future climate change projections. These uncertainties are specific to the climate variable and the region, and can be classified in to three categories as expressed in Figure 2.2 (LeTreuth et al., 2013): *natural variability*, *emission uncertainty*, and *climate response uncertainty*.

Natural Variability (orange shaded area in Figure 2.2) defines a limit how precise models can project climate. This is due to the chaotic nature of climate and is considered to be constant over time. On regional and local scales, the influence of natural variability is much larger than on global scales and its relative importance diminishes when averaging over decadal or longer time scales. Simulations of seasonal and decadal predictions try to address and reduce this source of uncertainty.

The socio-economic development has a large effect on GHG and aerosol precursor emission rates and land use, which defines the second source of uncertainty in climate projections. The increase in GHG emission is mainly a man-made forcing, resulting in increasing concentrations of CO_2, methane (CH_4), nitrous oxide (N_2O) and other GHGs since the industrial revolution. Anthropogenic forcings (e.g., changes in aerosol and GHG concentrations, land use changes) and natural forcings (e.g., volcanic aerosols, and variations in sun activity) change the energy budget of the Earth (Collins et al., 2013). Solar radiance is the Earth heat source, but is not constant over time. The sun has an 11-year sun spot cycle, causing a variation in solar radiance of about 0.1% (Fröhlich & Lean, 2004). GHGs act as the heating system of the Earth. Except for oxygen (O_2) and Ozone (O_3), which absorb solar radiation, the Earth atmosphere is mainly transparent for the short wave (approx. wavelength < 280 nm) radiation resulting in a warming of the Earth's surface. The Earth itself emits this energy in the infrared (approx. wavelength > 280nm) spectrum. Trace gas molecules absorb longwave radiation according to their vibration frequencies and re-radiate it in all directions. This leads to additional warming of the Earth surface. Only 50% of the anthropogenic CO_2 emissions (e.g., by fossil fuel burning) is taken up by natural carbon reservoirs (Le Quéré et al., 2013; Ciais et al., 2013) via terrestrial and oceanic carbon sinks. The rest remains in the atmosphere, where it acts as GHG leading to additional anthropogenic warming of the surface. Aerosols (e.g., dust, smoke and soot) have natural as well as anthropogenic sources and exhibit primary a cooling effect compared with pre-industrial times (e.g., Naik et al., 2013).

To assess *Emission Uncertainties* (green shaded area in Figure 2.2) possible alternative future scenarios that cover alternative evolutions of anthropogenic emissions can be defined and simulated by global climate models. For example, the CMIP5 projections were based on four scenarios, the RCP scenarios as described above (Taylor et al., 2012). By definition these RCP scenarios only represent four out of many possible futures, but give a first estimate of possible emission scenario uncertainty.

The third source of uncertainty arises from the diversity of climate models that differ in terms of spatial resolution, processes included and parametrizations of unresolved processes. Some of these processes can either amplify or reduce the warming effect of climate forcings, and are referred to as climate feedbacks. Feedbacks that have an amplifying effect on an initial warming are positive feedbacks and vice versa. An overview of the main climate feedbacks and their timescales is given in Figure 2.3. Important physical climate feedbacks are the water vapor and cloud feedback, both acting on timescales of days (*Water vapor* in Figure 2.3). Water vapor is the largest contributor to the natural greenhouse effect (Gordon et al., 2013). This feedback is controlled by air temperature, where a temperature increase of one degree of warming leads to additional evapouration of water by 7% (Myhre et al., 2013), thus enhanced absorption and consequently re-emitting more of infrared radiation, and leading to even further temperature increases. Water vapor has a two to three times larger contribution to the natural greenhouse effect than CO_2. In the troposphere water vapor comes mostly from natural sources but to a small degree also from anthropogenic sources such as irrigation and power plant cooling. In the stratosphere the main source of water vapor is the photodissociation of CH_4. Uncertainties arise from the simulation of the hydrological cycle and the cryosphere, where many small scale processes are important (Klein & Hall, 2015).

Also clouds are understood to amplify warming (Boucher et al., 2013), by reflecting or re-emitting radiation (*Clouds* in Figure 2.3). The magnitude of the cloud feedback remains uncertain (Fasullo et al., 2015). The cloud-climate feedback affects the climate system in a number of ways, for example precipitation formation has a net warming effect on the ambient air and water vapour as described above (Bony et al., 2006; Sherwood et al., 2008). Clouds also strongly affect radiation from top and bottom, incoming sunlight is reflected and Earth's infrared radiation trapped by clouds. This feedback mechanism is especially important in the tropics, where the troposphere is deeper and differences between cloud top and surface
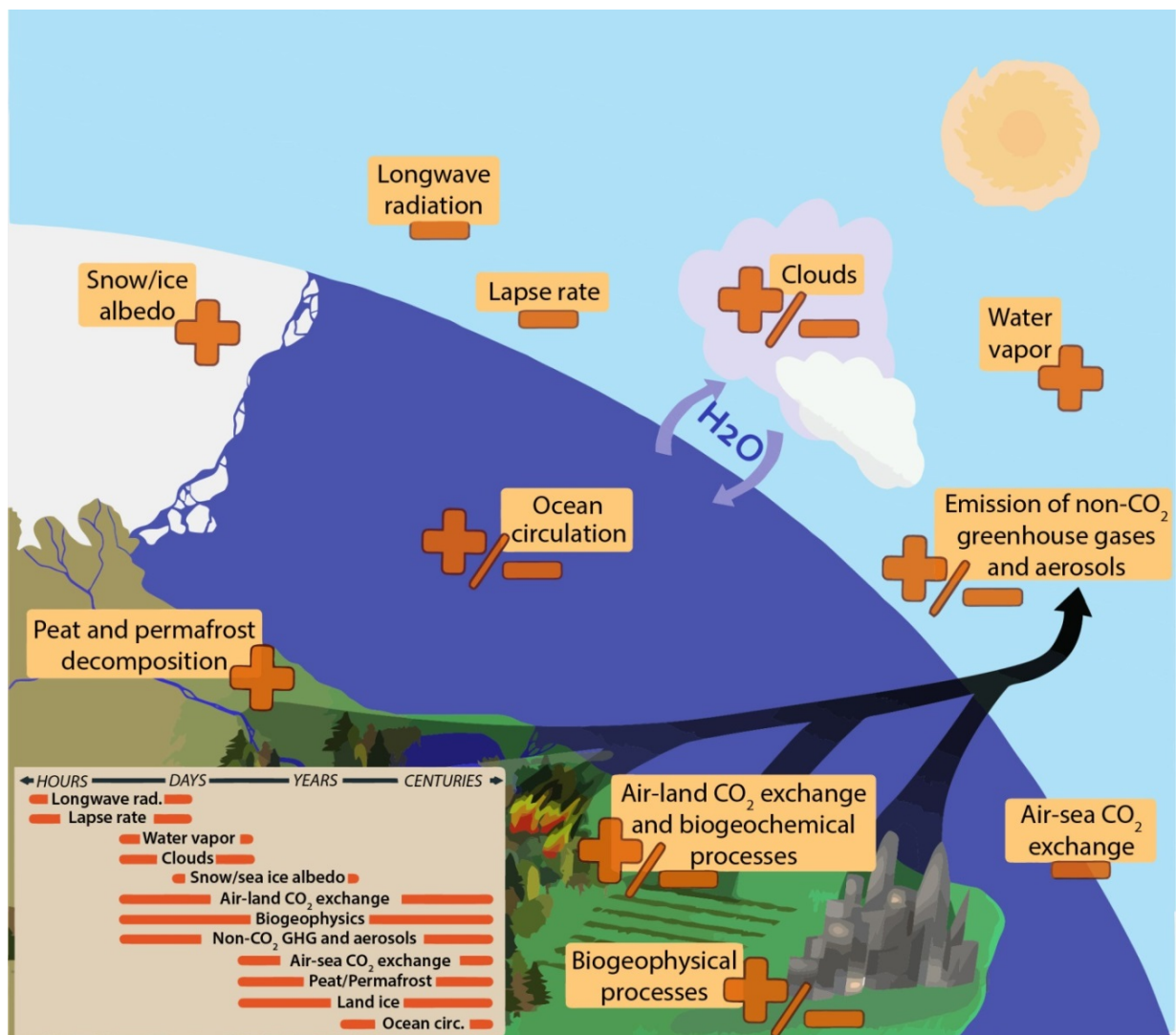
Figure 2.3: Overview of climate feedbacks and their time scales (see box), depict as negative (-) and positive (+) climate feedbacks, that are related to increasing CO2 and temperature. From Cubasch et al. (2013), their Figure 2.1

temperature increases (Tian, 2015). In the mid-latitudes especially the decrease of cloudiness and the shift of clouds associated with poleward shifts of storm tracks leads to increase of surface warming as more solar radiation reaches the Earth's surface (Fasullo & Trenberth, 2012). Uncertainties of the cloud feedbacks arise in general from the amount and reflectivity, as well as compensating effects between other cloud feedback mechanisms.

Another example for feedbacks is the sensitivity of the carbon cycle to anthropogenic climate change (*Air-land* CO_2 *exchange and biogeochemical processes* in Figure 2.3). The terrestrial and oceanic reservoir are absorbing about half of the anthropogenic emitted CO_2 yearly (Ciais et al., 2005). On land, carbon is removed from the atmosphere by plants through photosynthesis, but carbon is also released from land ecosystems, for example soils and organic matter decomposition. Elevated atmospheric CO_2 concentration results in an increased partial pressure of CO_2 in plant leaves, leading to an increased photosynthesis and hence uptake of carbon. Microbial decomposition of soil organic matter is largely temperature dependent, where warming leads to an increase in the release of carbon from soil. These biogeochemical processes take place on timescales of days to centuries (Figure 2.3). There is empirical evidence that the balance between these fluxes going in and out of these reservoirs is altered as the world warms, leading to a faster accumulation of CO_2 in the atmosphere (Cox et al., 2000; Friedlingstein et al., 2001, 2003, 2006; Huntingford et al., 2013; Ciais et al., 2013).
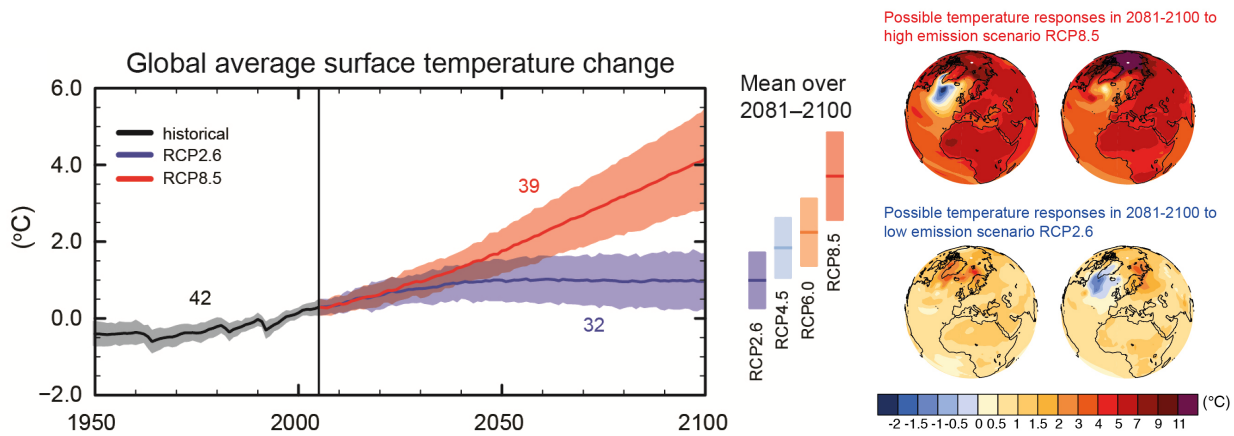
Figure 2.4: (a) Time series from 1950 to 2100 for the change in global annual mean surface temperature relative to 1986 - 2005 simulated by CMIP5 models. Numbers indicate the ensemble size of models. From IPCC (2014) SPM, their Figure 7a. (b) Illustrative maps of surface temperature change at the end of the 21st century (2081-2100 relative to 1986-2005), shown for two different CMIP5 models depict from the highest (RCP8.5) and lowest (RCP2.6) GHG concentration scenario. From Collins et al. (2013) FAQ12.1, their Figure1b.

Although climate models are essentially based on similar basic principles, limited computation power and understanding of physical, chemical and biological processes in the climate system make parametrizations necessary (Knutti et al., 2010a). The magnitude of *Climate Response Uncertainty* depends on the model improvements from one generation of climate models to the next. The uncertainty may increase (Figure 2.2b) if a new process is found to be important and included for the first time in the next generation of models. For example, in the CMIP5 ensemble, not all ESMs that included a carbon cycle also included a nitrogen cycle. Nitrogen limitation leads to a reduction of the land carbon uptake. Models that account for nitrogen limitations therefore simulate a larger atmospheric CO_2 growth and climate change than equivalent models neglecting this process (Thornton et al., 2009, 2007; Zaehle et al., 2010). Such newly included processes possibly enlarge the model ensemble spread of atmospheric CO_2 concentration projections. On the other hand the climate response uncertainty may decrease (Figure 2.2b) with model improvements (e.g., inclusion of new important processes). It can also decrease with the help of observational constraints which is the main topic of this thesis.

As an example for emission and climate response uncertainty, Figure 2.4 shows the global average and spatial distribution of surface temperature averaged over more than 30 CMIP5 models for two different RCPs following different GHG concentration scenarios. Figure 2.4a illustrates the possible evolution and range of projected global mean surface temperature in scenarios with high (RCP8.5) and low (RCP2.6) CO_2 concentrations. The figure indicates an increase of model uncertainty over time in each of the RCPs. From each ensemble two representative models are chosen in Figure 2.4b, illustrating the modeled response to different GHG forcings. Both models are simulating a different spatial distribution of surface temperature change even though forced with the same GHG concentration pathway.

However, such multi-model ensembles do not necessarily represent a systematically sampled group of models (Knutti et al., 2013). Because climate models evolve from previous versions, and are not developed completely new, each generation of models tends to be rather similar to their predecessors. This is because modelling groups share successful code of submodules and parametrizations, hence such a model ensemble more likely represents an 'ensemble of opportunity' (Knutti et al., 2010a; Stephenson et al., 2012), which has to be considered when interpreting such ensembles of models.

2.3   Emergent Constraints

2.3.1   Methods

Method to constrain the carbon cycle feedbacks

A method to relate both, observational variations or trends and Earth system sensitivity, is the so called *Emergent Constraints* method, which is based on statistical relationships between models' simulation of the historical variations or trends and their future projections (Allen & Ingram, 2002; Hall & Qu, 2006; Bracegirdle & Stephenson, 2013). The key idea is to use the models to establish a relationship between the historical observable and the future projection - i.e. the regression illustrated by the red line in Figure 2.5 - and use this relationship to estimate the future projection based on historical observations.

More generally, emergent constraints are relationships across an ensemble of models, between some aspect of the Earth system response and an observable trend or variation in the current climate (Knutti et al., 2010a). If there is a robust relationship supported by a physical explanation between the future projections of a target variable (e.g., some feedback of the carbon cycle) and a proxy diagnostic of the current or past climate, one can use observations to make an improved forecast. The term emergent constraints consists of two parts; emergent: because it emerges of from an ensemble of climate models; and constraint: because it enables on observable variation or trend to constrain the estimate of the future response of a component of the Earth system in the real world. The goal and challenge of this method is to find an observable variation or trend which expresses the same physical behavior as the unobservable Earth system sensitivity which shall be constraint. The emergent constraint is therefore physically motivated and is based on an observable diagnostic which uncertainty is smaller than the inter-model spread (Fasullo et al., 2015; Klein & Hall, 2015). In that sense, the method of the emergent constraint helps to better understand the sensitivity of the Earth system and the underlying processes that force future climate projections.

In this thesis, the method of emergent constraints is applied to constrain carbon cycle feedbacks. The corresponding results are discussed in Chapters 3 and 4.

Method to constrain the future austral jet position [1]

In a similar vein, the emergent constraint method described in the previous section can also be applied to make an improved prediction on climate projections using multiple linear regression. The projection of a specific target variable may not depend only on one observable variable or trend. That is, because of multiple forcings and processes may be important to the target variable. Karpechko et al. (2013) developed the MDER method to show how Antarctic total column ozone projections in October are related to observable process-oriented present-day diagnostics in chemistry-climate models. The method identified key biases in model transport processes, and used them to establish future ozone projections with higher precision compared to the unweighted Multi Model Mean (uMMM) projection. MDER is similar to the method described in Section 2.3, but slightly different in that regard that it looks at correlations between process-oriented diagnostics and a future quantity, why it is described separately here. If there is a robust linear relationship between future projections of a target variable (e.g., the position of the austral jet or October Antarctic total column ozone as in Karpechko et al. (2013)) and a diagnostic of the present-day climate, one can use observations to make an improved forecast, as illustrated schematically in Figure 2.5. The key idea is the same as described in Section 2.3.

---

[1]The contents of this section appears in similar form in the study of Wenzel et al. (2015b) Constraining Future Summer Austral Jet Stream Positions in the CMIP5 Ensemble by Process-oriented Multiple Diagnostic Regression. J. Clim.
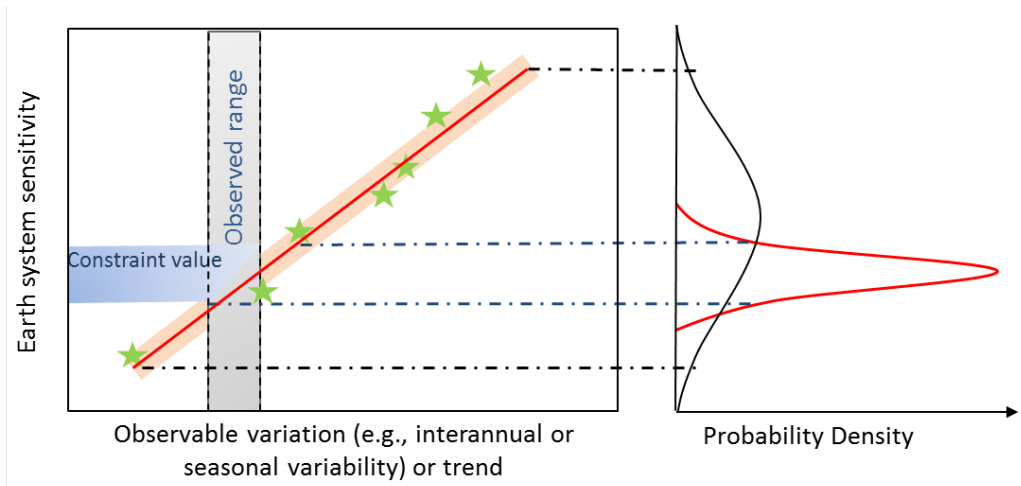
Figure 2.5: Schematic diagram illustrating the method of the Emergent Constraint. Each star represents (hypothetical) output from different climate models, comparing a model's performance on a diagnostic based on the historical scenario integration (x-axis) with its future Earth system sensitivity or climate projection (y-axis). The linear relationship between the past diagnostic and future projection illustrates an emergent constraint, which is quantified by linear regression (red line). The linear relationship can be used to estimate the future projection based on the observations of the past diagnostic, as marked by the black arrows. Uncertainty in the new projection (blue shading) arises from two sources: uncertainty in the observational constraint (gray shading) and uncertainty in the linear regression (red shading).

The method thus depends (1) on the existence of robust correlations between key processes and the future variable to be projected and (2) the ability to constrain the relationships with available observations. Also the uncertainty in the observational constraint is taken into account (Figure 2.5). However, this uncertainty only relates to the interannual variability.

As emphasized by Bracegirdle & Stephenson (2012), one must be wary of spurious relationships between the past climatology and future projections. This danger of over-fitting grows larger when considering multiple diagnostics at once, and the main difficulty of the MDER method stems from the need to systematically reject spurious relationships and avoid using redundant information, i.e. cases where the same effective emergent constraint is captured by two different diagnostics. Cross validation is used to help filter out spurious relationships and redundancy is avoided by a step-wise regression procedure, as detailed below.

More formally, the method exploits relationships between a climate response variable y and a set of m diagnostics of the present climate x_j, where $j = 1, 2, \ldots m$. For a set of n climate models, the multiple linear regression of the relation can be written in matrix form:

$$\mathbf{Y} = \mathbf{1}\,\beta_0 + \mathbf{X}\,\boldsymbol{\beta} + \boldsymbol{\epsilon} \tag{2.1}$$

where $\mathbf{Y} = \{y_1, y_2, \ldots y_n\}^T$ is the vector of the climate response variables in the model projection (a superscript T denotes the transpose); $\mathbf{1} = \{1, 1, \ldots 1\}^T$ is a column-vector of size n; $\mathbf{X} = \begin{pmatrix} x_{1,1} & x_{1,2} & \ldots & x_{1,m} \\ x_{2,1} & x_{2,2} & \ldots & x_{2,m} \\ \ldots & \ldots & \ldots & \ldots \\ x_{n,1} & x_{n,2} & \ldots & x_{n,m} \end{pmatrix}$ is the matrix of diagnostics and $\boldsymbol{\epsilon}$ is the vector of independent random variables of size n representing the uncertainty in the projections. The parameters β_0 and $\boldsymbol{\beta}$ of the multiple regression represented in Equation (2.1), where $\boldsymbol{\beta}$ is a column-vector of size m, are estimated by a least square fit. A key additional assumption for MDER is that the relationship defined by Equation (2.1) and parameters estimated from the model ensemble simulations holds also for the true climate - and not just for the climate models. Under this

assumption Equation (2.1) can be used to estimate the climate response $\hat{y}_0$, given the vector of observed diagnostics $\hat{\mathbf{X}}_0$:

$$\hat{y}_0 = \hat{\beta}_0 + \hat{\mathbf{X}}_0^T \hat{\boldsymbol{\beta}} \tag{2.2}$$

where the hatted quantities indicate that a variable is the best fit determined from the regression analysis.

The selection of the diagnostics x_j in MDER is done in a two-step process. First, physical processes which are expected to influence the climate response y must be identified. A set of diagnostics representing these processes are selected based on expert judgment. This step is necessarily subjective, and Eyring et al. (2005) and Bracegirdle et al. (2015) provide practical examples of diagnostic selections. Second, a stepwise regression procedure von Storch & Zwiers (1999) is applied in order to only choose a subset of diagnostics for the multiple linear regression which contribute significantly to intermodel variation in the climate response y. In the stepwise regression diagnostics are iteratively added to and removed from the regression model depict by Equation (2.1). This will continue until the regression sum of squares is not further increased by adding more diagnostics according to an F-test, with the level of significance chosen in this study being p = 0.05. A more detailed description of the stepwise regression can be found in von Storch & Zwiers (1999).

An example of a model weighting strategy which uses only the first (subjective) step for diagnostic selection is giving by Waugh & Eyring (2008). However, as discussed by Räisänen et al. (2010), Bracegirdle & Stephenson (2012) and Karpechko et al. (2013), it is not necessary that all the subjectively selected diagnostics play a discernible role in climate response, or contribute significantly to intermodel spread in the response. As a result, the statistical model in Equation (2.1) may become overfitted and not necessarily provide the best estimate of the climate response.

For example Karpechko et al. (2013) initially selected 19 diagnostics known to be relevant to stratospheric ozone under present day conditions; but only 1 to 4 diagnostics, depending on the forecast period, were selected by the stepwise algorithm during the second step (i.e., m was $\leq$ 4 in their study). Similarly Räisänen et al. (2010) found that up to 4 diagnostics could be added to the regression model before overfitting problems started to emerge. Räisänen et al. (2010) applied a multiple regression model, as in Equation (2.1), to diagnose the climate response in surface air temperature, but used ad-hock diagnostics which were not necessarily directly related to physically relevant processes.

In order to assess whether projections following from the MDER algorithm may be susceptible to overfitting, a cross-validation strategy (Michaelsen, 1987) can be performed. In the field of weather forecasting, one can test a predictive model against subsequent observations, but clearly we cannot wait to verify climate model projections. Thus cross-validation is performed in a "pseudo reality" where, one model at a time is chosen to represent reality (hence the term pseudo reality) and withdrawn from the model ensemble. As a measure of prediction error, a squared difference between the projected future jet position and the jet change in this pseudo reality can be calculated for both MDER and uMMM approaches. The process is repeated n times, once using each model as the pseudo reality, and the resulting root mean squared errors (RMSE) quantifies the accuracy of the prediction.

The MDER method is applied in this thesis to constrain future shifts in the austral jet stream (see Chapter 5). If the above described method of the MDER is applied to a projected target variable using multiple process-oriented present day diagnostics, it provides inside and a better understanding of the underlying processes that force future climate projections.

Risk of spurious correlations and model interdependence

Emergent constraint methods need to be carefully applied to model ensembles. The significance of predictive relationship in the CMIP5 and CMIP3 model archive was assessed by Caldwell et al. (2014) using data mining. They demonstrated that a broad survey of relationships, assuming independence between models, variables, locations and seasons yields misleading results. Simply identifying a strong relationship across an ensemble of models is no sufficient proof that a real physical relationship exists (Caldwell et al., 2014). They concluded that a necessary property of emergent constraints is a physical basis for the relation, the mechanisms which links observable present-day quantities to future climate change variables need to be clearly identified by a convincing physical explanation. Furthermore, Klein & Hall (2015) conclude that the physical understanding should also explain intermodal variations of the simulated spread of both, observable proxy and predictand. However, it might be easier to establish such emergent constraints for individual feedbacks than for climate projections since feedbacks of the Earth system are more closely connected to physical processes (Caldwell et al., 2014; Fasullo et al., 2015).

Most emergent constraints on biogeochemical feedbacks are only valid as long as processes that are important for the long-term climate response are also driving the observable short-term fluctuation. When the future climate system is forced to cross some threshold the transition into a new state of the climate system may be faster than the cause (Alley et al., 2002). Such changes in the climate system are called "tipping points" and are potentially sudden and also irreversible (Lenton et al., 2008). Many of these tipping points are associated with ecosystem-climate feedbacks, such as tropical and boreal forest dieback and permafrost loss in the Tundra and the Arctic oceans (Lenton et al., 2008; Ciais et al., 2013), but these tipping points are difficult to predict. Although such tipping elements have the potential to alter emergent constraints, this is not necessarily always the case. Cox et al. (2013) compared their results derived from C^{4}MIP models (see Section 2.3.2) to three models with perturbed key land surface parameters (e.g., temperature sensitivity of photosynthesis and soil respiration), where one of the three perturbed models simulates Amazonian forest dieback due to warming and drying in Amazonia (Cox et al., 2004) after the year 2050. They found that these models predict extremely low values for the carbon cycle-climate feedback but were also confirming the tight relationship found across the C^{4}MIP models.

For a sufficient proof of the identified relationship, the emergent constraints should also be robust across different model generations

2.3.2   Review of Existing Emergent Constraint Studies

Emergent constraints are a relatively new area of research with some promising examples that have been published in the literature recently. Some of the studies focus on constraining overall Equilibrium Climate Sensitivity (ECS) and Transient Climate Response (TCR). ECS is defined as the equilibrium change in the annual global mean surface temperature following a doubling of atmospheric equivalent CO_2 concentration (IPCC, 2013), which is largely determined by atmospheric processes such as radiative forcing. The CMIP5 model spread in ECS ranges from 2.1°C to 4.7°C and has not been significantly reduced compared to previous IPCC assessments (IPCC, 2013). The TCR is defined as the mean global temperature change at CO_2 doubling and is calculated from an idealized simulation (IPCC, 2013) where CO_2 concentrations increase by 1% per year (Section 2.1).

In climate models especially feedbacks from low-latitude clouds and water vapor play an important role for the ECS (Fasullo et al., 2015).Previous studies have highlighted that the net shortwave feedback at low latitude clouds provide the largest source of uncertainty in climate feedbacks (Soden & Vecchi, 2011), which implicates in particular low clouds (Klein &

Hall, 2015). However, the representation of low-latitude clouds remains a challenge to climate models, as they require an adequate representation of related processes (e.g., moisture, radiative processes, convection, and interaction to large-scale circulation). Fasullo & Trenberth (2012) explored the structure of the lower latitude troposphere, emphasizing the seasonal interactions between moisture, dynamics, clouds and radiation. A negative linear correlation was found between ECS and mean relative humidity from May to August in the middle troposphere, which has been motivated in previous studies (Bony et al., 2004). The authors hypothesized that the processes responsible for "drying the troposphere served as an indicator of the interaction between moisture and the tropical circulation" Fasullo et al. (2015). This process was linked to future projections via the expansion of such dry zones with warming. In a similar vein Sherwood et al. (2014) explored the connection between ECS and the strength of mixing in shallow convective clouds over the warm tropical ocean. The underlying mechanism is the dehydration of lower cloud layers by mixing. This effect increases as the climate warms and it varies proportional to the internal mixing strength of models. Models with higher sensitivity simulate certain cloud-relevant phenomena better, which was also found in previous studies (Fasullo & Trenberth, 2012). Sherwood et al. (2014) yield a central estimate of ECS in the order of $4 \pm 1°C$ However, the metric suffers from large uncertainties in the observed estimates. Gordon & Klein (2014) tried to constrain ECS using a different cloud parameter, i.e. the optical depth of low-level clouds, which is proportional to the reflectivity of clouds. Distinguished by latitudes, the predictor was found to be the sensitivity of optical depth to local surface temperature, which was derived from the variability of daily to interannual time scales. The authors found the change in optical depth under local warming to be generally positive for cold clouds. This behavior was found for the current climate and on the long-term climatology. However, appropriate observations are yet not available. Therefore the ECS response of low level clouds optical depth remains unconstrained.

For a better understanding of the role of lower tropospheric stability in ECS Qu & Hall (2014) used a metric model, relating the amount of low clouds in regions of persistent cloudiness to changes in the strength of top of boundary layer inversion and sea surface temperatures. They found that the reduction in low level clouds under warming supports a positive feedback but only yield a weak constraint.

In a more recent study Tian (2015) connected ECS to the magnitude of the double-Inter Tropical Converges Zone (ITCZ) bias and was related to low level cloud feedbacks. Models with a low sensitivity of this feedback inaccurately simulated the southern branch of the ITCZ, concluding that most CMIP3 and CMIP5 models might underestimate the ECS.

In order to find multiple lines of evidence to constrain ECS to cloud properties, Sanderson et al. (2015) and Huber et al. (2011) both used a bulk multivariate assessment of model skill to investigate whether excluding generally poor performing models could constrain climate variables in the CMIP5 ensemble. If a model generally performs poor, it can be down-weighted or excluded from the ensemble. This approach is not sensible to possible spurious correlations, as errors are combined into one metric. Using this approach Sanderson et al. (2015) found CMIP5 models with an ECS of less than 3K to perform generally worse in their mean state. Their best estimate of ECS was found to be 3.5 ± 0.6 °C in the likely range of 2.8 - 4.0 K. Huber et al. (2011) found that Top Of Atmosphere (TOA) fluxes to correlate well with ECS, creating a large number of predictive sensitivities, although they are not necessarily independent. The approach used by Sanderson et al. (2015) and and Huber et al. (2011) dismisses models on the basis to be inconsistent with observations, which might be premature in some cases as some model errors might not be relevant for the calculation of ECS (Fasullo et al., 2015).

Although the ECS could not fully be constraint, the studies so far find that the ECS is generally underestimated by climate models (Fasullo et al., 2015).

While cloud feedbacks of the lower latitude are well known to impact the ECS, additional contributing to this uncertainty comes from feedbacks of the cryosphere and water vapour.

Addressing this contribution, Hall & Qu (2006) demonstrated one of the first emergent constraints. In the constraint on snow-albedo feedbacks the large inter-model variation of the feedback strength in a warming climate is related to the variations in the seasonal cycle of the snow albedo (Hall & Qu, 2006; Qu & Hall, 2014), providing an observational constraint. This analysis was carried out with two different model ensembles, namely CMIP5 and models from the previous phase, CMIP3, proving the robustness of this relation. Both studies found a snow albedo feedback of approx. 1% snow cover decrease per Kelvin of warming. Most climate models were found to underestimate the observed trend of Arctic sea-ice loss (Hall & Qu, 2006), implying wrong projections for the timing of ice-free conditions. By relating September Arctic sea-ice cover over the 21st century to past trends of sea-ice cover, Boé et al. (2009b) found that under a medium GHG scenario the Arctic sea-ice will be vanished before the end of the 20th century. Consistent results were found by Massonnet et al. (2012), who related future September Arctic sea-ice cover to September sea ice extent, annual mean sea-ice volume and the amplitudes of the mean seasonal cycle of sea-ice extend. Massonnet et al. (2012) used only those models that are within a 20% tolerance limit of the reference data set, where the limit was arbitrary chosen. The authors suggest a faster rate of summer Arctic sea-ice decline than simulated by most of the climate models.

Also Crook & Forster (2014) found that climate models largely underestimate the extratropical surface cryosphere feedback (0.4 - 1.2 W m-2 K-1 compared to 3.1 ± 1.3 W m-2 K-1) under warming, in a more recent study. They found a useful proxy for the cryosphere feedback to be variations in the seasonal cycle of the cryosphere similar to Hall & Qu (2006).

Water vapour is the largest contributor to climate change and therefore has the largest single feedback term for ECS. In this context Gordon et al. (2013) related the water vapour feedback to observed variability between 2002 and 2009. The study demonstrates the physical explanation of the relation between short and long-term forced changes in models under warming. However, they yield only a relative weak relation combined with large uncertainties in the observations precluding any tight constraint. The authors suggested an observational record of 25 years or longer could significantly improve the demonstrated observational constraint.

Additional to the ECS other studies focus on constraining TCR, which is a measure of the strength and rapidity of surface temperature response to GHG forcing (IPCC, 2013). Boé et al. (2009a) related the TCR to the deep ocean polar mixing layers, showing that models with deeper polar mixing layers have a larger ocean warming associated with smaller global surface warming. The observational constraint further suggests, that models overestimate polar deep ocean mixing and therefore underestimate surface warming. Using a cluster analysis algorithm, Mahlstein & Knutti (2010) found a good correlation of TCR to regional climate change patterns. This analysis identifies regions of similar projected change (e.g., temperature, precipitation). With this method Mahlstein & Knutti (2010) were able to reduce the spatial uncertainty of the projected change of different climate variables. The TCR is also well correlated with observed values of historical climate responds of TCR found by Gillett et al. (2013), as reported by Gillett (2015). Here, a somewhat lower warming range of 0.8 - 2.5K was found than reported by IPCC AR5 (1.0 - 2.5K). Gillett et al. (2013) used a detection and attribution analysis to observationally constrain the TCR. In this analysis method observed temperature changes are fitted to simulate GHGs, other anthropogenic and natural responses by regression. In a second step simulated GHG-induced warming from each model is multiplied by the obtained multi model estimate of the regression coefficients to yield the observational constraint. The advantage of this method is that it does not imply a linear relation between the present-day diagnostic and the TCR. Gillett et al. (2013) found that the relation between TCR and the response to GHG forcings may not be linear, as broadly assumed.

Another measure of Earth system sensitivity is the TCRE, which provides a measure of the maximum allowed cumulative CO_2 emission since pre-industrial times for a given level of global average surface warming. The magnitude of the terrestrial carbon sink is a key uncertainty

when estimating the TCRE. This uncertainty can be attributed to uncertainties in efficiency of the carbon cycle in response to changes in the environmental conditions (see Section 2.4) such as climate change and increase of atmospheric CO_2 concentrations. The first promising emergent constraint on carbon cycle feedbacks was found by Cox et al. (2013) across a set of models participating in the C^4MIP, (Friedlingstein et al., 2006)). In this study the carbon cycle-climate feedback was related to the observable sensitivity of the interannual variability on the CO_2 growth rate due to tropical temperature variations. Cox et al. (2013) found models to largely underestimate this feedback compared to the observationally constraint feedback of -53 $\pm$ 17 GtC per K.

Since ECS and TCR depend on multiple individual processes other emergent constraint studies focus on constraining individual key climate feedbacks or variables in other fields and regions with observations directly. In order to understand the impact of future precipitation change (Schaller et al., 2011; O'Gorman, 2012). Allen & Ingram (2002) proposed one of the very first emergent constraints, relating observable temperature changes to future changes in precipitation, finding a sensitivity of 6 - 7% precipitation increase by 1 K of warming. Further extending this research Schaller et al. (2011) explored variations in the climate variability, global and regional features of precipitation, and related those to comparable variations in observed temperature. However, only by choosing a subset of models, to create an observational constraint the uncertainty can be reduced by half. O'Gorman (2012) related tropical precipitation extremes to their inter annual climate variability, reporting a sensitivity of daily tropical precipitation to climate change of the order of 10% per K of surface warming. Furthermore, this sensitivity is found to be higher than in the extra tropics and is mainly associated with precipitation on land regions.

Oceans play an important role in terms of heat and carbon uptake. Therefore, processes influencing the uptake conditions of heat and carbon are also in the focus of observational constraint studies. For example Huang & Ying (2015) were using a multi model ensemble pattern regression approach to observationally constrain patterns of tropical Pacific Sea Surface Temperatures (SST). This approach first extracts leading modes of historical model biases and in a second step linearly correlates modes between these historical integrations and projections of tropical Pacific SST, using multivariate linear regression. The so corrected SST pattern displays an El Nino-like pattern reducing intermodel uncertainty by half. The ventilation of the deep ocean is strongly impacted by the surface wind stress. Changes in the general circulation therefore impact the heat and carbon uptake of the ocean. Son et al. (2010) found that the main driver of changes in general SH circulation trends are mainly related to trends in ozone recovery. Models showing a stronger ozone depletion in past climate also simulated a stronger poleward shift and intensification of the SH jet stream and a greater expansion of the SH Hadley cell in summer. Sansom et al. (2013) used a statistical framework of simple analysis on variance to observationally constrain North Atlantic cyclone frequency in responds to climate change. This framework essentially quantifies the uncertainty associated with the estimates of the mean climate change responds. Applying this framework yielded a statistically significant decrease in cyclone frequency under climate change.

Further analysis is required to constrain the key Earth system feedbacks, but the studies discussed above demonstrate the potential of emergent constraints to reduce uncertainty in future climate projections with observations.

2.4   The Carbon Cycle

Two of the three emergent constraint studies examined in this thesis focus on the carbon cycle. Here an overview of the scientific background of the carbon cycle is given while further details
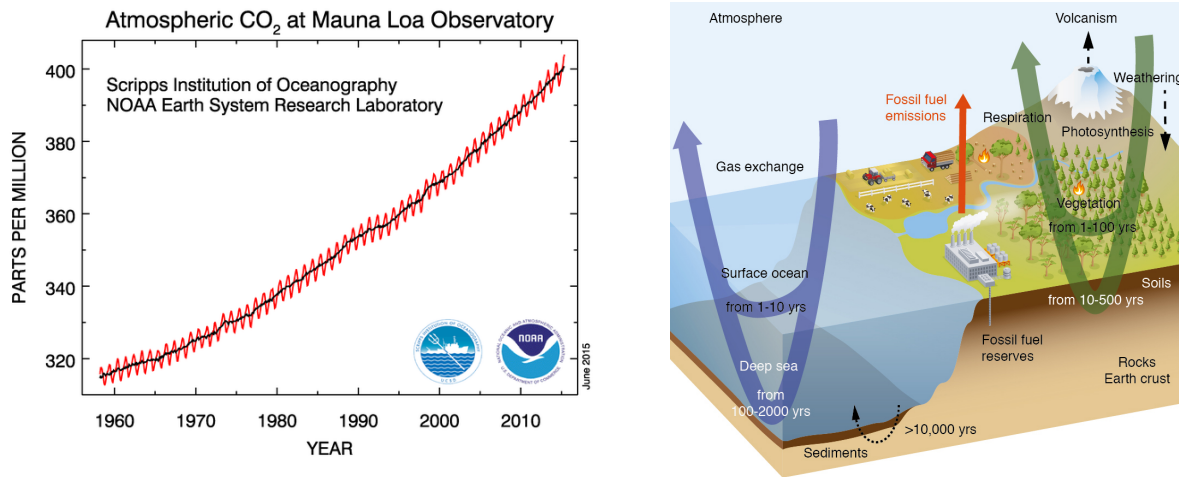
Figure 2.6: (a) Observed atmospheric CO_2 concentrations at the Mauna Loa Observatory between 1958 and 2015 for monthly (red) and annually (black) averaged CO_2 concentrations (Dlugokencky & Tans, 2014). (b) Schematic overview of the global carbon cycle. The numbers represent reservoir turnover times. From IPCC FAQ 6.2 Ciais et al. (2013) their Figure 1

on the two emergent constraints and the corresponding results are presented in Chapters 3 and 4, respectively.

In the atmosphere, CO_2 is the second most important GHG after water vapour. It absorbs and emits longwave internal infrared radiation at its two infrared-active vibration frequencies, leading to additional warming at the Earth surface. The greenhouse effect of CO_2 causes higher temperatures which in turn lengthens the terrestrial growing season in the extra tropics with direct implications for the terrestrial carbon sources and sinks.

Charles David Keeling started to measure CO_2 in the atmosphere in 1958 at Mauna Loa, Hawaii (Figure 2.6a). His measurements gave evidence that burning fossil fuels results in a buildup of atmospheric CO_2 (Keeling et al., 1976). Since then until 2015 the atmospheric CO_2 concentration increased by about 100 ppmv at Mauna Loa and about 75 ppmv at Pt. Barrow, Alaska between 1974 and 2013 as a result of increasing anthropogenic CO_2 emissions (Ciais et al., 2013). In addition to the annual increase of the CO_2 concentration a seasonal variability can be measured in the atmosphere CO_2, mirroring the phase of the carbon cycle.

The carbon cycle describes the exchange of carbon in the Earth system between different reservoirs. Some processes within this cycle exchange carbon on relatively fast times-scales (e.g., atmospheric carbon, land vegetation and soils, surface ocean, and freshwater), being on the time scale of years to millennia (Ciais et al., 2013). Other reservoirs (Sundquist, 1986), such as carbon stores in rocks and sediments exchange carbon on much longer time-scales (e.g., volcanic eruptions, erosion and sediment formation on the sea floor), hence these natural exchange fluxes can be assumed to be constant when looking at the current anthropogenic perturbation. The turnover time of a carbon reservoir is defined as the reservoir carbon mass, expressed in grams of carbon (1 PgC = 1 GtC = 1015 gC), divided by the exchange flux.

The global carbon cycle is schematically illustrated in Figure 2.6b, mainly focusing on the fast exchanging cycles: Carbon in the atmosphere is primarily in the form of CO_2, with a current concentration of approximately 400 ppmv (Dlugokencky & Tans, 2014), being equivalent to 828 PgC. Other trace gases containing carbon are methane (CH_4, ≈ 3.7 PgC) and carbon monoxide (CO, ≈ 0.2 PgC) and other components (e.g., hydrocarbon, black carbon aerosols and organic compounds), contributing even smaller amounts to the atmospheric carbon loading (Ciais et al., 2013). From the atmospheric reservoir, carbon is exchanged with the huge terrestrial and oceanic reservoirs.
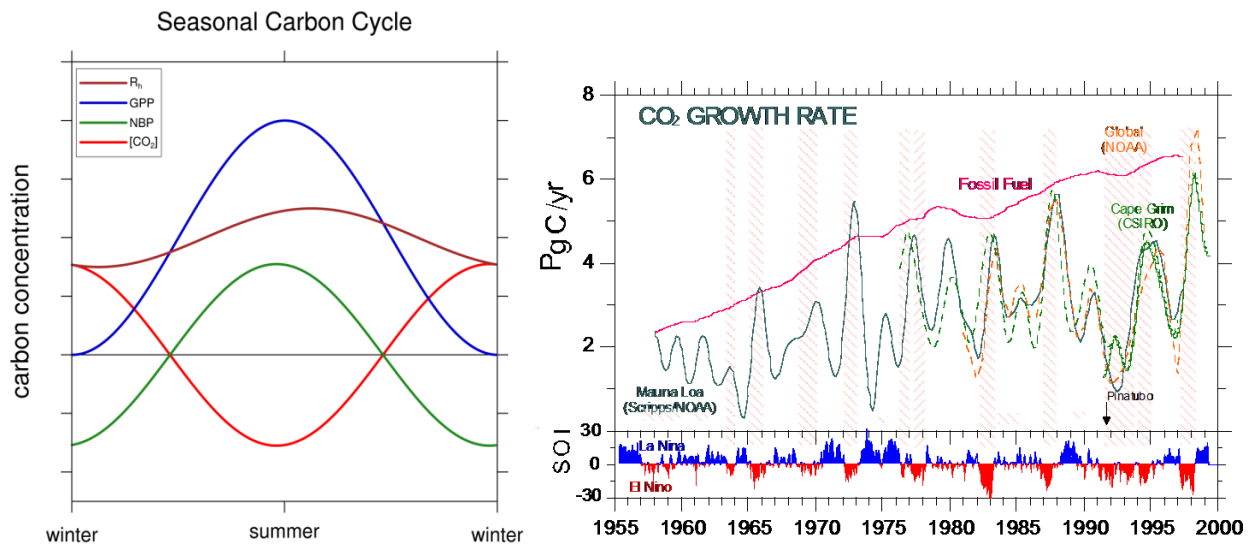
Figure 2.7: (a) Schematic illustration of the seasonal carbon cycle, representative for the Northern Hemisphere. (b) Comparison of CO_2 growth rate from various measurements (see labels in upper part) and fossil fuel burning (pink) and the ENSO oscillation index in the tropics (lower part). Red shaded areas indicate an increase in the CO_2 growth rate in El Nino - warm periods (http:www.esrl.noaa.govgmdpublications).

Atmospheric carbon is exchanged with the ocean via gas exchange at the surface, which is driven by the partial pressure difference of CO_2 between air and the sea. The carbon in the ocean is mainly present as inorganic (e.g., carbonic acid, bicarbonate, carbonic ions) and organic (e.g., phytoplankton, other microorganisms) carbon. Carbon is transported from the ocean's surface via primary productivity of marine phytoplankton, converting inorganic dissolved carbon to organic matter in photosynthesis. This so-called Biological Pump is limited by the availability of light and nutrients, crucial for photosynthesis and building cell structure. An important source for marine CO_2 is the formation of calcareous shells, which increases the partial CO_2 pressure in the ocean leading to a subsequent release of CO_2 into the atmosphere.

The increase of atmospheric CO_2 enhances the exchange of CO_2 molecules between air and sea thus leading to a net uptake of carbon by the ocean (McKinley et al., 2006) . This constitutes a negative climate feedback since it reduces the growth rate of CO_2 hence has a cooling effect on climate. The balance between atmosphere and ocean surface is rapidly obtained within a few years, sustained carbon uptake requires the export of the carbon from the surface to the deep ocean, which operates on much longer time scales (centuries).

In the terrestrial biosphere, carbon is stored in organic compounds, such as vegetation living biomass (450 - 650 PgC) and dead organic matter in litter and soils (1500 - 2400 PgC). Via photosynthesis, CO_2 is removed from the atmosphere and is stored as organic carbon in the plants. This flux is referred to as GPP, and carbon is then further cycled through plant tissues, litter and soil carbon and released back into the atmosphere by autotrophic respiration (Ra) of plants and heterotrophic respiration (Rh) by soil microbial decomposition and animals as well as by other disturbance processes (e.g., fires). All together these carbon fluxes are summarized as the Net Biosphere Productivity (NBP), describing the net carbon uptake by the biosphere.

Since the carbon uptake by photosynthesis only occurs during the growing season, the uptake and release of carbon by the terrestrial biosphere throughout the year causes a seasonal cycle of atmospheric CO_2 (Figure 2.7a), with high concentrations in the northern hemisphere winter when there is a net release of CO_2 from the land due to decomposition of organic matter in soils (brown), and lower values in summer when northern hemisphere photosynthesis (blue) results in a draw-down of atmospheric CO_2 (Keeling et al., 1995).

Most of the processes in the terrestrial and ocean carbon cycles are dependent on the environmental conditions. Human impacts (e.g., land use changes and fossil fuel burning) changes CO_2 emissions, which in turn change the atmospheric CO_2 concentration (Figure 2.7b). Photosynthesis is controlled by the atmospheric CO_2 concentration and also by climate (e.g., temperature, humidity, precipitation), where for example droughts reduce photosynthesis rates. Decomposition is mainly controlled by climate, with a warming climate for example increasing microbial activity and therefore decomposition (Figure 2.7b). Changes in the NBP, which is defined as GPP minus ecosystem respiration, will therefore change the amplitude of the CO_2 seasonal cycle as measured in the atmosphere (Figure 2.7a). Not only an increase or decrease in GPP or respiration but also a changes in the respective shape of the GPP and respiration seasonal cycle, could affects the seasonal cycle of NBP as illustrated in Figure 2.7a.

An increase of atmospheric CO_2 stimulates plant photosynthesis, thus leading to additional carbon uptake by the terrestrial biosphere (Norby et al., 2005; Leakey et al., 2009). This so called CO_2 fertilization effect helps plants to more efficiently use ground water in dry areas, increasing biomass and soils. The CO_2 fertilization effect also constitutes a negative feedback to climate, but the magnitude of this sink is also dependent on other factors, such as water and nutrient availability.

The warming of the atmosphere leads to enhanced release of carbon due to faster soil respiration, as indicated by climate models (Arora et al., 2013). This leads to a net decrease of the terrestrial carbon sink, which is a positive feedback to climate (Cox et al., 2000; Friedlingstein et al., 2001).

The interactions between the reservoirs can be mathematically summarized and expressed in the change of atmospheric CO_2 over the time t as the negative sum of carbon emissions E and carbon sinks S (Le Quéré et al., 2013):

$$\frac{d\text{CO}_2}{dt} = E - S \tag{2.3}$$

The main contributions to the emissions E are anthropogenic, such as fossil fuel burning and land use change. The sink term S can be represented as changes in terrestrial C_L and marine C_O carbon reservoirs, where $S = \frac{dC_L}{dt} + \frac{dC_O}{dt}$.

As noted above, the magnitude of the carbon sinks themselves depend on the environmental conditions such as the change in atmospheric CO_2 and temperature T and can be described for each reservoir separately, assuming linear responses (Friedlingstein et al., 2003, 2006):

$$\frac{dC_L}{dt} = \beta_L \ \frac{dCO_2}{dt} + \gamma_L \ \frac{dT}{dt} \tag{2.4}$$

$$\frac{dC_O}{dt} = \beta_O \ \frac{dCO_2}{dt} + \gamma_O \ \frac{dT}{dt} \tag{2.5}$$

Both equations describe the long term change in the land (L) or ocean (O) reservoirs (in GtC), where β_L and β_O describe the land and ocean carbon sensitivity to atmospheric CO_2, i.e. a measure of the carbon cycle CO_2 feedback parameter, and γ_L and γ_O are the land and ocean sensitivity of the carbon reservoir to climate change, i.e. a measure of the carbon cycle-climate feedback parameter.

However, as both of these feedbacks operate simultaneously, they cannot be directly evaluated with observations. Likewise, it is not possible to use only a single simulation to diagnose carbon cycle feedbacks with models, since there are two unknowns in equations (2.4) and (2.5), β and γ. ESMs and simulations where the response of the carbon cycle to climate change is either enabled or disabled, are necessary to determine those carbon cycle feedback parameters.

The coupled simulation experiment, in which the carbon cycle is fully coupled to the climate system, provides the quantities for equations (2.4) and (2.5), but a second type of simulation is needed to derive the two yet unknown feedback parameters β and γ. In such simulation experiments, often referred to as the "uncoupled simulation", the carbon cycle responds to the atmospheric CO_2 concentrations but the climate system only sees a constant control CO_2 concentration (Friedlingstein et al., 2003). Because in these simulations the temperature does not change significantly over time (i.e., can be considered to be constant) equations (2.4) and (2.5) for the uncoupled simulations simplify to:

$$\frac{dC_L}{dt} = \beta_L \; \frac{dCO_2}{dt} \tag{2.6}$$

$$\frac{dC_O}{dt} = \beta_O \; \frac{dCO_2}{dt} \tag{2.7}$$

From these two equations it is possible to diagnose β_L and β_O from the models. When inserting the equations (2.6) and (2.7) into the equations (2.4) and (2.5), respectively, the parameters γ_L and γ_O can also be diagnosed for a given model.

Such idealized simulations are therefore a useful technique for assessing relative sensitivities of the carbon cycle in the models (Friedlingstein et al., 2003).

2.5 Mechanism of the Southern Hemispheric Jet Stream

The third study focuses on observational constraints on the future shift in the austral jet stream (Wenzel et al., 2016). The SH jet stream is part of the global general circulation, which is caused by a equator-to-pole heating gradient and the Coriolis force, depicted in Figure 2.8. Here a brief overview of the scientific background is given while further details on important processes and the results are presented in Chapter 5.

The inhomogeneous heating of the Earth's surface by the sun, with a maximum in the tropics causes a thermal expansion of the air mass and meridional pressure gradient. This in turn drives the poleward mass flux in the upper troposphere, redistributing the temperature and therefore causing a change in surface pressure (Wallace & Hobbs, 2006). This redistribution in turn drives a compensating low level flow equatorward on each hemisphere, respectively. The Coriolis force adds a zonal angular momentum to the meridional redistribution of heat, creating steady easterly blowing trade winds in the tropics.

Baroclinic instability in the mid latitudes causes the meridional circulation to brake in a wave like structure, dividing the global circulation into three cells with a high pressure band at 30° N/S and a low pressure band between 50° - 60° N/S. At these latitude bands, the temperature gradients are especially strong. The resulting complex circulation system, depicted in Figure 2.8, is responsible for the weather on Earth, and explains the movement of air and the existence of storm tracks.

Jet streams are narrow bands of relatively high wind speeds in the upper troposphere and are created by the interplay of the Coriolis force and the temperature gradient between equator and pole. Air parcels traveling poleward experience an angular momentum through the Coriolis force. These parcels conserve this momentum resulting in a westerly motion of air. According to the thermal wind relation, describing the vertical wind shear caused by a horizontal temperature gradient, the resulting geostrophic wind increases with its height. At high latitudes, where the temperature gradient at the surface is very strong, the extratropical jets are located at the upper troposphere, at about 250 hPa.

Especially the extra tropical jets have large impacts on the regional weather, where the convergence of cold polar and warm subtropical air causes large convection with associated
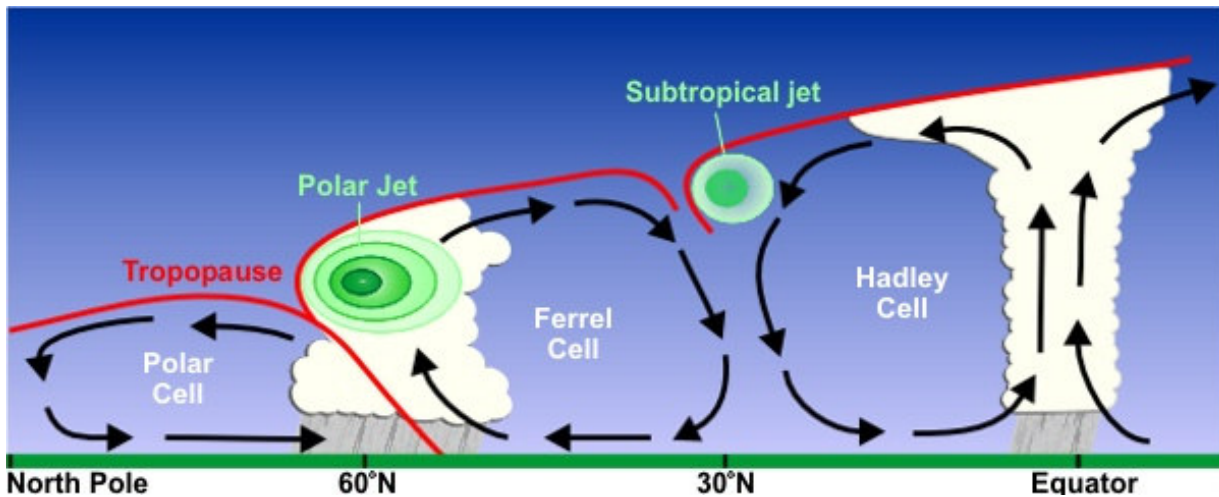
Figure 2.8: Schematic illustration of the general wind circulation, representative for the northern hemisphere. (http:www.srh.noaa.govjetstreamglobaljet.htm).

storms and precipitation. For example increased rainfall over eastern Australia and the southern part of South Africa (Gupta & England, 2006) are associated with shifts in jet streams being the transition to the subtropical dry zone (Kang et al., 2011). Earth's general circulation not only redistributes heat in the atmosphere influencing regional weather conditions, but also drives the ventilation of the ocean due to an increased ocean surface wind stress (Waugh et al., 2013). The primary regions where heat and carbon are taken into the deep ocean are the southern oceans. An increased ventilation of the deep ocean not only implies an increase of heat and carbon uptake (Waugh et al., 2013), but also changes the circulation in the oceans. A change in the ocean circulation would also affect Antarctic sea ice with further implications of sea level rise (Pritchard et al., 2009).

A change in the meridional temperature gradient will change intensity, height and latitude position of the jet stream, according to the thermal wind relation. Increasing the temperature gradient will lead to a strengthening of the SH jet stream and a poleward shift and vice versa. The SH jet also appears to be sensitive to temperature perturbation on either side (Gerber & Son, 2014). A heating of the tropics would therefore have the same effect as cooling in the Antarctic. This mechanism causes the general circulation, and hence the jet stream, to vary throughout the year. But also on climatological time scales the jet position is strongly affected by changes in the meridional temperature gradient, caused by external forcings, in particular changes in stratospheric ozone and GHGs.

Ozone in the lower stratosphere absorbs incoming solar radiation, and reemits leading to additional warming. The ozone depletion during the last decades has led to anomalous radiative cooling in the polar upper stratosphere and the cool air descended into the tropopause. Associated with this is a lowering of geopotential height of the tropopause and a strengthening of the polar vortex in the stratosphere (Thompson & Solomon, 2002; Gillett & Thompson, 2003). This in turn causes a poleward shift in the SH jet stream. However, the exact mechanisms by which changes in the polar stratospheric temperature impact the troposphere are still not fully understood and are subject of ongoing research (Kushner & Polvani, 2004; Chen & Held, 2007; Orr et al., 2012).

On the other hand anthropogenic GHGs increase Earth global temperature as described in Chapter 2.1. Although temperature will increase globally especially in the tropics it will cause a stronger lifting of the geopotential height of the tropopause having the same effect as the depletion of ozone at pole (Polvani et al., 2011). These two effects, namely ozone depletion and GHG increase, acted in concert to impact the SH extratropical circulation during the late 20th century and shifted the SH jet stream poleward (Gillett & Thompson, 2003; Son et al., 2010).

Current AOGCMs show an equatorward bias in the SH jet position, which has direct implications for future projections. The radiative forcing sets an ultimate high-latitude limit to the SH jet position. Models that are closer to that limit are unable to shift the jet position very far further poleward (Kidston & Gerber, 2010; Barnes & Hartmann, 2010; Simpson et al., 2013). Such models appear to be insensitive to external forcings. Biases in the current jet position are closely linked to biases in mid-latitude shortwave cloud forcing distribution anomalies (Ceppi et al., 2014; Grise & Polvani, 2014). A positive shortwave cloud forcing anomaly causes a net warming in the hemisphere, shifting the meridional surface temperature gradients and baroclinicity. Additionally, the bias in the jet position is also linked to a high persistence of the Southern Annular Mode (SAM), which is the leading mode of southern circulation variability. The persistence of this mode is described by the e-folding time, wich decreases with a poleward shift of the jet (Kidston & Gerber, 2010; Barnes & Hartmann, 2010).

Future trends of jet positions and shifts remain uncertain also in terms of future temperature trends. One source of uncertainty arises from the models climate sensitivity to perturbed Antarctic temperature. Gerber & Son (2014) found, that models having a similar global warming signal strongly deviate in the simulated SH jet position due to differences in polar stratospheric temperature trends associated with ozone recovery. The dynamical response to a given temperature change defines the circulation sensitivity and is another source of uncertainty in the models (Kidston & Gerber, 2010; Gerber & Son, 2014). Both, the climatological and the circulation sensitivity in the models cause a wide spread in the actual SH jet positions. Finally, the magnitude of GHG emissions in the future also determines the actual shift in the SH jet position in the future.

Chapter 3

Emergent Constraints on Carbon Cycle-Climate Feedback [1]

As detailed in the Scientific Background (Section 2.3) two main feedbacks of the carbon cycle control the efficiency of the terrestrial carbon sink. This Chapter presents results how the carbon cycle-climate feedback (γ_L) can be observationally constrained with observations, whereas results on the constraint of the carbon cycle-CO_2 feedback (β_L) are discussed in Chapter 4.

One of the main finding of the IPCC AR5 is that "Cumulative emissions of CO_2 largely determine global mean surface warming by the late 21st century and beyon"(IPCC, 2013). Indeed (Section 2.4), cumulative CO_2 emissions since pre industrial times (e.g., 1870) are approximately linearly related to global near surface temperature increase. Any level of warming can be associated with a given amount of cumulative CO_2 emissions (Collins et al., 2013). A 2°C warming target, as currently discussed by policy makers, therefore implies a cumulative CO_2 emission of not more than 1000 GtC (for a likely probability), where non-CO_2 forcings are not accounted for (Collins et al., 2013).

The near-linearity of this relation between cumulative CO_2 emissions and global temperature warming is the result of the interplay of several compensating processes between the carbon cycle and climate. This relation is referred to as the TCRE and is estimated to be likely between 0.8 to 2.5°C per 1000 PgC. The large uncertainty range arises from uncertainties in carbon cycle feedbacks, where the carbon cycle responds to the CO_2 emissions affecting the atmospheric CO_2 concentrations, and climate feedbacks, where climate responds to the change in the atmospheric CO_2 concentration. Thus the maximum allowed amount of CO_2 emission for the given 2° warming target is very uncertain.

To further reduce these uncertainties feedbacks of the carbon cycle to the climate system need to be better understood and if possible constrained by observations. This builds the motivation for the results presented within this Chapter and in Chapter 4.

The long-term sensitivity of land carbon storage to future climate warming (γ_L, see Section 3.4) can be quantified in terms of carbon loss per unit temperature change (Friedlingstein et al., 2006), usually given in units of GtC K-1. The differences in γ_L simulated by the models remains a key uncertainty in climate projections of the 21st century (Friedlingstein et al., 2006; Booth et al., 2012). However γ_L cannot be directly evaluated with observations, because γ_L relates to a theoretical reference state in the absence of climate change, which is obviously not observable. The tropics make a dominant contribution to uncertainties in γ_L (Raddatz et al., 2007; Huntingford et al., 2013). Uncertainties in future projections of tropical rainfall, and in the response of ecosystems to these, are central to the overall uncertainty in the response of the land carbon cycle to climate change (Rammig et al., 2010; Jupp et al., 2010; Huntingford et al., 2013).

In a recent study, Cox et al. (2013) found a correlation between the long-term sensitivity of tropical land carbon storage to climate warming (γ_{LT}) and the short-term sensitivity of atmospheric CO_2 to temperature variability on interannual time scales (γ_{IAV}). A correlation

---

[1]The contents of the majority of this chapter appears in similar form in the study of Wenzel et al. (2014), Emergent constraints on climate-carbon cycle feedbacks in the CMIP5 Earth system models. Journal of Geophysical Research: Biogeosciences, 119(5), pp.794-807.

between the long-term and the short-term sensitivity can be expected if the processes that play for the long-term response are also driving the short-term fluctuations, i.e. if processes occurring on long time scales (such as vegetation dynamic) are not dominant. This is potentially the case here as both the short- and long-term responses of the tropical land to climate are predominantly driven by changes in the balance between the gross carbon fluxes, photosynthesis and ecosystem respiration. Responses of the carbon cycle to climate anomalies are mirrored in the interannual variability (IAV) of the CO_2 growth rate (Keeling et al., 1995, 1989; Francey et al., 1995). This relationship is especially valid in the tropics (see Section 2.4), where strong variability caused by El Niño gives a spatially coherent pattern of warmer and colder years (Bousquet et al., 2000).

The variability of tropical temperature and atmospheric CO_2 concentrations are both observable quantities, and therefore γ_{IAV} can be directly inferred from observations. A strong correlation within models between γ_{IAV} and γ_{LT} therefore provides an Emergent Constraint on the long-term sensitivity of land carbon storage to climate change.

As part of this study, the theoretical basis for describing the emergent constraint reported by Cox et al. (2013) is started to be developed. The analysis is also extended by considering the more recent ensemble of CMIP5 ESMs, including models with an interactive land nitrogen cycle which have the potential to change the correlation between γ_{IAV} and γ_{LT}. In addition, land and ocean net CO_2 fluxes from the Global Carbon Project (GCP) were used to develop the observational constraint on γ_{IAV}, rather than the global atmospheric CO_2 concentration as in Cox et al. (2013). This allows the approach to be applied to model runs with prescribed CO_2 concentrations as well as those with interactive atmospheric CO_2, and is more directly comparable to the carbon flux anomalies simulated in the ESMs. The sensitivity of CO_2 to tropical temperature IAV is calculated from two kinds of CMIP5 simulations: historical simulations driven by CO_2 emissions and standard simulations with a prescribed 1% per year increase in CO_2 concentration. The results are cross-checked with models from the previous Coupled Climate-Carbon Cycle Model Intercomparison Project (C^4MIP), as used in the study of Cox et al. (2013), but applying the new methodology presented here.

This Chapter is organized as follows: Section 3.1 describes the models and simulations used in this study. Section 3.2 provides an overview of the observations that are used to evaluate the models and to constrain the projections. The theoretical basis and the methodology for an emergent constraint are presented in Section 3.3. In Section 3.5 the results are presented and discussed and Section 3.6 closes with a summary.

3.1 Models and Model Simulations

In this study, the carbon cycle feedback constraints from eight ESMs participating in the CMIP5 project are analyzed. CMIP5 supported the climate model projections presented in the IPCC AR5 and includes a large number of different experimental designs (Taylor et al., 2012). The model data are available to the research community via the Earth System Grid Federation (ESGF). The models that are included in this study are listed in Table 3.1 together with their atmospheric and oceanic grids, and an appropriate reference.

For this study, model outputs from three simulations were analyzed and are listed in Table 3.2. The *esmHistorical* (hereafter referred to as "Historical") experiment is a fully coupled simulation from 1850 to 2005 with historical anthropogenic emissions of CO_2, atmospheric concentrations being calculated interactively by the ESM as the balance between anthropogenic emissions and uptakes by the land and ocean (Taylor et al., 2012). The *1pctCO2* (hereafter referred to as "1%COU") simulation is a standard idealized experiment forced with a 1% per year increase of atmospheric CO_2 concentration up to 4xCO_2, starting from the pre-industrial value for 1850 of ≈ 285 ppmv. The third simulation also considers a 1% per year increase of CO_2,

Table 3.1: CMIP5 models

	Model	Institute	Atmospheric Resolution	Oceanic Resolution	Main Reference
A	CanESM2	Canadian Center for Climate Modeling and Analysis, BC, Canada	T63, L35	256x192, L40	Arora et al. (2011)
B	CESM1-BGC	National Center for Atmospheric Research Boulder, CO, USA	0.9°x1.25° gx1v6, L53	0.9°x1.25° gx1v6, L53	Gent et al. (2011)
C	GFDL-ESM2M	Geophysical Fluid Dynamics Laboratory, United States	M54, L24	360x200, L50	Anon (2012)
D	HadGEM-ES	Met Office Hadley Center, Exeter, Devon, UK	N96, L38	1.0°-0.3° x 1.0°, L40	Collins et al. (2011)
E	IPSL-CM5A-R	Institut Pierre Simon Laplace, Paris, France	96x95, L39	2x2, L31	Dufresne et al. (2013)
F	MIROC-ESM	Japan Agency for Marine-Earth Science and Technology, Japan; Atmosphere and Ocean Research Institute, Japan	T63, L80	256x192, L44	Watanabe et al. (2011)
G	MPI-ESM-LR	Max Planck Institute for Meteorology, Hamburg, Germany	T63, L47	GR15, L40	Giorgetta et al. (2013)
H	NorESM1-ME	Norwegian Climate Center, Norway	f19, L26	gx1v6, L53	Iversen et al. (2012)

Table 3.2: Overview of the simulations in this study

	Experiment	Coupling of carbon cycle	Available Period	Temporal Resolution	Forcing
1	Historical	Fully coupled	1850-2005	monthly	greenhouse gases, anthropogenic and volcanic climate forcing, land-use change, solar forcing, aerosols
2	1%COU	Fully coupled	1850-1989	monthly	1% per year CO_2 increase
3	1%BGC	Uncoupled	1850-1989	monthly	1% per year CO_2 increase

Table 3.3: Overview of land and ocean carbon modules in CMIP5 models

	Model	Land Models	References for Land Model	Ocean Models	References for Ocean Models
A	CanESM2	CLASS2.7 and CTEM1	Verseghy et al. (1993), Arora et al. (2011)	CMOC	Zahariev et al. (2008)
B	CESM1-BGC	CLM4	Lawrence et al. (2011)	BEC	
C	GFDL-ESM2M	LM3	Dunne et al. (2013)	MOM4	Griffies et al. (2004)
D	HadGEM-ES	JULES and TRIFFID	Clark et al. (2011), Clark et al. (2011)	Diat - HadOCC	Collins et al. (2011)
E	IPSL-CM5A-R	ORCHIDEE	Krinner (2005)	PISCES	Aumont (2003)
F	MIROC-ESM	MATSIRO and SEIB-DGVM	Sato et al. (2007)	COCO	Watanabe et al. (2011)
G	MPI-ESM-LR	JSBACH	Knorr (2000)	HAMOCC5	Assmann et al. (2010)
H	NorESM1-ME	CLM4	Lawrence et al. (2011)	HAMOCC5	Assmann et al. (2010)

but in which the carbon cycle is not affected by any climate change (*esmFixClim1*, hereafter referred to as "1%BGC", the biogeochemically coupled simulation). In this latter simulation (termed as the "uncoupled run" by Friedlingstein et al. (2003, 2006)) the radiation code of the ESM sees the control pre-industrial CO_2 concentration (so that there is no associated climate change), but the carbon cycle otherwise sees a 1% per year increase in atmospheric CO_2. As opposed to the Historical simulation that accounts for all known forcings (greenhouse gases, aerosols, land use change, volcanoes), the two 1% per year simulations are only forced with the CO_2 increase; all other forcings are held at their pre-industrial levels.

From the CMIP5 models that were available on the ESGF by summer 2013, those that provide both land and ocean carbon fluxes and storage for all three experiments were selected. For details of these models see Table 3.1. Table 3.3 lists details of the land and ocean carbon representation for each model. For comparison, also six models from the Coupled Climate Carbon Cycle Model Intercomparison Project (C[4]MIP Friedlingstein et al. (2006)) were analyzed. For C[4]MIP the coupled and uncoupled simulations were forced by anthropogenic CO_2 emissions for the historical period, followed by anthropogenic emissions from the SRES A2 scenario

(Nakicenovic et al., 2000).

3.2   Observations

The observational estimate of γ_{IAV} was calculated from land and ocean carbon fluxes from the Global Carbon Project (GCP, http://www.tyndall.ac.uk/global-carbon-budget-2010), providing the most recent long-term (1959 - present) and yearly updated data set (Le Quéré et al., 2013). The global carbon budget is estimated as the sum of CO_2 emissions and terrestrial and oceanic carbon sinks. CO_2 emissions from fossil fuel combustion, gas flaring and cement production are mainly based on data provided by several international organizations (Andres et al., 2012). In this dataset, the global ocean carbon uptake of anthropogenic carbon is estimated from the average of four global ocean biogeochemistry models, which were forced by observed atmospheric weather and CO_2 conditions (Le Quéré et al., 2013). The residual of the model based estimate of the oceanic carbon sink and the estimate of the atmospheric CO_2 concentrations defines the magnitude of the terrestrial carbon sink. Uncertainties of these estimates are given as 0.5 GtC per year.

Free-Air CO_2 Enrichment (FACE) experiments and flux measurements on towers also provide invaluable data of carbon exchange, especially for the terrestrial carbon sink. However, in this study the focus is on the overall response of the tropical regions to El Nino Southern Oscillation (ENSO) - driven climate variability. Unfortunately only few of the flux sites cover tropical ecosystems and none have measurements over a long enough period to allow a robust estimate of the sensitivity of carbon fluxes to ENSO variability. Neural network approaches, such as the Model Tree Example (MTE) described by Jung et al. (2011), are useful for spatial distribution of terrestrial carbon fluxes, such as GPP, but they are known to highly underestimate the inter annual variability of GPP. This is essential because of the lack of long-term measurements, in which MTE implicitly uses spatial patterns to infer the temporal variability.

Annual mean temperatures from the NOAA - National Climate Data Center (NCDC, http://www.esrl.noaa.gov/psd/data/gridded/data.noaamergedtemp.html) were used to estimate the interannual variability in the tropics (30°S - 30°N). This data set covers the period from 1880 to the present day at a monthly resolution (Smith et al., 2008).

3.3   Theoretical Basis

In Section 2.3.1 the fundamentals of the emergent constraint method have been described. Here the theoretical basis for such a constraint between the carbon cycle-climate feedback and the sensitivity of interannual variability of CO_2 to temperature variations is being developed while Section 3.4 describes how these parameters were inferred from the models and observations.

As part of this thesis, the theoretical basis for describing the emergent constraint of Cox et al. (2013) has been developed.

The change of land carbon over time, $\frac{\partial \Delta C_L}{\partial t}$, can be defined as the net carbon flux from land to atmosphere (NBP) that depends on the temperature (T), the atmospheric CO_2 concentration (C_a) and the stored carbon on land (C_L):

$$\frac{\partial \Delta C_L}{\partial t} = NBP(T, C_a, C_L) \tag{3.1}$$

As in previous studies (Friedlingstein et al., 2003, 2006), it is implicitly assumed that the impacts of other environmental changes, such as changes in rainfall, scale approximately linearly with the magnitude of the warming. This assumption is broadly consistent with the success

of pattern-scaling (Huntingford & Cox, 2000). Linearizing Equation (3.1) by Taylor-expanding about an initial equilibrium state leads to:

$$\frac{\partial \Delta C_L}{\partial t} = a\Delta T + b\Delta C_a + c\Delta C_L \tag{3.2}$$

where a, b and c denote $\frac{\partial \Delta NBP}{\partial T}; \frac{\partial \Delta NBP}{\partial C_a}; \frac{\partial \Delta NBP}{\partial C_L}$ and ΔC_L, ΔC_a and ΔT are changes relative to the initial state in land carbon uptake, CO_2 and temperature, respectively. Rewriting equation (3.2) and defining the constants a, b and c for consistency with Friedlingstein et al. (2006) gives:

$$\tau \, \frac{\partial \Delta C_L}{\partial t} + \Delta C_L = \gamma_L \, \Delta T + \beta_L \, \Delta C_a \tag{3.3}$$

with,

$-\frac{a}{c} = \gamma_L$: land carbon storage sensitivity to climate change

$-\frac{b}{c} = \beta_L$: land carbon sensitivity to direct CO_2 effects

$-\frac{1}{c} = \tau$: time scale of the carbon system

Equation (3.3) is as proposed by Friedlingstein et al. (2003, 2006), except for the first-term on the left-hand side. It is however vital to include this "inertial" term as it enables us to relate short-term variability to long-term sensitivity. To show this two-limits can be considerd:

1. On long (centennial) time scales, the interannual variability in the carbon cycle is much smaller than the long-term changes which means that $\tau \, \frac{\partial \Delta C_L}{\partial t} << \Delta C_L$ and the first term in Equation (3.3) is therefore negligible. The resulting equation is the one published by (Friedlingstein et al., 2003, 2006) and describes the long-term change of land carbon uptake depending on the change in temperature and atmospheric CO_2 as described in Section 2.4, Equation (2.4):

$$\Delta C_L = \gamma_L \, \Delta T + \beta_L \, \Delta C_a \tag{3.4}$$

   From Equation (3.4) γ_L, or its regional equivalents such as γ_{LT} for the tropics, can be calculated as in previous studies (Friedlingstein et al., 2003, 2006).

2. On short (interannual) time scales, changes in the long-term trend will be close to zero ($\Delta C_L \approx 0$, $\Delta C_a = 0$) and the second term in Equation (3.3) is now negligible. This limit gives a relationship between the long-term sensitivity of land carbon storage to climate change γ_L and the short-term sensitivity of the net atmosphere to land carbon flux to interannual temperature variations, $\gamma_{NBP} = \frac{\partial \Delta C_L}{\partial t}/\Delta T$:

$$\gamma_{NBP} = \gamma_L \, / \tau \tag{3.5}$$

   Here, as elsewhere in this paper, the subscript "L" represents "Land" and the subscript "NBP" denotes the "Net Biome Productivity". Equation (3.5) is in the spirit of the Fluctuation-Dissipation Theorem (Leith, 1975; Bell, 1980) as it is a relationship between the equilibrium sensitivity of the system to external forcing, and the fluctuations in the unperturbed system.

However, Equation (3.5) does not in itself imply an observational constraint on γ_L, for two reasons. Firstly, in general the NBP of a region is poorly known so that γ_{NBP} is not well constrained by observations. Secondly, the timescale τ is not known a priori. Here it is followed Cox et al. (2013) to overcome these problems. By focusing specifically on tropical land (30°N - 30°S) it is possible to get an estimate of γ_{NBP} based on the interannual variability in atmospheric CO_2, making use of the strong evidence that interannual variability in CO_2 is dominated by interannual variability in the NBP of tropical land (Denman et al., 2007; Schneising et al., 2014). This implies assuming: $\gamma_{NBP} \approx \gamma_{IAV} = -\frac{\partial \Delta CO_2}{\partial t}/\Delta T$, where here ΔCO_2 is the interannual variability in CO_2, and ΔT is the interannual variability in temperature. Under this assumption Equation (3.5) becomes:

$$\gamma_{IAV} \approx \gamma_{LT} / \tau \tag{3.6}$$

where the subscript "LT" now applies specifically to land in the tropics. Given an estimate of τ, Equation 3.6 provides a constraint on the long-term sensitivity from the observable γ_{IAV}.

The outstanding issue is therefore the estimation of τ, which is the subject of ongoing research. The Fluctuation-Dissipation theorem (FDT) indicates that τ could in principle be derived from the correlogram relating fluctuations in tropical temperature to fluctuations in atmospheric CO_2, by integrating across all lag-periods between these two variables (Bell, 1980). Unfortunately, the time-series data available from observations are invariably too short for this pure-FDT approach to provide a useful constraint (Kirk-Davidoff, 2009).

Alternatively it could be assumed that tropical land carbon behaves approximately like a one-box store with a single turnover time. In this case τ becomes the carbon turnover time, defined as the size of the store (i.e., the total vegetation plus soil carbon in the tropics) divided by the annual flux of carbon flowing through that store (i.e., the Net Primary Productivity in the tropics). Previous studies have shown that the turnover times for land carbon differ substantially across ESMs (Anav et al., 2013), and it therefore is not expectable that a correlation of γ_{LT} against γ_{IAV} will to fit around a single straight-line in the way that Cox et al. (2013) describe for the C^{4}MIP models.

In fact, Equation (3.6) implies that the linear relationship between γ_{LT} and γ_{IAV} reported by Cox et al. (2013) in turn implies a near constant value of τ across the model ensemble. As the turnover time for tropical land carbon also differs for the C^{4}MIP models (although to a lesser degree than for the CMIP5 models), this strongly suggests that the τ value relating γ_{LT} to γ_{IAV} is not determined by the turnover rates of tropical land carbon, but instead by a timescale that is common to all of the C^{4}MIP model runs.

The most likely candidate for such a timescale is related to the rate of climate change, which is largely determined by the common scenario of increases in CO_2 emissions prescribed in all of the C^{4}MIP models (Friedlingstein et al., 2006). Similarly the CMIP5 simulations experience a common timescale associated with the prescribed 1% per year increase in atmospheric CO_2, which differs slightly from the scenario timescale of the C^{4}MIP models.

The working hypothesis is therefore that the CMIP5 models will also fit around a straight-line in the γ_{LT} and γ_{IAV} space, but that this straight-line may have a different gradient to that for the C^{4}MIP models, owing to the different scenarios prescribed in each of these intercomparison exercises. The analysis presented in the remainder of the Section 2.3.1 allows this hypothesis to be tested, and most importantly assesses whether the emergent constraint on γ_{LT} as reported by Cox et al. (2013) is robust to changes in the ESM model generation and the prescribed climate change scenario.

3.4   Details on Methodology

As in Friedlingstein et al. (2003, 2006) Equation (3.4) is separately applied to the tropical land carbon in the coupled and uncoupled simulations:

$$\Delta C_L{}^c = \gamma_L \ \Delta T_T{}^c + \beta_L \ \Delta C_a{}^c \tag{3.7}$$

$$\Delta C_L{}^u = \gamma_L \ \Delta T_T{}^u + \beta_L \ \Delta C_a{}^u \tag{3.8}$$

where ΔT_T is the change in the average tropical near-surface temperature (over land and ocean between 30°N and 30°S), and the superscripts "c" and "u" denote the coupled and uncoupled simulations respectively.

In contrast to Cox et al. (2013), here the coupled (1%COU) and uncoupled (1%BGC) 1% per year simulations are used to estimate ΔC_L . As the CO_2 concentration is prescribed to be identical in the coupled and uncoupled runs, $\Delta C_a{}^c$ equals $\Delta C_a{}^u$. Following Friedlingstein et al. (2003, 2006) it is additionally assumed that $\Delta T_T{}^c >> \Delta T_T{}^u$. Although there may be small temperature changes in the uncoupled simulations, for example due to CO_2 -induced changes in the distribution of vegetation, these are negligible compared to the temperature changes in the coupled simulations (1% to less than 5% depending on the ESM). Under these assumptions the equations for the coupled and uncoupled changes can be subtracted to yield an expression for γ_{LT} which depends on the difference between the tropical land carbon storage of the coupled (1%COU) and uncoupled (1%BGC) simulations, and the temperature change in the coupled simulation:

$$\gamma_{LT} = (\Delta C_L{}^c - \Delta C_L{}^u)/\Delta T_T{}^c \tag{3.9}$$

The changes in these variables are computed for the tropical band (30°N - 30°S) as the difference between year 110 and year 30 after the start of the simulation at 1850 CO_2 concentration levels.

In order to calculate the short-term fluctuation, land and ocean CO_2 annual fluxes and tropical annual mean temperature from the models and the observations are de-trended using an 11-year running mean, as in Cox et al. (2013). The gradient of the least squares linear regression between anomalies in the CO_2 growth-rate and the tropical temperature defines γ_{IAV}. An advantage of calculating γ_{IAV} from the annual-mean land and ocean CO_2 fluxes is that the tropical temperature does not have to be aligned to the annual increment in CO_2 (Jones & Cox, 2005; Cox et al., 2013), as both are already centered in time in the middle of each year.

To assess robustness γ_{IAV} is calculated from both the Historical and the 1%COU simulation. For the Historical simulation data two years following large volcanic eruptions (Mount Agung, 1963; El Chichon, 1982; and Mount Pinatubo, 1991) are exclude, as done by Cox et al. (2013), and calculate γ_{IAV} over the period 1960 to 2005 in both models and observations. In the 1%COU simulation, a reference period from 40 to 90 years after the start of the simulation in 1850 is chosen, thus representing a warmer climate than today. The robustness of this choice was tested by calculating γ_{IAV} (and γ_{LT} above) also for different periods, which yielded very similar results (not shown).

3.5   Results of the Carbon Cycle-Climate Feedback Analysis

In both experiments with prescribed CO_2 (i.e, 1%COU and 1%BGC), all models were forced by 1% increase of CO_2 until quadrupling, except the GFDL-ESM2M model simulation, which
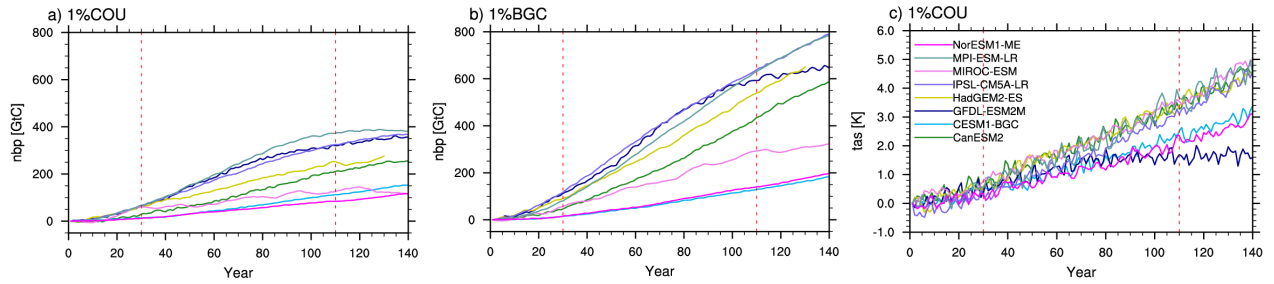
Figure 3.1: Quantities used to diagnose γ_{LT}. Cumulative tropical land carbon uptake for (a) the coupled simulation, (b) the uncoupled simulation, and (c) the projected tropical (30°N - 30°S) mean near-surface air temperature (tas) change in the prescribed-CO_2 coupled simulation (1%COU), for the CMIP5 models listed in Table 3.1. The simulations are forced by 1% per year rise in CO2 until quadrupling, except in the GDFL-ESM2M model, which prescribed a constant CO_2 after doubling. Vertical red lines show the interval over which γ_{LT} was calculated.

stopped increasing CO_2 at the time of CO_2 doubling (year 80) and kept the CO_2 concentration thereafter. The results for GFDL-ESM2M are therefore not comparable to the other models after year 80. The simulated tropical temperature change in the CO_2 prescribed coupled simulations (1%COU) show significant differences among the models at the time of CO_2 quadrupling (year 140 in Figure 3.1c), ranging from around 3 to 5 K (excluding GFDL-ESM2M). CESM1-BGC and NorESM1-ME show a slower increase in tropical temperature than the other five models.

There is also a wide spread in the tropical land carbon storage among the CMIP5 models (Figure 3.1), which is of the order of 117 - 381 GtC for the coupled (Figure 3.1a) and 182 - 788 GtC for the uncoupled (Figure 3.1b) simulations. Due to holding CO_2 at 2xCO_2 after the time of concentration doubling (year 80), the evolution of tropical land carbon storage of GFDL-ESM2M flattens in both simulations after atmospheric CO_2 stabilization.

From the difference of coupled and uncoupled simulations the climate carbon cycle sensitivity γ_{LT} can be quantified in terms of carbon loss per unit temperature increase. γ_{LT} values for each model are listed in Table 3.1. Confirming the findings of previous studies (Cox et al., 2000; Friedlingstein et al., 2001, 2006; Arora et al., 2013), all models show a negative γ_{LT}. However, there is a wide range of results in γ_{LT}, ranging from -6.7 GtC K-1 in CESM1-BGC to -116.4 GtC K-1 in GFDL-ESM2M.

It is interesting to note that CESM1-BGC and NorESM1-ME simulate the weakest climate change impact on tropical land carbon storage. The CLM4 land surface model, used in both of these ESMs (Table 3.3) includes an interactive nitrogen cycle. Therefore in these models, warming not only leads to carbon loss from enhanced soil decomposition, but also a counteracting carbon gain due to enhanced photosynthesis associated with increased soil nitrogen availability. The overall effect depends on the balance between these two effects, but is always lower (less negative γ_{LT}) than in carbon only models (Thornton et al., 2007, 2009; Zaehle et al., 2010).

γ_{IAV} is calculated over the period 1960 - 2005 for the historical simulations (Historical, Figure 3.2 left panels and Figure 3.3i) for consistency with the CO_2 observational data that was used, and over the period year 40 to year 90 from the 1%COU simulations. The variability of both carbon fluxes and tropical temperature is found to vary widely across the ESMs (range in Figure 3.1, Figure 3.3 and Figure 3.4), as does the strength of the correlation between CO_2 IAV and temperature IAV (linear regression in Figure Figure 3.3 and Figure 3.4). γ_{IAV} varies from zero (non-significant) for CESM1-BGC to -12 GtCy-1 K-1 for GFDL-ESM2M, with a multi model average of -4.6 GtC y-1 K-1.
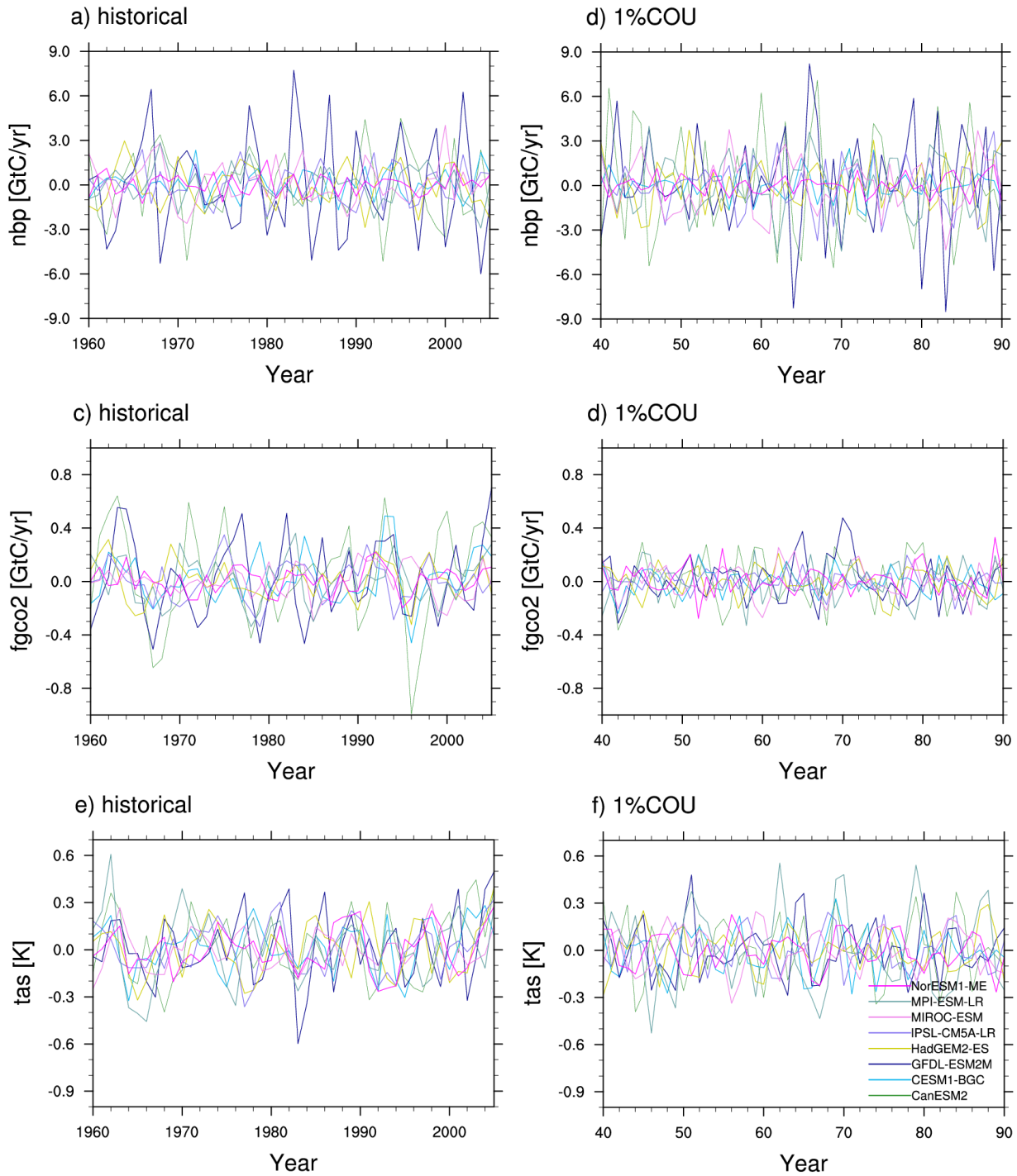
Figure 3.2: Quantities used to diagnose γ_{IAV}, each displayed in the applied period. Anomalies of the global land carbon flux (a, b), global ocean carbon flux (c, d), and tropical near-surface temperature (e, f), calculated from the Historical simulation in the left panels and from the 1%COU simulation in the right panels, for CMIP5 models listed in Table 3.1

Table 3.4: Overview of the derived sensitivities γ_{LT} and γ_{IAV}, listed for each model. The uncertainty is given as the standard deviation of the mean. γ_{LT} was calculated according to Equation (3.9), as the difference of cumulated land carbon flux between the coupled (1%COU) and uncoupled (1%BGC) simulation and γ_{IAV} follows from the correlation between the global CO_2 IAV from land plus ocean carbon fluxes and tropical (30°N - 30°S) temperature IAV.

	Model	γ_{LT} (GtC K-1)	γ_{IAV} **Historical** (GtC y-1 K-1)	γ_{IAV} **1%COU** (GtC y-1 K-1)
A	CanESM2	-74.3	-7.4 ± 1.1	-16.2 ± 1.2
B	CESM1-BGC	-6.7	0.2 ± 1.1	-3.5 ± 0.8
C	GFDL-ESM2M	-116.4	-12 ± 1.6	-13.1 ± 2.1
D	HadGEM-ES	-60.2	-5.9 ± 0.7	-7.9 ± 1.5
E	IPSL-CM5A-LR	-22.9	-3.7 ± 1	-6.6 ± 1.6
F	MIROC-ESM	-58.4	-6.9 ± 1.7	-10.7 ± 1.4
G	MPI-ESM-LR	-78.3	-0.5 ± 0.9	-6.9 ± 0.6
H	NorESM1-ME	-7.2	-0.8 ± 0.9	-2.9 ± 0.7
I	OBS	-	-	4.9 ± 0.9

The observed γ_{IAV}, derived from the sum of the GCP land and ocean fluxes vs. the IAV of tropical (30°S - 30°N) temperature from NCDC data, yields a γ_{IAV} of -4.9 ± 0.9 GtCy-1 K-1 with a correlation coefficient of r = -0.60 (Figure Figure 3.3i). This compares with the value quoted by Cox et al. (2013) of 5.1 ± 0.9 GtCy-1 K-1, using a different method based on annual mean CO_2 concentrations rather than fluxes, and for a slightly longer period (1960-2010). GFDL-ESM2M and CanESM2 have the highest values of γ_{IAV} of -12 GtCy-1 K-1 and -7.4 GtCy-1 K-1 respectively (Figure Figure 3.3i). CESM1-BGC and NorESM1-ME show the smallest γ_{IAV}, 0.2 GtCy-1 K-1 and -0.8 GtC y-1 K-1, which is much lower than the observations. These two models also show weak correlation between CO_2 IAV and temperature IAV (r = 0.03 and r = -0.14, respectively).

Plotting γ_{LT} against γ_{IAV} reveals the emergent constraint identified by Cox et al. (2013), and this is done for both the Historical simulations and the 1%COU simulations (Figure 3.5) to test for robustness. In both cases there is evidence of a linear relationship between γ_{LT} and γ_{IAV}, that holds for all the models apart from MPI-ESM-LR. This model shows a surprising net negative correlation between variations in soil respiration and temperature, most likely due to a strong suppression of soil respiration under reducing soil moisture, which overwhelms the usual increase in soil respiration with warming (Reichstein et al., 2007; Zaehle et al., 2010; Ciais et al., 2005).

As a result MPI-ESM-LR has unusually high soil carbon in dry regions, which is vulnerable to climate change (Figure 3.5a). It therefore seems that MPI-ESM-LR does not fit on the γ_{IAV} vs. γ_{LT} correlation line (Figure 3.5a) as its short-term response is driven by different processes (the suppression of heterotrophic respiration by soil aridity) than the long-term response (decline in net primary productivity and hence in carbon storage). The MPI-ESM-LR model was excluded when calculating the best fit linear regression.

Interestingly, although both CESM1-BGC and NorESM1-ME include nitrogen limitations (Lawrence et al., 2011), these two models appear to fit the same line as the carbon-only models. This suggests that the inclusion of the nitrogen cycle does not change the relationship between the short and long-term responses of tropical land carbon to climate, even though these models yield much lower values of γ_{IAV} and γ_{LT}.

In the Historical experiment, the models can be constrained by the calculated observational estimate of γ_{IAV} = - 4.9 ± 0.9 GtC y-1 K-1. Without the observational constraint, all models would be equally likely to give the true γ_{LT} in both experiments, which is shown as the dashed
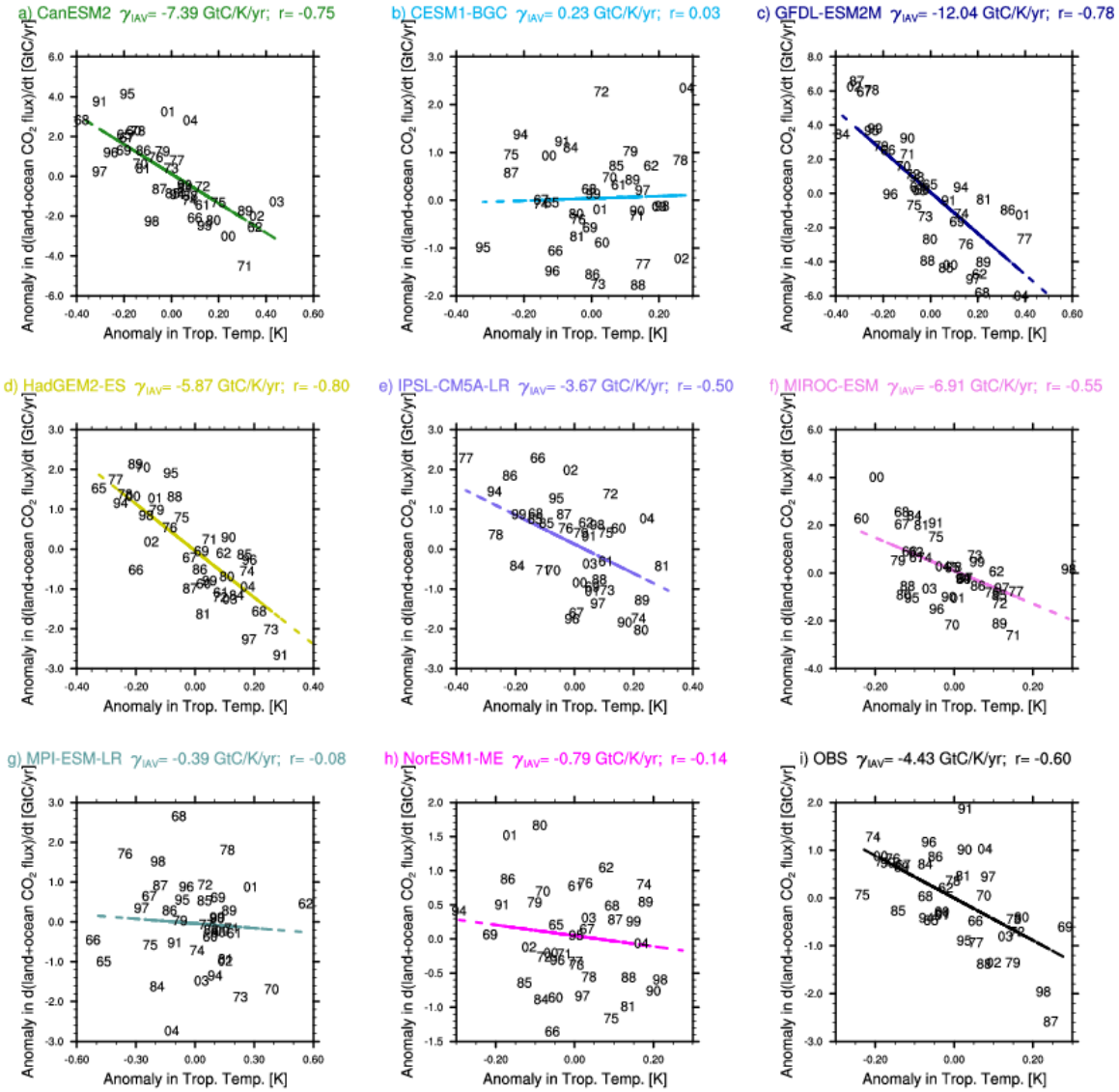
Figure 3.3: Correlation between the IAV of the sum of the global land and ocean CO_2 fluxes and tropical temperature from Historical, shown for each model and the observations. Numbers indicate single years and colored lines are the best fit linear regression excluding the years after volcanic eruptions.
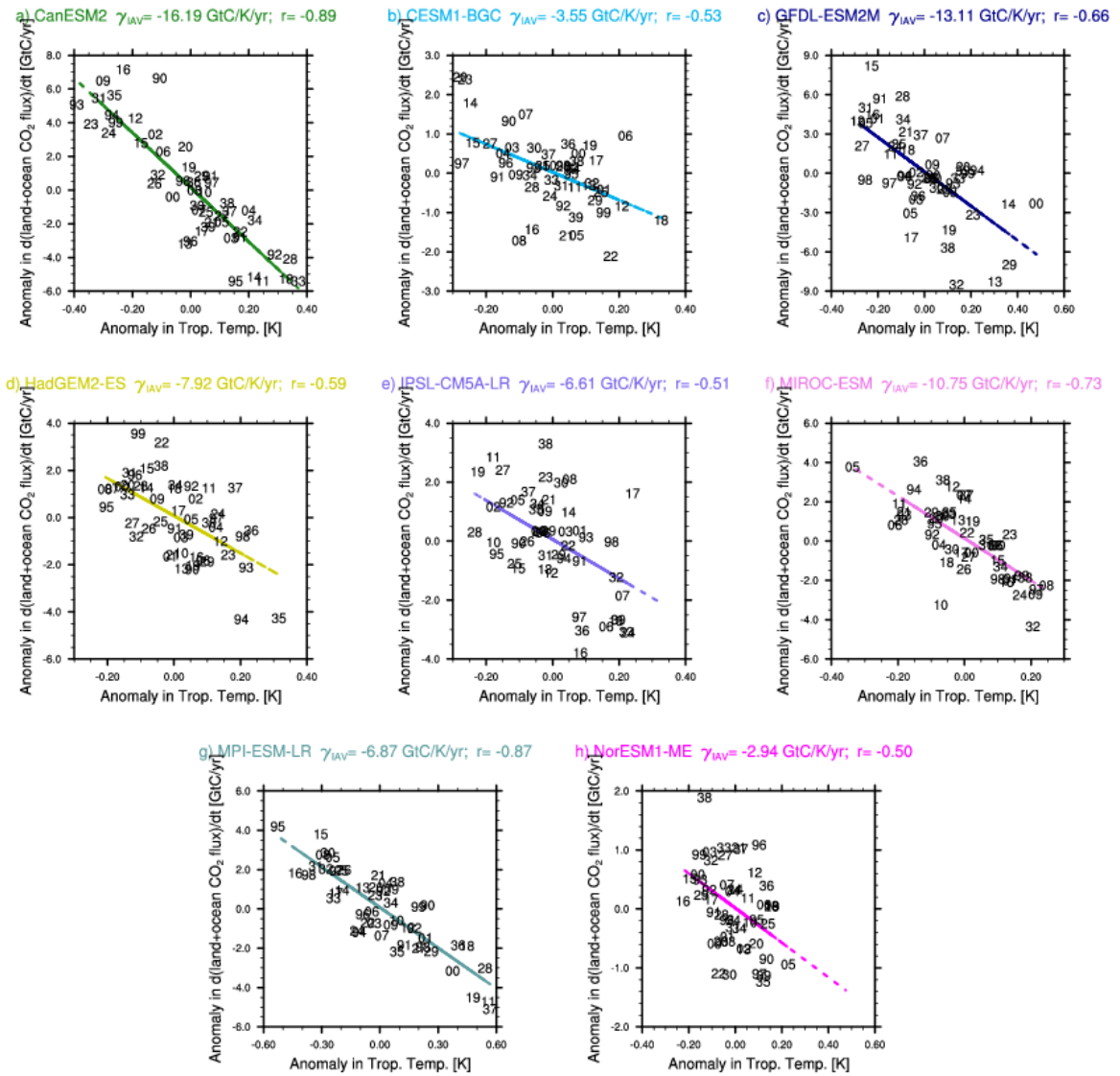
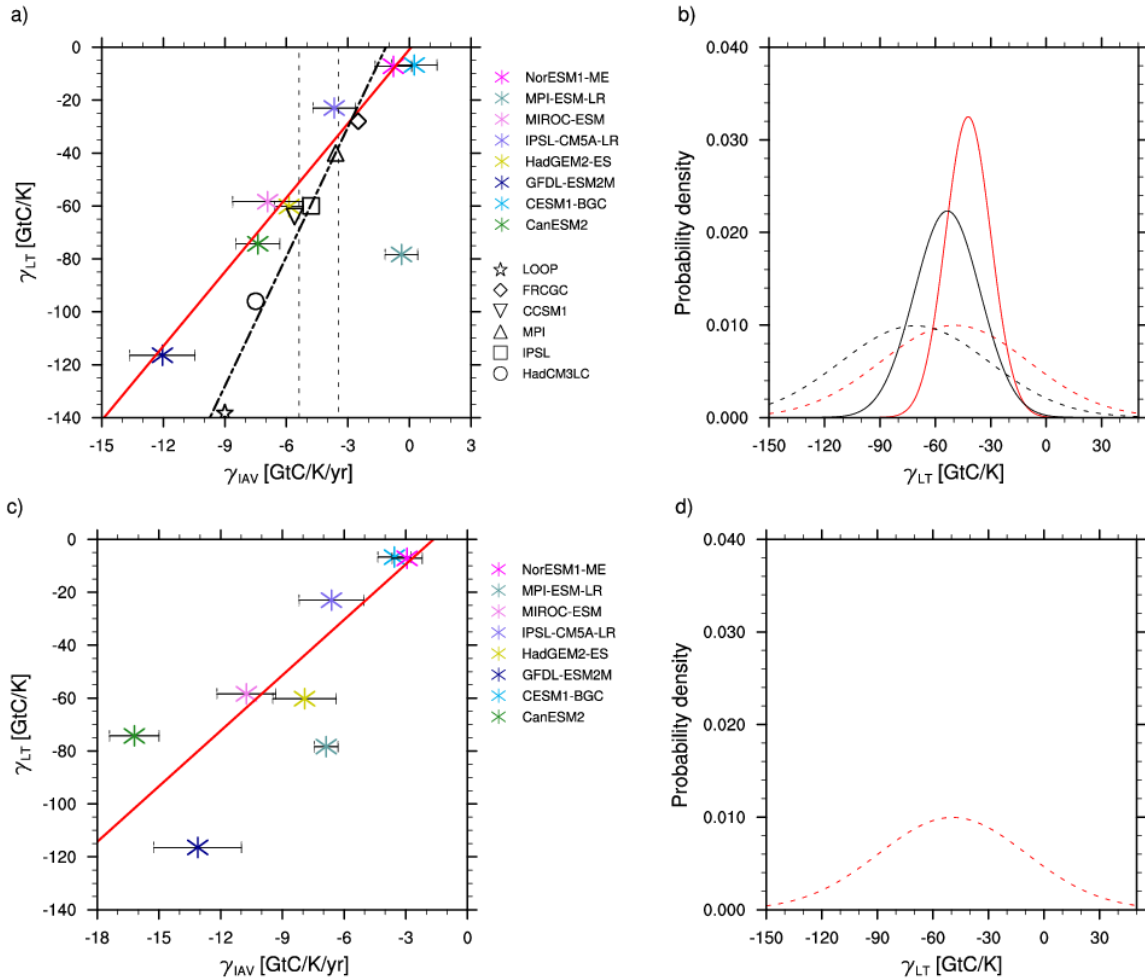Figure 3.4: As for Figure 3.3, but using 1%COU simulations. Note that there is no observation panel here

Figure 3.5: (a) γ_{LT} versus γ_{IAV} for the CMIP5 and C[4]MIP models. The red line shows the best-fit line across the CMIP5 models using the Historical simulation. The vertical dashed lines show the range of the observed γ_{IAV} according to Figure 3.3. (b) PDF for γ_{LT}. The solid line was derived after applying the IAV constraint to the models while the dashed line is the prior PDF derived purely from the models, before applying the IAV constraint. Red lines show PDFs for CMIP5 models and black lines and symbols are for C[4]MIP models. Panels (c, d) are as (a, b) but with γ_{IAV} calculated from the 1%COU simulations

red lines in Figure 3.5b and Figure 3.5d as a probability density function (PDF, calculated following Cox2013). Using the observed γ_{IAV} as constraint, a conditional PDF can be calculated. This is achieved by integrating over a contour PDF, which follows from multiplying the PDF of the observations and the PDF of the regression line. This conditional PDF gives a sharper peak with slightly less negative values and a much tighter range on the γ_{LT}. The conditional PDF gives γ_{LT} = -44 ± -14 GtC K-1, whereas the unconditional PDF gives γ_{LT} = -49 ± 40 GtC K-1 for the CMIP5 models in the Historical experiment (Figure 3.5b).

For comparison, six models from the Coupled Climate Carbon Cycle Model Intercomparison Project (C[4]MIP (Friedlingstein et al., 2006)), were also analyzed. For C[4]MIP the coupled and uncoupled simulations were forced by anthropogenic CO_2 emissions for the historical period, followed by anthropogenic emissions from the SRES A2 scenario (Nakicenovic et al., 2000).

To test for robustness, the results from the CMIP5 models are compare with the findings from Cox et al. (2013) who derived a similar constraint from C[4]MIP models (Figure 3.5a, black symbols). The correlation between γ_{LT} and γ_{IAV} across the C[4]MIP (r = 0.98) models is as tight as for the CMIP5 models but the slope is slightly different. Most importantly, the best-fit linear regression lines intercept close to the observational range and therefore give a similar emergent constraint on γ_{LT}. The calculated conditional PDF gives -53 ± -17 GtC K-1 for the C[4]MIP models as compared to -44 ± -14 GtC/K for the CMIP5 ESMs.

3.6 Summary and Discussion on the Carbon Cycle- Climate Feedback

An observation-based emergent constraint for the long-term sensitivity of land carbon storage to future climate warming (γ_{LT}) has been derived from an ensemble of eight ESMs participating in CMIP5. γ_{LT} cannot be directly derived from observations, yet it remains a key uncertainty in climate projections of the 21st century. A previous study by Cox et al. (2013) based on models participating in the Coupled Climate-Carbon Cycle Model Intercomparison Project (C[4]MIP) has already shown that the long-term climate sensitivity γ_{LT} is highly correlated with the short-term sensitivity of atmospheric carbon dioxide (CO_2) to temperature variability (γ_{IAV}).

In this thesis, a mathematical formulation for the emergent constraint between γ_{LT} and γ_{IAV} has been developed, which shows that the long- and short-term sensitivities are approximately related to each other through a timescale τ (Wenzel et al., 2014).

To test whether the emergent constraint holds in an ensemble different than C[4]MIP, a subset of eight ESMs was selected from the larger CMIP5 ensemble because the necessary output (surface downward CO_2 flux, carbon mass flux out of the atmosphere due to net biosphere production on land, and near-surface air temperature) was provided from two simulations with fully coupled carbon cycle (Historical and 1%COU) and one where the carbon cycles was insensitive to climate change (1%BGC). The first experiment is a historical simulation where the carbon cycle is fully coupled and CO_2 emissions calculated interactively (Historical). In the second simulation CO_2 is prescribed with a 1%/yr increase until quadrupling, starting at a preindustrial value of 285 ppmv (1%COU), except in one model (GFDL-ESM2M) where the forcing stabilized at a doubling of CO_2.

A tight correlation across the CMIP5 models between the sensitivity of land carbon storage to warming (γ_{LT}) and the short-term sensitivity of atmospheric CO_2 to tropical temperature variability (γ_{IAV}), is found. The only obvious divergence from the relationship is the MPI-ESM-LR model, which shows a unique positive correlation between anomalies in temperature and soil respiration, which seems at odds with observations. This model was therefore excluded from our linear regression. The two ESMs with an interactive nitrogen cycle (NorESM1-ME

and CESM-BGC) produce the lowest values of γ_{LT} along with unrealistically low values of γ_{IAV}, but still broadly fit the best fit emergent relationship.

Overall, a linear correlation between γ_{LT} and γ_{IAV} is derived from both the Historical and the 1%COU CMIP5 model ensemble, thus confirming previous results found for the C[4]MIP ensemble (Cox et al., 2013). However, this straight-line in the γ_{LT} and γ_{IAV} space has a different gradient in all three ensembles, owing to the different scenarios prescribed in each of these inter-comparison exercises. The timescale τ in the theoretical framework for the emergent constraint is therefore most likely related to the rate of climate change, which is largely determined by the particular scenario imposed for each of the ensembles.

Constraining both ensembles with observations results long-term sensitivities, γ_{LT}, that are very similar (CMIP5: -44 ± 14 GtC K-1 and C[4]MIP: -53 ± 17 GtC K-1). It therefore seems that this emergent constraint is robust to changes in the model ensemble, to the experimental design (i.e., whether the CO_2 concentration is prescribed or interactive), and to the scenario prescribed.

Chapter 4

Emergent Constraints on Carbon Cycle-CO$_2$ Concentration Feedback [1]

The carbon cycle-CO$_2$ feedback parameter β_L is the second unknown in Equation (2.4) of the terrestrial carbon store, as described in Section 2.3.1. It represents the sensitivity of the terrestrial carbon sink efficiency to elevated atmospheric CO$_2$ concentrations.

Uncertainties in the response of vegetation to rising CO$_2$ concentrations (Norby et al., 2005; Leakey et al., 2009) contribute significantly to the large spread in projections of future climate change (Friedlingstein et al., 2006; Ciais et al., 2013). Coupled climate-carbon-cycle models generally agree that elevated CO$_2$ will enhance GPP, but the magnitude of this fertilization effect varies widely among the models (Anav et al., 2013; Piao et al., 2013; Friedlingstein et al., 2014). Free-Air CO$_2$ Enrichment (FACE) experiments suggest that global models which neglect nutrient limitations over-estimate long-term CO$_2$ fertilization (Leakey et al., 2009). Such local manipulative experiments provide invaluable data to calibrate land models at specific sites, but are arguably too small-scale and site-specific to constrain the large-scale response simulated by global models (Zaehle et al., 2014).

Almost two decades ago it was hypothesised that increasing GPP was responsible for an observed increase in the amplitude of the CO$_2$ seasonal cycle at Mauna Loa (Keeling et al., 1996), but the subsequent non-monotonic variations in the CO$_2$ amplitude have prevented any attribution of these changes to CO$_2$ fertilization and other factors (Keeling et al., 1995; Barichivich et al., 2013; Graven et al., 2013). In Section 4.4 it is shown that the climate influence on the CO$_2$ amplitude is well correlated with the North Atlantic Oscillation (NAO), especially prior to 1995, and this allows isolating the CO$_2$ effect on the observed CO$_2$ amplitude at Mauna Loa.

Recent studies also suggest that variations in the CO$_2$ amplitude at Mauna Loa are at least partly due to changing agriculture in the mid-latitudes (Zhao & Zeng, 2014; Gray et al., 2014). In Section 4.3 therefore an Emergent Constraint is demonstrated on large-scale CO$_2$-fertilization of northern high latitude GPP based instead on observed changes in the seasonal cycle of atmospheric CO$_2$ at Poit Barrow (Graven et al., 2013), which is a high-latitude site much less affected by mid-latitude agriculture (Zhao & Zeng, 2014; Gray et al., 2014). The trend of the CO$_2$ amplitude at Poit Barrow is dominated by CO$_2$ fertilization, although its multi-annual variability is correlated with the Atlantic Multi-decadal Oscillation (AMO).

Using an identical approach to analyse historical simulations from the latest climate-carbon cycle models, it is possible to demonstrate that the magnitude of the inferred CO$_2$ effect on the CO$_2$ amplitude at each measuring site is linearly related to the magnitude of CO$_2$-fertilization of GPP, across the entire ensemble of models. When combined with the estimate of the CO$_2$ effect on the observed CO$_2$ amplitude, this relationship constitutes an Emergent Constraint on the CO$_2$ fertilization of GPP.

The aim of the study presented within this Chapter is to reduce the uncertainty in projected GPP increase, based on the observed trends in the CO$_2$ amplitude by applying an Emergent Constraint (Allen & Ingram, 2002; Hall & Qu, 2006; Cox et al., 2013; Wenzel et al., 2014).

---

[1]The contents of this chapter appears in similar form in the study of Wenzel et al. (2015a) that is under review in Nature.

This method utilizes common relationships between observables, such as the CO_2 seasonal cycle, and Earth System sensitivities, such as the CO_2 fertilization of the terrestrial carbon sink as described in Section 2.3, considering the full range of responses from an ensemble of complex ESMs.

4.1   Models, Simulations and Observations

Similar to Chapter 3, seven ESMs from the CMIP5 ensemble (Taylor et al., 2012) are used as well as the historical and the 1%BGC simulations are analyzed (see Table 3.2). It is focused on the seven ESMs in the CMIP5 archive for which outputs were available for both the historical and 1%BGC simulations.

Because of its molecular structure, CO_2 can be measured via infrared spectrometry. The concentration of CO_2 rich air in a cell is measured by its absorption of infrared radiation which is transmitted through the cell and detected. A higher CO_2 concentration absorbs more infrared radiation and leaves less to hit the detector. The National Oceanic and Atmospheric Administration/Earth System Research Laboratory (NOAA/ESRL, www.esrl.noaa.gov/gmd/ccgg /trends/) provide a global network of in-situ and flask measurements of atmospheric CO_2 concentrations. For this study observation data was used from the two measuring sites at Mauna Loa, Hawaii (MLO, 19.5°N 155.6°W, record time 1958 to 2013) and Point Barrow, Alaska (BRW, 71.3°N 156.6°W, record time 1974 2013). The observatories measure CO_2 concentrations as dry air mole fraction and are reported as daily means. The uncertainty of these measurements is derived as one standard deviation of the difference between monthly mean values measured independently by the Scripps Institute of Oceanography and NOAA/ESRL. The standard deviation corresponds to an uncertainty in the annual mean growth rate of 0.11 ppmv per year. These two stations provide the longest continuous record of atmospheric CO_2 measurements. CMIP5 model data was extracted for each grid box at the measuring sites, where for the MLO observatory CO_2 from the models boundary layer was used.

Records from other measuring sites or satellite retrievals, such as from SCIAMACHY (Schneising et al., 2014) are yet not long enough for the particular use as observational constraint. A long record of observations is however necessary for the method of the emergent constraint to calculate statistically reliable observational constraints on future Earth system sensitivities. Efforts such as the ESA Climate Change Imitative (CCI) creating long-term, homogenized dataset should open new possibilities for emergent constraint studies with satellite data in the future.

The observed first principal components of NAO and AMO (Pacific Decadal Oscillation (PDO), Arctic Oscillation (AO) and ENSO in the Fig. A9 and A10) were downloaded from NOAA/ESRL Climate Prediction Centre (CPC) (http://www.esrl.noaa.gov/psd/data/ climateindices/) for the time period of 1950 until present, and are based on observations.

4.2   Details on Diagnosing the CO_2 Fertilization and Observable CO_2-Effect

The long-term land carbon cycle-CO_2 feedback is expressed in this study as the CO_2 fertilization of GPP and is calculated as the fractional change of GPP over time in the 1%BGC simulation. The carbon cycle-CO_2 feedback parameter was diagnosed individually for all models for the northern hemispheric high latitudes (60°N - 90°N) and the extra tropics (30°N - 90°N) for a doubling of atmospheric CO_2 concentrations from the pre-industrial value of 285ppmv. Because not all models started the simulation at year zero, the fractional change was calculated from 5

year means between year 10 and year 70 and multiplied by a factor of 0.9 to account for the missing first 10% of CO_2 increase, which corresponds to 2x CO_2.

The amplitude of the seasonal cycle shows how much net CO_2 is taken up and released by land ecosystems throughout the year and is derived as the difference between maximum and minimum atmospheric CO_2 concentration for each year individually.

In order to extract the CO_2 fertilization effect of increasing atmospheric CO_2 concentrations $\Delta C_A(t)$ on the CO_2 seasonal cycle amplitude $\Delta C_{A,ampl}(t)$, both are correlated for the full records of observations (Section 4.1) and historical model simulation (1860 - 2005):

$$\Delta C_{A,ampl}(t) = a\Delta C_A(t) \tag{4.1}$$

In this study it is also investigated whether climate effects may change the diagnosed trend of the CO_2 seasonal cycle amplitude. For this approach a multiple linear regression was applied, including climate indices at one year time lag (t-1) as an additional predictor variable, to account for changes in the CO_2 seasonal cycle amplitude due to climate variability:

$$\Delta C_{A,ampl}(t) = a\Delta C_A(t) + Climate\ Index(t-1) \tag{4.2}$$

where the Climate Index is dependent on the analyzed observation site.

For the analysis using CO_2 observations at Poit Barrow the Climate Index of AMO was used (Section 4.3), which is defined as monthly anomalies of sea surface temperature in the area of the north Atlantic (0:60°N, 80°W:0°E) minus globally averaged (60°S:60°N) sea surface temperature anomalies.

For the analysis using observations at Mauna Loa the Climate Index of NAO was used (Section 4.4), being the first principal component of sea surface pressure averaged over the area of the north Atlantic (20:80°N, 90°W:40°E). The correlation between the NAO and the CO_2 seasonal cycle amplitude is only found for periods where the AMO is in its negative phase. Therefore only those years were sampled and included in the multiple linear regression.

For the models historical simulations were used starting in 1860 ending in 2005. The first principal component of NAO and AMO in the CMIP5 models were derived using the Climate Variability Diagnostic Package (CVDP) from NCAR (Phillips et al., 2014) as implemented into the Earth System Model Evaluation Tool (Eyring et al., 2015). For the second approach the CO_2 amplitude and the climate index time series were smoothed with a 3-year running mean, since both correlate well only on multi-annual time scales. We also tested correlations to other climate indices, such as the Pacific Decadal Oscillation (PDO) and El Nino / Southern Oscillation (ENSO), if they could explain some variability in the CO_2 amplitude, but found that these additional predictor variables did not significantly improve the fit to the observed amplitude variations (Figure A9 and A10 in Appendix A).

4.3   Emergent Constraint on High Latitude Gross Primary Productivity

Between 1974 and 2013 the atmospheric CO_2 concentration increased by about 75 ppmv at Poit Barrow (BRW: 71.3°N, 156.6°W) as a result of increasing anthropogenic CO_2 emissions (Ciais et al., 2013). On top of this increasing CO_2 trend, the uptake and release of carbon by the terrestrial biosphere throughout the year causes a seasonal cycle of CO_2 (Keeling et al., 1995). A change in the rate of photosynthesis (e.g., due to CO_2 fertilization) or decomposition (e.g., due to temperature variability) will therefore change the amplitude of CO_2 as measured in the atmosphere. In addition, changes in the phase lag between photosynthesis and decomposition,
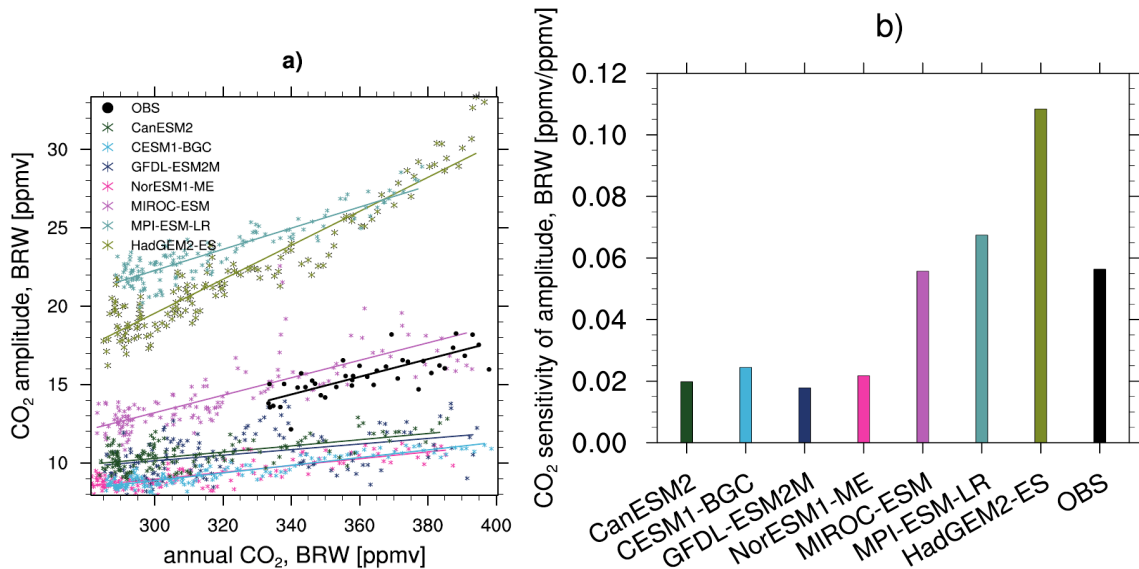
Figure 4.1: Comparison of observed and simulated CO_2 seasonal cycle amplitudes at BRW. (a) Correlation between annual mean atmospheric CO_2 vs. amplitudes of the seasonal cycle at BRW for observations (black) and CMIP5 historical simulations (colours). Markers show the correlations for the individual years and lines show the linear best fit for each model and observations. (b) Histogram showing the gradient of the linear correlations in panel (a). Correlations are derived between 1860 - 2005 from historical simulations for the models and 1974 - 2005 for the observations.

for example due to the effects of summer drying on photosynthesis or the effects of autumn warming on decomposition, can also change the amplitude of the CO_2 seasonal cycle.

Figure 4.1a compares the observed change in the amplitude of the annual CO_2 cycle (black markers) to that simulated by each of the seven CMIP5 models during their historical simulations. For clarity of our subsequent analysis, we have plotted the CO_2 amplitude against the annual mean CO_2 at BRW, for each of the models and for the observations. The observed CO_2 amplitude at BRW rises from about 13 ppmv to 18 ppmv over the available observational record from 1974 to 2013. The models simulate CO_2 amplitudes at BRW for current CO_2 concentrations (approx. 395 ppmv) which vary from about 12 to 30 ppmv. In general, the models also simulate an increase in the CO_2 amplitude, but the magnitude of this increase varies significantly from model to model, as shown by the linear regression lines on Figure 4.1a.

Figure 4.1b compares the gradient of these linear regression lines. The observations (black bar) suggest an increase in the CO_2 amplitude of about 0.06 ppmv per ppmv increase in annual mean CO_2. The models show a large range of trends in the CO_2 amplitude over a factor of five from about 0.02 to 0.11 ppmv per ppmv. Models with significant high-latitude vegetation greening (e.g., HadGEM2ES) give large increases in the CO_2 amplitude, while models with strong nitrogen-limitations on plant growth (CESM1-BGC, NorESM1-ME) typically show weaker trends. Overall, weaker trends of around 0.02 ppmv per ppmv are favoured by four out of the seven CMIP5 models.

In each of the models, the change in the CO_2 amplitude is highly correlated with the annual mean GPP from 60° to 90°N (Fig. A2). The interannual variability in the CO_2 amplitude at BRW is correlated with the AMO (Figure 4.2). The AMO strongly affects the northern hemisphere atmospheric circulation (Deser et al., 2010) and autumn and winter temperatures over the north American continent (Russell & Wallace, 2004; Knight et al., 2006), determining the extent of net CO_2 release and therefore the annual peak of CO_2 (Russell & Wallace, 2004). But from multiple linear regression (Equation (4.1)) it is clear that the most robust predictive model for the CO_2 amplitude (based on an adjusted R^2 measure) uses the annual mean CO_2
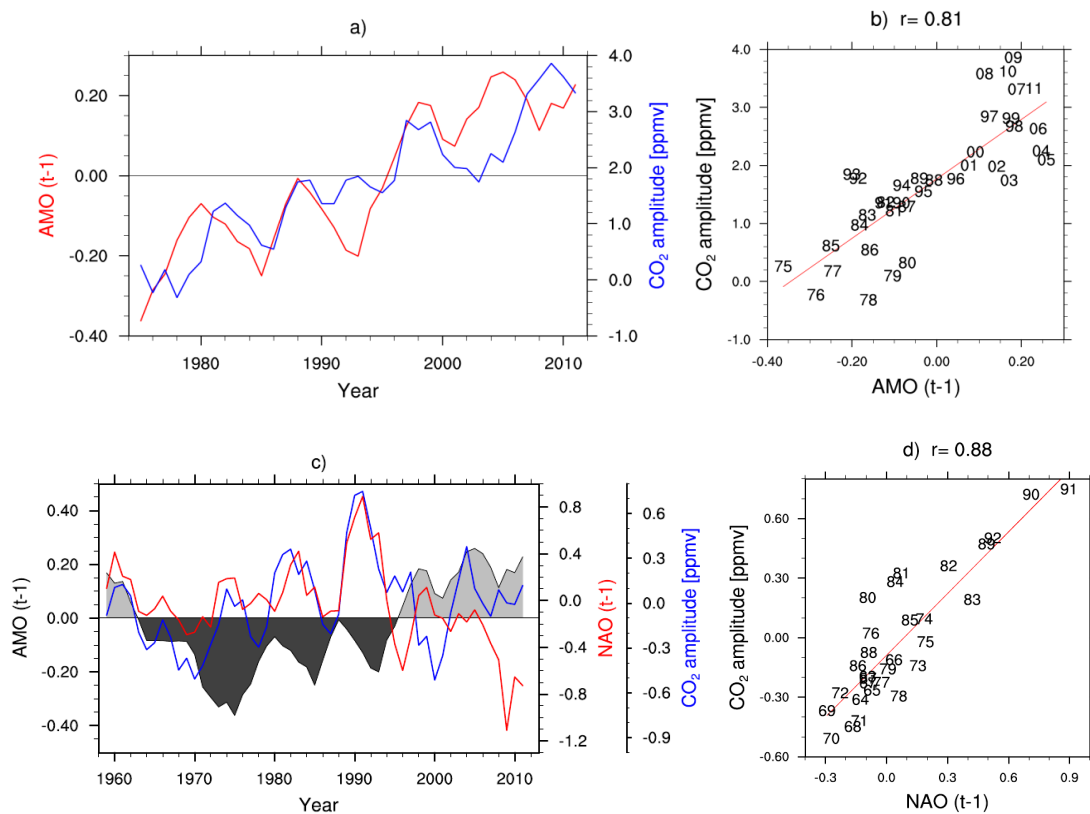
Figure 4.2: Comparison of observed CO_2 seasonal cycle amplitude with observed climate indices. Right panels show time series for the CO_2 seasonal amplitude observed at (a) Pt. Barrow and the AMO for the period between 1974 and 2013 and (c) Mauna Loa, the NAO and AMO for the period between 1960 and 2012, grey shaded areas indicate positive (light grey) and negative (dark grey) phases of AMO. Left panels show the corresponding correlation of CO_2 seasonal cycle amplitude versus (b) AMO and (d) NAO for the period where the AMO is in its negative phase, with one year time lag respectively. Numbers indicate the individual year of the correlation and correlation coefficient is given in the title.

concentration as it is only a predictor variable (Table 4.1).

The implication of this is that the models agree that the trend in the CO_2 amplitude at BRW is indeed indicative of a trend in high-latitude GPP, which opens up the possibility of an Emergent Constraint (Chapter 2.3) on future changes in GPP. As models predominantly simulate changes in GPP as a response of photosynthesis to CO_2 (Fig. A3), this also offers the promise of a constraint specifically on CO_2 fertilization. Figure 4.3 shows the extent of CO_2 fertilization in these same models until the time of doubling CO_2 from the 1%BGC runs. The fractional increase in high latitude GPP due to doubling CO_2 in these models varies from 20 to 60%, with four of the seven models giving values of less than 25% (Figure 4.3b). There is a clear similarity to the histogram showing the sensitivity of the CO_2 amplitude at BRW to CO_2 (Figure 4.1b).

The linear relationship between the CO_2-effect on the CO_2 amplitude at BRW and the relative GPP increase at the time of CO_2 doubling for the CMIP5 models is shown in Figure 4.4a, with a correlation coefficient of r = 0.98. Models that simulate a large trend in the CO_2 amplitude at BRW therefore also predict a large high latitude GPP increase in the future. The combination of the observed changes of the seasonal cycle and this model-based linear relationship, creates an Emergent Constraint on the magnitude of CO_2 fertilization in the real world. In the absence of this constraint, the prior probability density function (PDF) for the CMIP5 model spread is shown as the black histogram in Figure 4.4b, implying a modal CO_2-fertilization effect of a 20 to 60% increase in GPP due to a doubling of CO_2. The observed
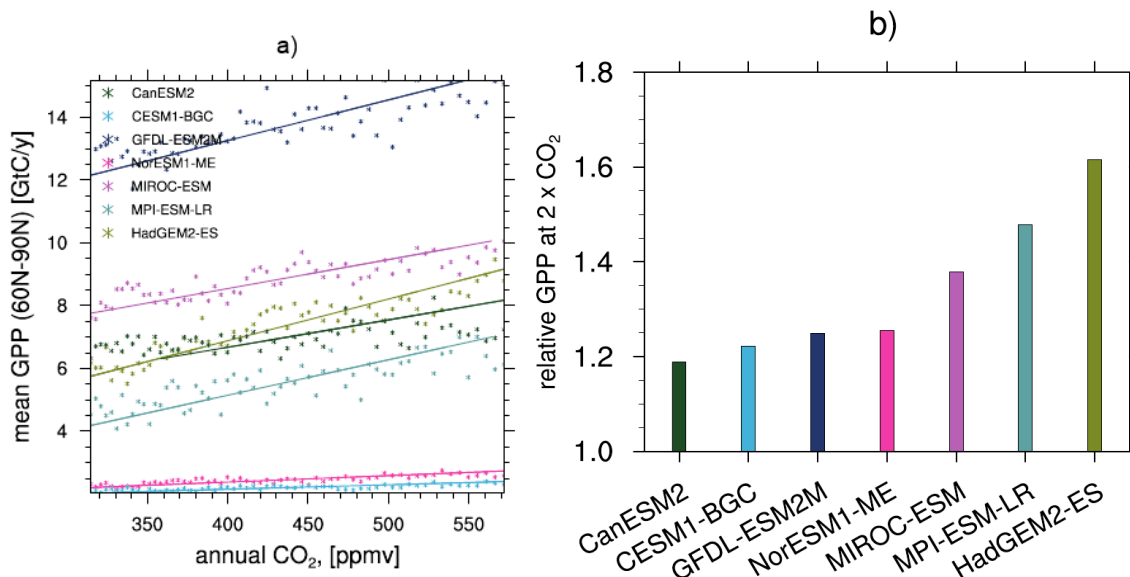
Figure 4.3: Comparison of simulated high latitude GPP increase. (a) Correlation between annual mean atmospheric CO$_2$ vs. amplitudes of the seasonal cycle at BRW for observations (black) and CMIP5 historical simulations (colors). Markers show the correlations for the individual years and lines show the linear best fit for each model and observations. (b) Histogram showing the gradient of the linear correlations in panel (a). Correlations are derived between 1860 - 2005 from historical simulations for the models and 1974 - 2005 for the observations.

range of the CO$_2$-effect at BRW allows a conditional PDF to be calculated, by convolving the probability contours around the best-fit straight-line in Figure 4.4a with the uncertainty in the observed sensitivity of the BRW CO$_2$ amplitude to annual mean CO$_2$ concentration (Cox et al., 2013; Wenzel et al., 2014). This Emergent Constraint implies a reduced range of uncertainty for the CO$_2$-fertilization effect, with a central estimate of $39 \pm 9\%$.

Models without nitrogen limitations span the full range of possible CO$_2$ fertilization within the CMIP5 ensemble for 20 to 60% while the current models which include nitrogen limitations appear to underestimate it (20 - 25%). This study therefore strongly supports efforts to improve the representation of nutrient limitations in climate-carbon cycle models (Zaehle et al., 2014). For comparison, the FACE experiments suggest an NPP increase of about 23% when averaged across four sites with approximately 1.5 times the current (375 to 550 ppmv) CO$_2$ concentration (Norby et al., 2005), which is about 0.13 %/ppmv. Our larger-scale constraint therefore implies a very similar CO$_2$ fertilization of photosynthesis in the future (approximately 0.14%/ppmv).

4.4   Emergent Constraint on Extra-Tropical Gross Primary Productivity

The non-monotonic variations in the CO$_2$ seasonal amplitude at Mauna Loa are more complex (Fig, A5a), and there are recent papers suggesting that these variations are in part due to changes in mid-latitude agriculture (Zhao & Zeng, 2014; Gray et al., 2014).

Between 1958 and 2014 the atmospheric CO$_2$ concentration increased by about 75 ppmv at Mauna Loa (MLO: 19.5°N;155.6°W). The observed 3-year mean CO$_2$ amplitude rises from about 5 ppmv to 6 ppmv from the beginning of the record in 1960 until the early 1990s. From then onwards there is no obvious upward trend, although variability in the amplitude remains evident throughout the record.
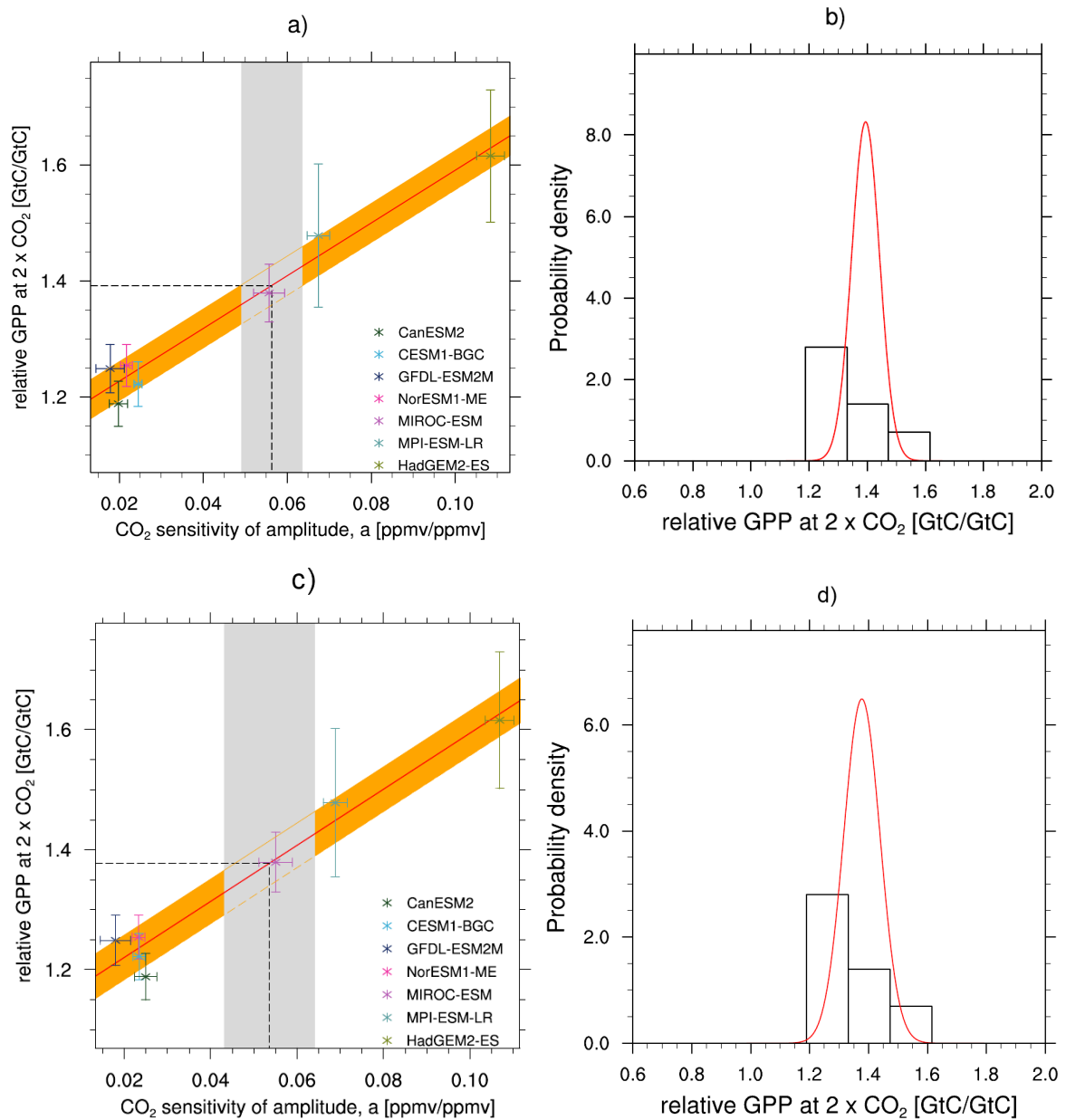
Figure 4.4: Emergent constraint on projected fractional increase high latitude GPP at 2xCO$_2$. Correlation between the CO$_2$-effect resulting from the multiple linear regression of (a) annual CO$_2$ only and (b) additionally including AMO to the CO$_2$ seasonal cycle amplitude at BRW and the fractional change of high latitude (60°N - 90°N) GPP at 2xCO$_2$. The gray shading shows the observational range and the solid red line the linear best fit across the CMIP5 ensemble together with the prediction error of this regression (orange shading). The black dashed line points to the observationally constraint value of the fractional change of GPP. Error bars show the standard deviation for the individual models. (b and d) Probability density functions for the unconstrained (black) multi model mean projected fractional change of GPP and after applying the observational constraint to the relationship (red) shown in (a) and (c), respectively.
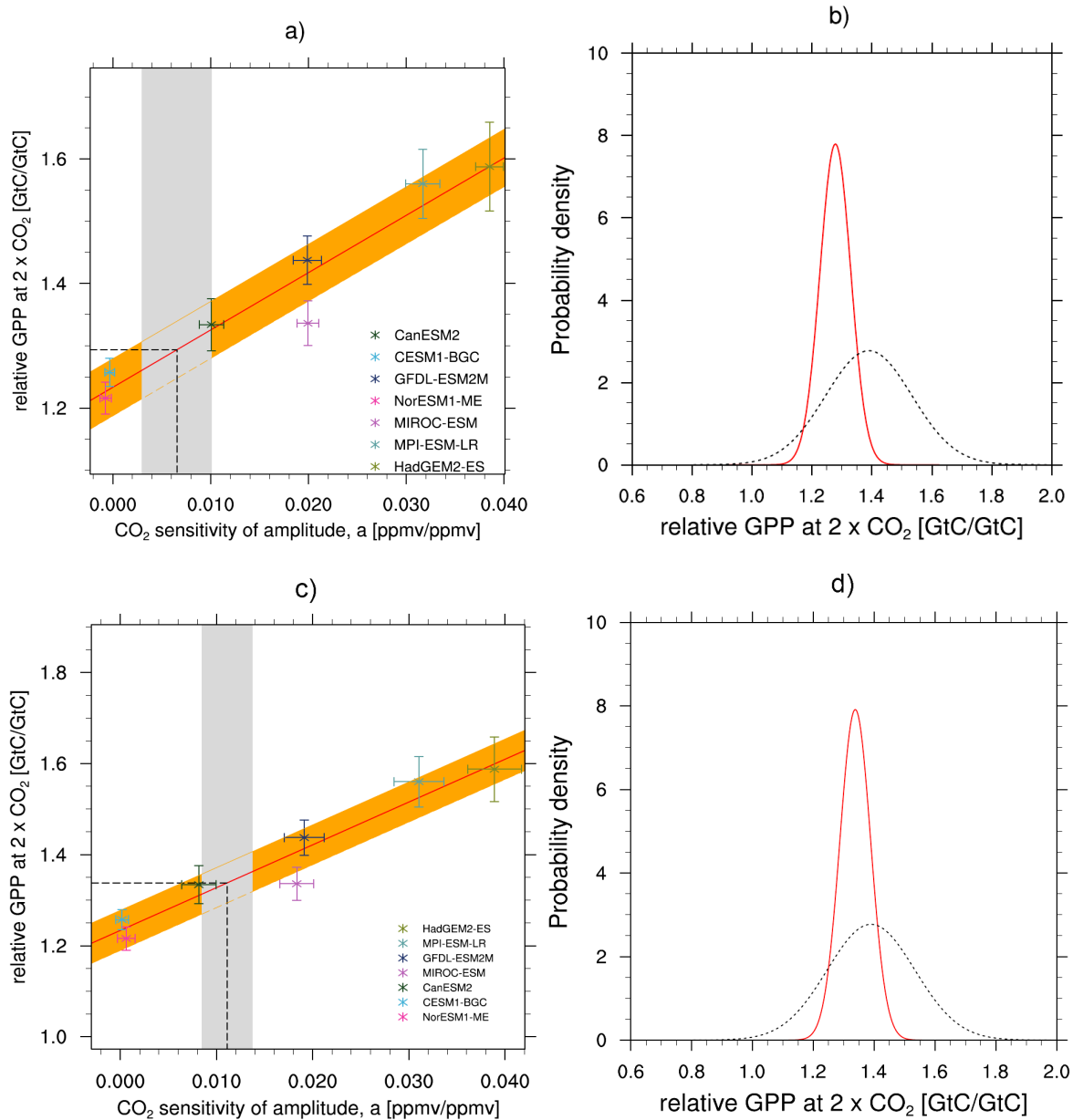
Figure 4.5:   Emergent constraint on projected fractional increase extra tropical GPP at $2xCO_2$ Correlation between the CO_2-effect at MLO resulting from the multiple linear regression and the fractional change of extra tropical GPP at $2xCO_2$. In panel (a) the CO_2 effect was extracted using annual CO_2 increase only as predictor variable for the CO_2 amplitude at, and in panel (c) it was inferred from the predictor variables of CO_2 and the NAO climate index at negative AMO phases, in both panels correlations are shown to extra tropical GPP at $2xCO_2$. The grey shading shows the observational range and the solid red line the linear best fit across the CMIP5 ensemble together with the prediction error of this regression (orange shading). The black dashed line points to the observationally constraint value of the fractional change of GPP. Error bars show the standard deviation for the individual models. (b and d) Probability density functions for the unconstrained (black) multi model mean projected fractional change of and after applying the observational constraint to the relationship (red) shown in (a) and (c), respectively.

Table 4.1: Summary data for high latitude carbon cycle-CO_2 feedback and present-day diagnostics. The fractional change of high latitude GPP was calculated using the 1%BGC simulation for a doubling of CO_2 and are listed for the individual models of the CMIP5 ensemble. The regression coefficients result from multiple linear regression Equation (4.1) and are calculated from historical simulations of the CMIP5 models between 1860 and 2005, and for Poit Barrow between 1974 - 2005.

Models	Fract. change of extra tropical carbon cycle-CO_2 feedback	Regression coefficients from multiple linear regression		adjusted R^2	
		Offset to initial amplitude, a_0 [ppmv]	CO_2 sensitivity of amplitude, a [ppmv/ppmv]	Predictor variable CO_2 only	Predictor variable CO_2 + AMO
CanESM2	1.18 ± 0.03	4.34 ± 0.68	0.02 ± 0.002	0.36	0.18
CESM1-BGC	1.22 ± 0.04	1.52 ± 0.31	0.02 ± 0.001	0.81	0.55
GFDL-ESM2M	1.25 ± 0.04	4.78 ± 1.10	0.02 ± 0.003	0.16	0.07
HadGEM2-ES	1.62 ± 0.11	-12.98 ± 1.07	0.11 ± 0.003	0.88	0.79
MIROC-ESM	1.38 ± 0.05	-3.51 ± 1.18	0.06 ± 0.004	0.62	0.35
MPI-ESM-LR	1.48 ± 0.12	2.05 ± 0.86	0.07 ± 0.003	0.81	0.58
NorESM1-ME	1.25 ± 0.04	2.43 ± 0.44	0.02 ± 0.001	0.62	0.29
OBS	-	-7.52 ± 2.11	0.06 ± 0.011	0.60	0.79

The observed changes in the CO_2 amplitude however are very well correlated with the NAO (Figure 4.2) prior to 1995 (r = 0.86, P = 0.00001), when the AMO is in its negative phase. Previous studies have demonstrated that during this period mainly CO_2 rich air from Eurasia is sampled at MLO during autumn to spring (Buermann et al., 2007; Lintner et al., 2006; Russell & Wallace, 2004). Eurasian autumn and winter temperatures are also strongly affected by north Atlantic modes such as the NAO pattern, which determines the extent of net CO_2 release and therefore the annual peak CO_2 (Russell & Wallace, 2004). Consistent with this, the variability in the CO_2 seasonal amplitude is strongly correlated with NAO prior to 1995, with a one year time lag (Figure 4.2d).

However, post-1995 the correlation between NAO and the CO_2 seasonal cycle amplitude is much weaker. This is when the AMO changes to its positive phase (Figure 4.2c). The AMO is characterized by warm and cold patterns of sea surface temperature in the northern Atlantic, which strongly affects the northern hemisphere atmospheric circulation (Deser et al., 2010) and causes a change in the transport pathways reaching MLO (Lintner et al., 2006; Buermann et al., 2007). To develop an observationally-based constraint on future GPP increase due to CO_2 fertilization, the analysis therefore is restrict to time periods of negative AMO, which supports the westerly surface winds at mid-latitudes caused by strong meridional pressure gradient which is defining the NAO (Hurrell, 1995; Russell & Wallace, 2004).

Once this climate-driven variation is accounted for, a CO_2-effect on the CO_2 amplitude is diagnosed of about 0.01 ppmv per ppmv from the Mauna Loa record (Fig. A5b). For comparison, the models give between 0 and 0.04 ppmv/ppmv for the same sensitivity coefficient (Fig. A5a). When looking across the model ensemble, again it is found that the sensitivity of the CO_2 amplitude to the annual mean CO_2, is approximately linearly related to the magnitude of the CO_2 fertilization of GPP, but now for the extra tropics ($30° - 90°$N, Figure 4.5). This provides an emergent constraint on CO_2 fertilization of extra tropical GPP of a 24 - 44% due to doubling CO_2, which overlaps heavily with the estimate derived above for BRW (30 - 48%).

This consistency is pleasing, although the BRW estimate are more robust as it does not suffer from the complications of agricultural change or climate variability in the mid-latitudes.

Table 4.2: Summary data extra tropical carbon cycle-CO_2 feedback and present-day diagnostics. The fractional change of GPP was calculated using the 1%BGC simulation for a doubling of CO_2 and are listed for the individual models of the CMIP5 ensemble. The regression coefficients result from multiple linear regression as described in Section 4.2 and are calculated from historical simulations of the CMIP5 models between 1860 and 2005, and for Mauna Loa between 1960 - 2005.

Models	Fract. change of extra tropical carbon cycle-CO_2 feedback	Regression coefficients from multiple linear regression			adjusted R^2	
		Offset to initial amplitude, a_0 [ppmv]	CO_2 sensitivity of amplitude, a [ppmv/ppmv]	Climate sensitivity of amplitude, b [ppmv/Climate index]	Predictor variable CO_2 only	Predictor variable CO_2 + NAO_{-AMO}
CanESM2	1.33 ± 0.04	1.49 ± 0.58	0.008 ± 0.002	-0.12 ± 0.22	0.31	-0.22
CESM1-BGC	1.26 ± 0.02	2.83 ± 0.23	0.000 ± 0.001	-0.28 ± 0.14	-0.004	-0.03
GFDL-ESM2M	1.44 ± 0.04	-1.17 ± 0.67	0.019 ± 0.002	0.51 ± 0.37	0.58	0.61
HadGEM2-ES	1.59 ± 0.07	-7.22 ± 0.90	0.039 ± 0.003	0.38 ± 0.32	0.84	0. 72
MIROC-ESM	1.34 ± 0.04	-0.43 ± 0.57	0.018 ± 0.002	0.13 ± 0.23	0.70	0.63
MPI-ESM-LR	1.56 ± 0.06	1.16 ± 0.82	0.031 ± 0.003	-0.14 ± 0.33	0.70	0.68
NorESM1-ME	1.21 ± 0.03	3.61 ± 0.29	0.001 ± 0.001	-0.03 ± 0.13	0.005	-0.02
OBS	-	1.94 ± 0.89	0.011 ± 0.003	0.63 ± 0.12	0.03	0.76

4.5   Summary and Discussion on the CO_2 fertilization of Gross Primary Productivity

This study, which is currently under review in Nature Wenzel et al. (2015) represents the first large-scale constraint on the extent to which additional atmospheric CO_2 fertilizes plant growth, which is one of the key unknowns in future climate-carbon cycle projections. A much improved estimate of CO_2-fertilization in the high latitudes and extra tropical ecosystems is demonstrated, using the observed changes in the amplitude of the CO_2 seasonal cycle at Poit Barrow and at Mauna Loa along with results from CMIP5 climate-carbon cycle models to produce an emergent constraint.

The trend in the CO_2 seasonal cycle amplitude on interannual time scales can be understood as the combination of the response of the carbon cycle to annually increasing CO_2 concentration plus the response to climate variability. The trend of the CO_2 amplitude at Poit Barrow is dominated by CO_2 fertilization, although its multi-annual variability is correlated with the AMO. In a similar manner historical simulations from the latest climate-carbon cycle models were analyzed and shown that the magnitude of the inferred CO_2 effect on the CO_2 amplitude at each measuring site is linearly related to the magnitude of CO_2-fertilization of GPP, across the entire ensemble of models. Adding the estimate of the CO_2 effect on the observed CO_2 amplitude the relationship can be used to observationally constrain the CO_2 fertilization of GPP. For the high latitude ecosystem a CO_2-fertilization of 30 - 48% increase of GPP due to a doubling of atmospheric CO_2 was estimated, which significantly narrows the range of uncertainty compared to the CMIP5 model ensemble.

This is consistent with the emergent constraint, found for the extra tropical GPP (24 - 44%),

which was derived from observations at Mauna Loa. However, extracting the CO$_2$ fertilization effect on the CO$_2$ amplitude required to develop a statistical model, which also includes the response of the seasonal cycle to climate variations. The measured changes in the CO$_2$ seasonal cycle at Mauna Loa are well correlated with the NAO (especially prior to 1996). This is due to the NAO affecting autumn and winter temperatures in Eurasia which determines the extent of seasonal CO$_2$ release and therefore the annual peak CO$_2$. Underneath this NAO dependence is a discernible effect of CO$_2$ on the seasonal cycle, consistent with some degree of CO$_2$ fertilization.

However, the analysis for high latitude ecosystems is more robust, because the changing CO$_2$ seasonal cycle is less sensitive to changes in agriculture in the mid-latitudes (Zeng et al., 2014), thus the changes in the CO$_2$ amplitude are indicative of changes in the GPP of natural vegetation, rather than changes in agriculture vegetation (Gray et al., 2014). Additionally the near monotonic increase in the CO$_2$ seasonal cycle amplitude allows to directly inferring the CO$_2$ fertilization effect.

The study therefore has great relevance to the changing functioning of the terrestrial carbon cycle and the implications for future climate change. It suggests that most current models are too pesimistic in projecting large increases in the land carbon storage due to CO$_2$ fertilization, and highlights the urgent need to improve the representation of nutrient limitations in next generation models.

Chapter 5

Emergent Constraints on the Position of the Austral Jet Stream [1]

As discussed in the Scientific Background of the SH circulation (see Section 2.5), uncertainty in the circulation response to anthropogenic forcing remains a pressing problem in climate projections (Shepherd, 2014). The CMIP5 models simulate a wide spread in the austral jet position trends in both the historical and future scenarios, particularly in austral summer (Eyring et al., 2013; Gerber & Son, 2014). Because of the strong influence of SH jet stream position on carbon and heat uptake (e.g., Waugh et al., 2013) and regional impacts on temperatures and precipitation (e.g., Kang et al., 2011; Thompson et al., 2011), it is therefore important to provide reliable projections of future summer austral jet position trends.

Historical trends in the austral jet stream have been largest in austral summer (Marshall, 2003), as the circulation has been impacted by two anthropogenic forcings in this season: stratospheric ozone loss and GHG increase (Arblaster & Meehl, 2006). Ozone depletion led to radiative cooling of the lower stratosphere over Antarctica in the late 20th century and strongly impacted the SH extra tropical circulation, shifting the jet stream poleward (Gillett & Thompson, 2003; Son et al., 2010). The recovery of ozone is expected to have the opposite effect as ozone depletion, thus tending to shift the jet equatorward (Perlwitz et al., 2008; Son et al., 2008). Increasing GHGs appear to drive a poleward expansion of the jet streams in both hemispheres (Yin, 2005), and controlled double CO_2 experiments suggest that the response of the jet in the SH is strongest in austral summer (Kushner et al., 2001).

The balance between ozone recovery and increasing GHGs will influence future austral jet position (Son et al., 2008; Arblaster et al., 2011). While ozone appears to have dominated the response in the past (Polvani et al., 2011), the balance in the future depends in part on the speed of ozone recovery and the strength of future greenhouse gas emissions (Son et al., 2010; Simpkins & Karpechko, 2012; Barnes & Polvani, 2013; Eyring et al., 2013). Even for a given forcing scenario, however, there is still considerable spread. Amongst the CMIP5 models, Gerber & Son (2014) found that in a moderate carbon future, as characterized by the RCP4.5 scenario, differences in ozone changes contributed most significantly to the spread in future climate projections. There was also considerable spread associated with processes independent of the thermodynamic trends; however, suggesting that uncertainty in the dynamical response to temperature trends also plays a role in model spread.

CMIP5 models differ substantially in their ability to simulate the basic climatology and trends of the 20th century (Eyring et al., 2013). The austral circulation has long presented a particular challenge to climate models, with substantial biases in the basic position and variability of the jet stream (e.g., Kidston & Gerber, 2010; Swart & Fyfe, 2012). These biases have significant implications; for example, Bracegirdle et al. (2015) emphasize that a model's ability to represent the austral circulation is one of the most important factors influencing future projections of the Antarctic climate.

In this study, relationships between models' ability to simulate the historical climate and their ability to simulate the future are diagnosed, with an ultimate goal of better discriminating

---

[1]The contents of this chapter appears in similar form in the study of Wenzel et al. (2015b), Constraining Future Summer Austral Jet Stream Positions in the CMIP5 Ensemble by Process-oriented Multiple Diagnostic Regression. Journal of Climate.

amongst their projections of the future. This relates to the question whether the ordinary arithmetic ensemble mean, i.e. the "one-model-one-vote" approach (Knutti et al., 2010a) gives the best estimate of future austral jet position. The MDER methodology of Karpechko et al. (2013) is used to relate future projections to process-oriented diagnostics based on the 20th century in order to see if one can improve on the uMMM projection of future climate.

Only the main diagnostics are included that have been linked to the austral jet position in the recent literature, which are discussed in Section 5.1. Section 5.2 then outlines the observational and reanalysis constraints on these diagnostics and lists the CMIP5 models used in this study. In Section 5.3, MDER is used to improve projections of the position of the jet stream in the near-term (2015 - 2034) and mid-term (2040 - 2059). The study is concluded in Section 5.4 with a discussion of the results.

5.1   Key Process-Oriented Diagnostics

Several processes have been linked to the austral jet position in the literature. For most diagnostics, both the climatological value (denoted by _c) and the linear trend (denoted by _t) over the observation period is included, which is defined to be 1979 - 2005. An exception is the meridional gradient of Absorbed Shortwave Radiation (ASR) diagnostic (ASR-SH), which was defined only for a shorter period (2000 - 2005) due to the lack of observations before 2000. The choice of 1979 - 2005 restricts the study to the satellite era, where there is some confidence in the reanalysis, and ends with the historical scenario in the CMIP5. The precise definition of each diagnostic, its value in the reanalysis/observational data set, and its multimodel mean value from the CMIP5 ensemble are listed in Table 5.1. The values from each individual model and the observational or reanalysis datasets are presented in the supporting information (Figures B1 to B11 in Appendix B).

In the list below the inclusion of each diagnostic in into the analysis is briefly justified. Note, however, that the vast majority of the diagnostics will not ultimately be utilized by MDER to predict future jet position. This is largely due to the fact that many diagnostics are correlated with each other (e.g., biases in the climatological position of the jet stream are highly correlated with biases in the natural variability; Kidston & Gerber (2010)). The abbreviated short names in the list below are used in the figures and are specified again in Table 5.1.

Table 5.1: Description of the diagnostics, reanalysis or observational data used to constrain the models, their mean value and uncertainty for the diagnostic, the corresponding value in the CMIP5 ensemble, and a reference. The substring "t" denotes the trend of this diagnostic and the substring "c" the climatological mean calculated for the period 1979 - 2005, except for the ASR-SH diagnostic, which was calculated for the period 2000 - 2005.

Short Name	Diagnostic	Reanalysis/ Observations	Reanalysis/ Observational Value	CMIP5 Mean ± Stddev	References
Impact of Antarctic Ozone Depletion on the Position of the Jet Stream					
T-SP_t	Trends and climatological means in ONDJ polar stratospheric temperatures at 100 hPa over Antarctica (60 - 90°S)	ERA-Interim (Dee et al., 2011)	-1.17 ± 0.63 K/dec	-1.40 ± 0.72 K/dec	Figure 10d of Eyring et al. (2013); Figure 10 of Gerber & Son (2014)
T-SP_c	As above	As above	219.47 ± 0.51 K	218.17 ± 2.75 K	
O3-SP_t	Trends and climatological means in SOND ozone at 50 hPa over Antarctica (60 - 90°S)	BDBP (Hassler et al., 2009)	-0.42 ± 0.05 ppmv/dec	-0.32 ± 0.10 ppmv/dec	Figure 10c of Eyring et al. (2013)
O3-SP_c	As above	As above	2.02 ± 0.077 ppmv	2.49 ± 0.23 ppmv	
Impact of GHG warming and climate sensitivity on the position of the jet stream					
T-NGlob_t	Trends and climatological means in annual mean near-global (82.5°S - 82.5°N) temperature at 100 hPa	ERA-Interim (Dee et al., 2011)	-0.14 ± 0.062 K/dec	-0.09 ± 0.09 K/dec	Figure 10b of Eyring et al. (2013)
T-NGlob_c	As above	As above	204.47 ± 0.05 K	205.88 ± 1.43 K	
O3-NGlob_t	Trends and climatological means in annual-mean near-global (NG, -82.5°S - 82.5°N) ozone at 50 hPa	BDBP (Hassler et al., 2009)	-0.13 ± 0.017 ppmv/dec	-0.05 ± 0.02 ppmv/dec	Figure 10a of Eyring et al. (2013)
O3-NGlob_c	As above	As above	2.08 ± 0.02 ppmv	2.20 ± 0.13 ppmv	
T-Trop_t	Trends and climatological means in DJF upper tropospheric tropical (30°S - 30°N) temperatures at 250 hPa	ERA-Interim (Dee et al., 2011)	0.29 ± 0.09 K/dec	0.38 ± 0.13 K/dec	Figure 10f of Eyring et al. (2013); Figure 10 of Gerber & Son (2014)
T-Trop_c	As above	As above	230.67 ± 0.08 K	229.23 ± 1.68 K	

	Description	Dataset			Reference
U-Jet_t	Trends and climatological means in DJF SH jet position at 850 hPa	ERA-Interim (Dee et al., 2011)	-0.79 ± 0.32 lat/dec	-0.45 ± 0.48 lat/dec	Figure 10e of Eyring et al. (2013)
U-Jet_c	As above	As above	-50.02 ± 0.27 lat	-48.49 ± 2.32 lat	
H-SH_t	Trends and climatological means of the location of the SH Hadley cell boundary defined by zero Ψ at 500 hPa	ERA-Interim (Dee et al., 2011)	-0.65 ± 0.18 lat/dec	-0.26 ± 0.22 lat/dec	Figure 5e of Son et al. (2010)
H-SH_c	As above	As above	-36.27 ± 0.17 lat	-35.59 ± 1.59 lat	
P-SH_t	Extratropical zonal mean tropopause pressure integrated south of 50°S	ERA-Interim (Dee et al., 2011)	-0.16 ± 0.07 hPa/dec	-0.32 ± 0.17 hPa/dec	Figure 5c of Son et al. (2010)
P-SH_c	As above	As above	280.11 ± 0.62 hPa	252.18 ± 13.77 hPa	
SAM-efold_c	e-folding time scale of southern annular mode in the troposphere	ERA-Interim (Dee et al., 2011)	12 ± 0.84 days	24.19 ± 10.21 days	Figure 1c of Kidston & Gerber (2010)
ASR-SH_c	Meridional gradient in ASR throughout the atmosphere	CERES-EBAF (Doelling et al., 2013)	136.38 ± 16.83 index	130.78 ± 6.57 index	Ceppi et al. (2014)
Impact of Antarctic Sea-Ice on SH winds and the position of the jet stream					
SIE-SP_t	Trends of annual mean Antarctic sea-ice extent	NSIDC (Cavalieri et al., 2006)	0.068 ± 0.109 10^6km^2/dec	-0.04 ± 0.05 10^6km^2/dec	Figure 3b of Stroeve et al. (2012)
SIE-SP_c	As above	As above	12.17 ± 0.06 10^6km^2	11.15 ± 4.38 10^6km^2	

O3-SP: Stratospheric ozone at 50 hPa, averaged over the south pole, directly captures differences in the strength of the ozone hole and recovery (Eyring et al., 2013). Many models used the Cionni et al. (2011) dataset generated by SPARC, a few models interactively simulated ozone, and others used data sets generated by related Chemistry Climate Models.

O3-NGlob: The near global mean ozone at 50 hPa diagnostic provides a complementary measure of ozone loss and recovery, and impacts near-global lower stratospheric temperatures trends in particular (Eyring et al., 2013).

T-SP: South Polar stratospheric temperature at 100 hPa is another indicator of ozone change (depletion/recovery). Due to differences in models radiation schemes and dynamical feedbacks, models with the same ozone can simulate different thermal trends despite having the same underlying ozone. The radiative cooling in the lower stratosphere due to ozone depletion results in an enhanced temperature gradient in the upper troposphere/lower stratosphere (UTLS), and therefore accelerates the austral jet (Wilcox et al., 2012). Gerber & Son (2014) found variance in T-SP to be a significant source of spread in CMIP5 models in both the historical and future scenario integrations.

T-NGlob: The near global mean temperature at 100 hPa is again a complementary measure of stratospheric trends, seeking to identify differences between the models that are not confined to the polar cap.

T-Trop: Changes in upper troposphere temperatures in the tropics at 250 hPa influence temperature gradients in the UTLS (Wilcox et al., 2012), and were also a key driver of model spread in the analysis of Gerber & Son (2014). Upper-tropospheric temperatures in the tropics are influenced by both changes in surface temperatures and changes in the atmospheric stability.

U-Jet: The historical DJF SH jet position at 850 hPa has been found to correlate with a models response (Kidston & Gerber, 2010). This could reflect geometric constraints on the circulation (Barnes & Polvani, 2013) and/or differences in the dynamics of the jet with latitude (Garfinkel et al., 2013). Recent trends in the jet also provide a measure of how sensitive the jets are to forcings, and may also reflect natural variability, as discussed in Section 2.5.

H-SH: Along with U-jet, the latitude of the SH Hadley cell boundary defined by zero Ψ at 500 hPa gives us information about circulation biases and trends associated with ozone depletion over the past period (Son et al., 2010), where Ψ denotes the meridional stream function.

P-SH: A decrease in extratropical zonal mean tropopause pressure integrated south of 50°S is associated with warming of the troposphere and cooling of the lower stratosphere (two signatures of global warming) and has been strongly linked to the position of the extratropical jet streams (Lorenz & DeWeaver, 2007).

SAM-efold: The e-folding time scale of a models' SAM in the troposphere characterizes the strength of interactions between baroclinic eddies and the extratropical jet stream (Lorenz & Hartmann, 2001; Gerber et al., 008a). Fluctuation dissipation theory suggests that the time scales of natural variability may be related to the response to external forcing (Gerber et al., 008b; Ring & Plumb, 2008), and there is evidence for this in comprehensive climate models (Kidston & Gerber, 2010; Son et al., 2010; Barnes & Polvani, 2013).

ASR-SH: Ceppi et al. (2014) link changes in the jet stream to changes in the meridional gradient of SH ASR. Changes in the ASR gradient can force changes in the equator-to-pole temperature gradient, directly impacting the baroclinicity of the atmosphere.

SIE-SP: Changes and biases in the climatological mean sea-ice extent in the Southern Ocean impact the local energy budget, and could influence the equator-to-pole temperature gradient (Stroeve et al., 2012; Ceppi et al., 2014; Bracegirdle et al., 2015).

5.2   Models, Observations and Reanalysis Data

The MDER method, as described in detail in Section 2.3.1, was applied to 28 models of the CMIP5 ensemble, as listed in Table 5.2, created and run by 18 different modeling centers. Many centers provided multiple ensemble member integrations of the same model and scenario. All available ensemble members were used, which helps reducing the impact of natural variability. In order not to bias the MDER method towards models which ran more ensemble integrations, we first average all ensemble members for each individual model together prior to the calculations. Hence MDER only sees one historical and future (RCP4.5) time series for each model. Only models that provided output for all process-oriented present-day diagnostics are included into the analysis, because the method does not allow for missing values (Karpechko et al., 2013).

As detailed in Section 2.1, historical simulations are extended by four RCP scenarios, defined by their approximate total radiative forcing in 2100 relative to 1750 (Moss et al., 2010; van Vuuren et al., 2011) and cover the period between 2006 and 2100. The future trends in the austral jet position were calculated from monthly means from the RCP4.5 scenario integrations, since for near and mid-term time horizons the analysis yield similar results (not shown). The present-day diagnostics were calculated from the monthly mean CMIP5 historical simulations, in general for the period 1979 - 2005 (see details in Table 5.1) and results are shown in the supplementary material. Each of the present-day diagnostics is compared with monthly mean reanalysis data or observations as listed in Table 5.1.

Since direct measurements cannot cover the whole globe or provide a continuous record, reanalysis data fills these missing values. These data sets are produced by global models which are nudged with observations (Dee et al., 2011). Direct measurements are used in the diagnostics where available, but for many diagnostics only on meteorological reanalysis could be used. For the evaluation, monthly means for the period 1979 - 2005 are used except for the zonal means of net balanced climatology TOA fluxes which are only available for the period 2000 - 2014. A list of the reanalysis and observations used in this study is given in Table 5.1 and briefly described below.

Monthly mean surface temperature, zonal and meridional wind fields, pressure and daily mean surface pressure were obtained from the global atmospheric reanalysis ERA-Interim (Dee et al., 2011). Reanalysis fields are available from 1979 until present and are continuously updated. The data has a spatial resolution of approximately 80 km on 60 vertical levels from the surface up to 0.1 hPa (Berrisford et al., 2011). Note that trend estimates based on reanalyses data should be taken with caution, due to changes in the measurement system (i.e., the addition of new satellites). We discuss the trend diagnostics singled out by the MDER method in more detail in Section 5.3.1.

From the Binary Data Base of Profiles (BDBP; http://www.bodekerscientific.com/) monthly mean vertical ozone profiles were downloaded. They were constructed by fitting a regression model to each of the 70 pressure levels of ozone measurements (Hassler et al., 2009). The BDBP regression model accounts for seven fit coefficients (including the seasonal cycle, linear trend,

age-of-air dependent equivalent effective stratospheric chlorine, Quasi-biennial Oscillation) plus a residual.

The Clouds and the Earth's Radiant Energy System (CERES; http://ceres.larc.nasa.gov/index.php) Earth Radiation Budget Experiment (EBAF) were designed for evaluating the radiative budgets of models and the meridional heat transport. From CERES-EBAF data monthly mean zonal means of net balanced climatology TOA fluxes was used. The fluxes are available between 2000 and 2014, but the observational record was limited to the period from 2000 - 2005 to allow direct comparison with the CMIP5 historical runs.

Monthly mean sea ice concentrations were obtained from the National Snow and Ice Data Center (NSIDC; http://nsidc.org/data/seaice/pm.html), which is generated from satellite brightness temperature data (Cavalieri et al., 2006). The data is on a 25 x 25 km grid and available from 1978 onwards.

5.3   Results of the MDER Analysis

To highlight how the most important factors constraining the jet stream evolve in time, the MDER algorithm is applied to two time horizons. First it is focused on the jet position in the near-term from 2015 - 2034. A twenty-year period was selected to reduce the influence of natural variability in the jet stream. Over this short time horizon, no significant changes in anthropogenic forcings occur in the RCP4.5 scenario, so the method is expected to focus on correcting biases in the historical climatologies. Second the method is then focused on a mid-century projection, 2040 - 2059, a time when the stratospheric ozone and greenhouse gas concentrations have changed.

5.3.1   Near-Term Projections of the Austral Jet Position

Figure 5.1a shows the absolute value of the correlation coefficients between the short-term projection of the austral jet position and 20 process-oriented present-day diagnostics. The coefficients reveal a strong correlation between the climatological mean of the historical austral jet position (U-Jet_c) and the near-term projection of the austral jet position. The correlation coefficient is near unity with a tight uncertainty envelope, as quantified by the 95% confidence interval. Models simulating the jet too far equatorward in the historical simulations (which can be seen in Figure B6) also do so for the near-term future, and vice versa. The high correlation between the historical and the projected austral jet position will cause the MDER algorithm to recognize and correct for this well-known equatorial bias in the CMIP5 model ensemble.

The climatological mean of the Hadley cell boundary (H-SH_c, Appendix B Figure B7) position (r = 0.90) and trend (r = 0.58) are also highly correlated with the jet position from 2015 - 2034, although the relationship is of opposite sign for the trend. Biases in the position of the SH Hadley cell mirror biases in the extratropical jet stream (Son et al., 2010; Arblaster & Meehl, 2006), such that the first relationship is strongly linked to the connection with the historical jet position U-Jet_c discussed above. At face value, the negative correlation between the near-term jet position and the trend in the SH Hadley cell position (H-SH_t) suggests that models which saw more expansion of the tropics in the late 20th century tend to have a more equatorward jet in coming decades. Given that the near-term jet is so highly correlated with the jet in the past, this could reflect the fact that models with an equatorward bias in their climatology are more sensitive to external forcing (and so exhibited larger trends in the 20th century), as found by Kidston & Gerber (2010) for future jet shifts. The late 20th century trend in the jet stream itself, U-Jet_t is also negatively correlated with the 2015 - 2034 jet position, albeit more weakly. It remains unclear why the trend in the Hadley cell is more strongly associated with jet position than the trend in the jet itself.

Table 5.2: Overview of CMIP5 models that are used in this study together with the number of ensembles and which concentration scenarios were simulated by each model.

| Nr.	Models	Modeling Center	Ensemble members	Main Reference
01	ACCESS1-0	Center for Australian Weather and Climate Research, Australia	1	(Dix et al., 2013)
02	ACCESS1-3		1	
03	bcc-csm1-1	Beijing Climate Center, China Meteorological Administration, China	1	(Wu, 2012)
04	bcc-csm1-1-m		1	
05	BNU-ESM	College of Global Change and Earth System Science, Beijing Normal University, China	1	
06	CanESM2	Canadian Center for Climate Modelling and Analysis, Canada	5	(Arora et al., 2011)
07	CCSM4	National Center for Atmospheric Research, USA	5	(Meehl et al., 2012)
08	CESM1-BGC	Community Earth System Model Contributors	1	(Gent et al., 2011)
09	CESM1-CAM5		3	
10	CMCC-CMS	Centro Euro-Metiterraneo per I Cambiamenti Climatici, Italy	1	(Vichi et al., 2011)
11	CNRM-CM5	Centre National de Recherches Meteorologiques, France	1	(Voldoire et al., 2013)
12	CSIRO-Mk3-6-0	Commonwealth Scientific and Industrial Research Organization in collaboration with Queensland Climate Change Center of Excellence, Australia	10	(Rotstayn et al., 2012)
13	FGOALS-g2	LASG, Institute of Atmospheric Physics, Chinese Academy of Sciences and CESS, China	1	(Li et al., 2013)
14	GFDL-CM3	NOAA Geophysical Fluid Dynamics Laboratory, USA	1	(Donner et al., 2011)
15	GFDL-ESM2G		1	(Dunne et al., 2013)
16	GFDL-ESM2M		1	
17	HadGEM2-AO	National Institute of Meteorological Research, Korea Meteorological Administration, Korea	1	(Martin et al., 2011)
18	Inmcm4	Russian Institute for Numerical Mathematics, Russia	1	(Volodin et al., 2010)
19	IPSL-CM5A-LR	Institut Pierre Simon Laplace, France	4	(Dufresne et al., 2013)
20	IPSL-CM5A-MR		1	
21	IPSL-CM5B-LR		1	
22	MIROC5	Japan Agency for Marine-Earth Science and Technology, Atmosphere and Ocean Research Institute (The University of Tokyo), and National Institute for Environmental Studies, Japan	3	(Watanabe et al., 2011)
23	MIROC-ESM		1	
24	MIROC-ESM-CHEM		1	
25	MPI-ESM-LR	Max Planck Institute for Meteorology, Germany	3	(Giorgetta et al., 2013)
26	MPI-ESM-MR		3	
27	MRI-CGCM3	Meteorological Research Institute Japan	1	(Yukimoto et al., 2012)
28	NorESM1-M	Norwegian Climate Centre, Norway	1	(Iversen et al., 2012)
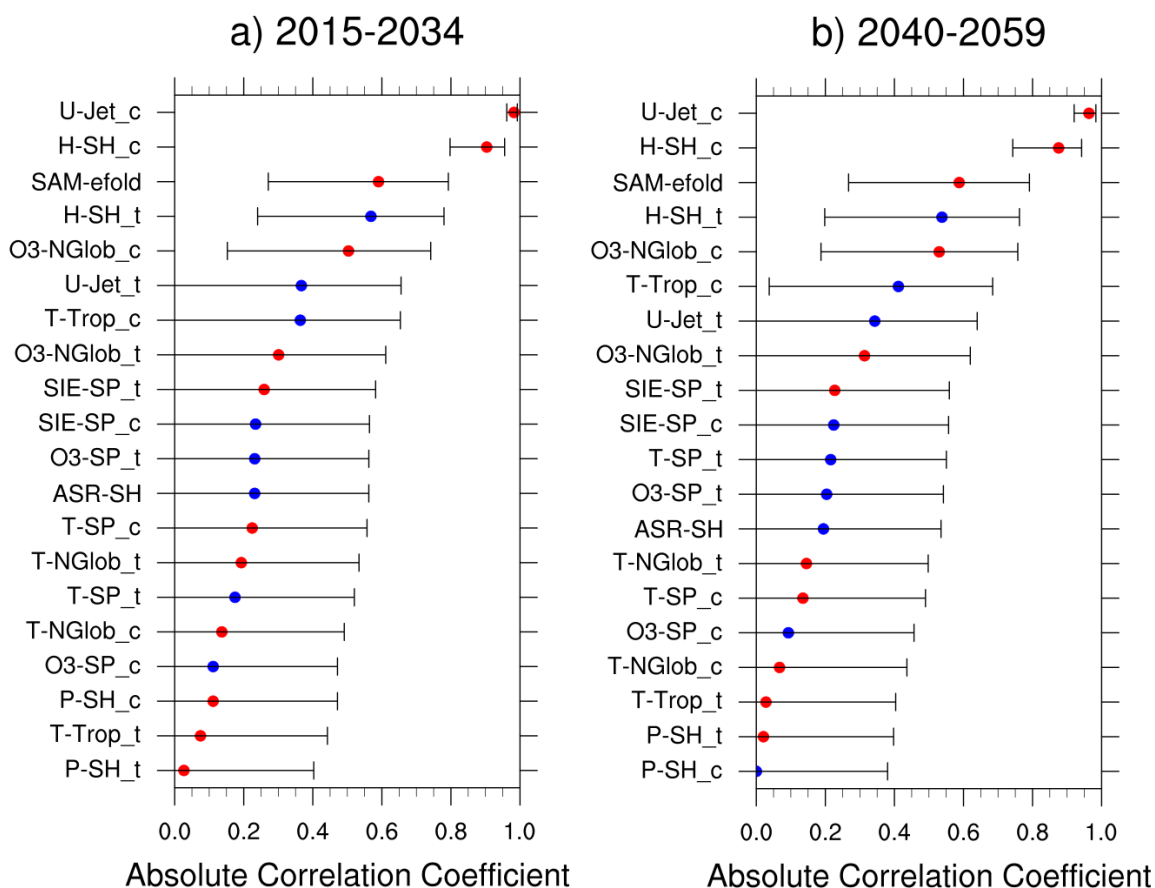
Figure 5.1: Absolute values of the correlation coefficient between future austral jet position and present-day diagnostics as listed in Table 1 across the CMIP5 model ensemble (see Table 5.2), for (a) the near-term austral jet position climatological mean (2015 - 35) and (b) the mid-term austral jet position climatological mean (2040 - 59). Error bars show the 95% confidence intervals for the correlation coefficients. Colored markers indicate positive (red) and negative (blue) correlations.

The e-folding time scale of SAM (SAM-efold, Appendix B Figure B10) also exhibits a statistically significant positive correlation (r = 0.59) with the near-term projection of the austral jet. As in the case of the Hadley cell, the SAM e-fording time scale is linked to the historical jet position U-Jet_c (e.g., Kidston & Gerber, 2010), and so again may be a manifestation of the same relationship. Since the H-SH and SAM-efold diagnostics ultimately provide somewhat redundant information compared to the diagnostic U-Jet_c, the MDER algorithm rejects them from the regression model.

The diagnostic of near global climatological mean ozone (O3-NGlob_c, Appendix B Figure B1) shows the fifth highest correlation, and the link is statistically significant (r = 0.50) at the 95% confidence level. The correlation could reflect that fact that models which experienced larger ozone loss over the historical period (and so exhibit a climatology with less ozone) also experienced a stronger ozone hole, and so a poleward shift in the jet stream (Eyring et al., 2013).

The remaining correlations in Figure 5.1a are not statistically significant at the 95% level of the linear regression. In general, however, diagnostics indicating biases in the SH circulation climatology show a stronger correlation to the near-term austral jet stream position than diagnostics which characterize trends over the historical period.

From all the diagnostics included, the MDER algorithm creates a parsimonious regression model to predict the near-term austral jet position, focusing exclusively on the diagnostic U-Jet_c, as shown in Figure 5.2a. The model is simply -1.36 + 0.98 x U-Jet_c. In essence, the algorithm detects the equatorward bias of the CMIP5 models in the jet stream in the past and
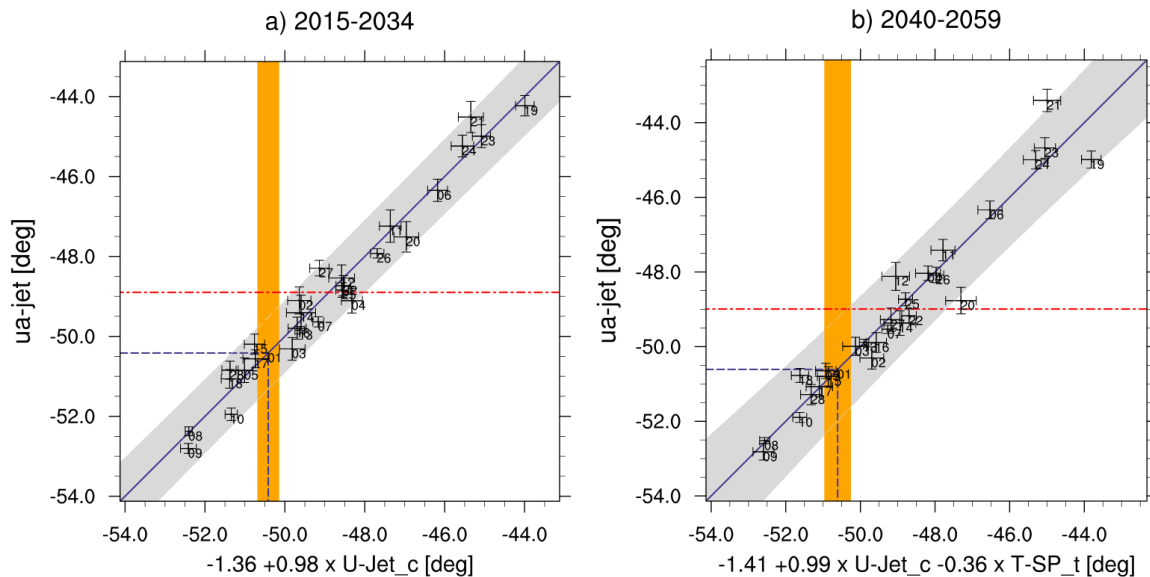
Figure 5.2: Scatter plot showing the correlation between the future austral jet position and (a) the quantity (-1.36 + 0.98 x U-Jet_c) for the near term climatological mean (2015 - 34) and (b) the quantity (-1.41 +0.99 x U-Jet_c - 0.36 x T-SP_t) for the mid-term climatological mean (2040 - 59). Numbers indicate estimates of simulated climatological mean values of each CMIP5 model and the error bars show one standard deviation of the means, calculated from seasonal means. The solid blue line shows the least squares linear fit to the CMIP5 model ensemble and the gray shading marks the 95% confidence interval for the least squares linear regression. The orange shading indicates one standard deviation of the observed climatological mean values calculated using historical values. The red dotted line shows the unweighted ensemble mean (uMMM) and the blue dashed line the MDER prediction.

provides a correction to the future projection. As the result depends on a single parameter, Figure 5.2a can be compared quite easily with the schematic diagram in Section 2.3.1. MDER focuses on the nearly perfect correlation between the historical jet position (U-Jet_c) and jet location in 2015 - 2034. The uMMM projection puts the jet at 48.9°S (red horizontal line), but knowing that the historic jet was biased in the CMIP5 models (located on average at 48.5 instead of 50.0°S), MDER suggests that it should also be 1.5° poleward of the uMMM in 2015 - 2034, at 50.4°S, as indicated by the blue dashed lines.

While the result is almost trivial, this is the first time, to my knowledge, that projections of the future multi-model jet position have been bias corrected. Taking the uMMM would place the jet at 48.9°S over the period 2015 - 2034, substantially equatorward of its current position in reanalysis. MDER suggests that it should be at 50.4°S, just a bit poleward of its current location.

Cross validation of the results indicates that MDER can reduce uncertainty in the jet projection. This is realized by comparing the results of future austral jet position estimates with the MDER method against the uMMM in pseudo reality, following Karpechko et al. (2013). The root mean squared projection error (RMSE) of the near-term austral jet positions is nearly an order of magnitude lower using the MDER method compared to uMMM (Figure 5.3; $\text{RMSE}_{MDER} = 0.42$ deg; $\text{RMSE}_{uMMM} = 2.37$ deg). This dramatic drop in uncertainty in the cross-validation can be understood more easily by viewing time series of the jet position, shown in Figure 5.4. In the cross validation test with an uMMM methodology, one is effectively seeking to predict one model's jet position (i.e., the pseudo reality) using the positions projected by all the other models. The RMSE_{uMMM} thus reflects the spread in the mean jet position from 2015 - 2034, a spread on the order of degrees. The errors are large because the uMMM cannot successfully predict cases when the pseudo reality is an outlier model. With MDER, however,
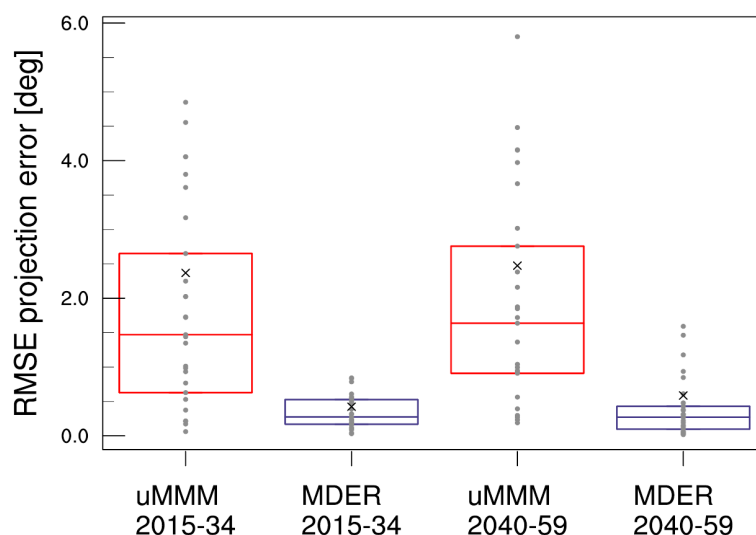
Figure 5.3: Root mean squared error (RMSE) differences between the ensemble-mean future climatological mean (2015 - 34 and 2040 - 2059) austral jet position and the future climatological mean austral jet position in pseudo reality for each pseudo reality considered (grey circles) under the RCP4.5. The ensemble mean is calculated for each scenario from the unweighted model mean (uMMM, red boxes) and the MDER method (blue boxes). The cross indicates the RMSE for each case and the boxes show the 25th - 75th percentiles across the error ensemble. The bars inside the box indicate the median of the ensemble.

it is explicitly taken into account information on the historical jet position in the model chosen as the pseudo reality, and only use the other models to estimate the jet shift between 1979 - 2005 and 2015 - 2034. For this short time horizon, the forced signal is small, on the order $1/10^{ths} of a degree$.

It should be emphasized that the RMSE error bounds obtained in the cross-validation exercise provide nice illustration of the actual prediction errors associated with uMMM and MDER. Formal estimates of the prediction errors from the full model ensemble further demonstrate how the prediction uncertainty is reduced by MDER in comparison to uMMM. Based on 28 realizations of climate change under the RCP 4.5 scenario, the 95% confidence intervals for MDER and uMMM methods are 0.8 or 4.8 deg correspondingly. Here, the MDER error is calculated in a standard way as confidence interval for the response variable of regression (Karpechko et al. (2013, e.g.,), Eq. 6). For uMMM the corresponding confidence interval is given by $t_{(1+\widetilde{p})/2)} \times s$ where s is the standard deviation across individual model projections, $t_{(1+\widetilde{p})/2)}$ is the $(1+\widetilde{p})/2)$ quartile of t distribution and $\widetilde{p} = 0.95$. The MDER uncertainty is calculated assuming perfect knowledge of the observed diagnostics.

A more realistic uncertainty bound should reflect both uncertainty in the multi-model estimate of the climate signal (in case of MDER, uncertainty in the change between 1979 - 2005 and 2015 - 2034), and uncertainty associated with calculation of the diagnostics. The latter is affected by reanalysis errors and internal variability. While reanalysis errors can only be estimated qualitatively (see discussion in Section 5.4), the influence of the internal variability can be directly incorporated into the prediction uncertainty. In 27 years of reanalysis, the mean jet can only be bounded to the range 50.0 ± 0.5 deg with 95% confidence. When uncertainty associated with internal variability is taken into account (by the law of error propagation) the uncertainty of MDER prediction becomes 1 deg., still considerably less than the uncertainty of uMMM method.
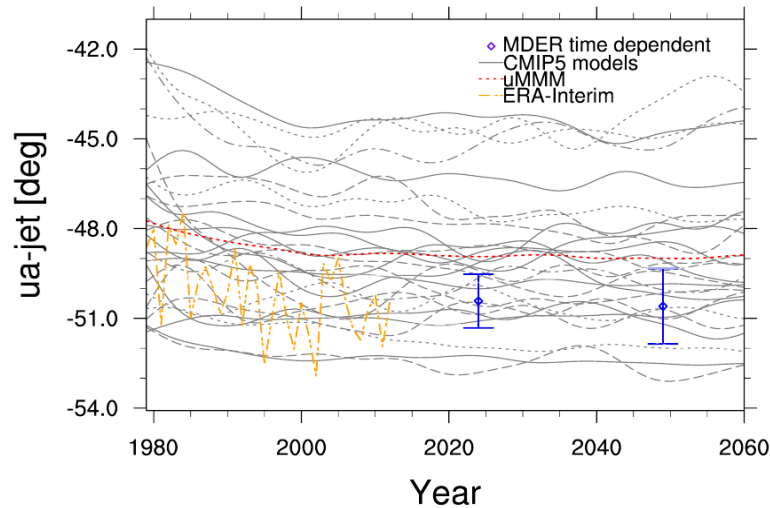
Figure 5.4: Time series of the austral jet position for the RCP4.5 scenario between 1980 and 2100. Grey lines show the individual models (iteratively smoothed with a 1-2-1 filter, repeated 30 times, to reduce the noise) and the red dotted line the unweighted model mean across all CMIP5 models in 5.2 Diamonds show the predicted mean estimate resulting from the MDER analysis, for the near-term (2015 - 34) and mid-term (2040 - 59) climatological means austral jet position. Error bars indicate the 95% confidence interval of the regression analysis. The orange line shows the reanalysis data from ERA-Interim.

5.3.2   Mid-term Projections of the Austral Jet Position

A key finding from the application of MDER to the near-term jet position is that the climatological biases in CMIP5 historical integrations are larger than any of the shifts predicted in the next two decades. Next the MDER algorithm is applied to mid-term (2040 - 2059) jet position where the forcing signal is larger. As will be shown, however, the mean trends in the jet remain small, likely due to the fact that stratospheric ozone loss and greenhouse gas increases tend to oppose each other in coming decades (e.g., Perlwitz et al., 2008; Son et al., 2008). Nonetheless, MDER suggest that it can gleaned more information than a simple bias correction when focusing on longer-term projections.

Figure 5.1b illustrates correlations between the process-oriented diagnostics and the mid-term austral jet projections. Even at mid-century, SH circulation biases in the historical integrations are still the most important. The top five diagnostics with the strongest correlations to mid-term austral jet positions are the same as for near-term. The importance of the remaining 15 process-oriented diagnostics has changed, although those correlation coefficients are generally not statistically significant.

Despite the similarities in the correlation structure, MDER obtains a more complex result for the mid-term projection. The method initially constructs the regression model, -1.66 +1.02 x U-Jet_c - 0.40 x T-SP_t - 0.10 x T-SP_c, involving three diagnostics: the historical austral jet positions (U-Jet_c), stratospheric south polar cap temperature trends at 100 hPa (T-SP_t) and the 100 hPa polar cap temperature climatology, T-SP_c. While the U-Jet_c term can again be interpreted as a bias correction of the austral position in the CMIP5 models, the T-SP terms indicate the diagnostics associated with the formation of the ozone in the historical period can be used to improve future projections of the jet position.

The negative sign of the T-SP_t term reflects the fact that models which experienced larger stratospheric cooling over the historical period tend to exhibit a more equatorward shift of the jet in the future. Wilcox et al. (2012) and Gerber & Son (2014) found that models with more cooling over the polar cap tend to experience a more poleward shift in the jet, suggesting

that the jet is responding to the equator-to-pole temperature gradient in the upper tropo-sphere/lower stratosphere. Here, the relationship has changed sign because cooling over the historical period is compared to an equatorward shift in the future. Models which experienced a strong thermodynamic response to ozone loss in the past are likely to have an equal and opposite response to ozone recovery in the future, i.e. more warming, and so a more equatorward jet shift. T-SP_t can thus be acting as a proxy for the strength of ozone loss and recovery, a key driver of austral jet shifts. It is emphasized, however, that it is the temperature response to ozone loss which appears to be crucial. The regression model picks T-SP_t over the actual historic trend in ozone, O3-SP_t, even though both statistics are nearly equally correlated with future jet position. Many models used a similar ozone data (Cionni et al., 2011), but do not exhibit a uniform thermal response due to differences in their radiation schemes.

However, negative sign of the correlation with T-SP_c could reflect a similar connection to the ozone hole, as ozone depletion already occurred over the entire historical period (1979 - 2005): a colder historical climatology is indicative of a larger ozone hole. It is thus unclear how the climatology would contain information independent from the polar cap temperature trend, which raises the danger that MDER could be overfitting the diagnostics. In order to avoid inclusion of redundant information with unclear physical interpretation, the regression model was therefore recalculated, intentionally removing the T-SP_c diagnostic, and obtained the result: -1.41 + 0.99 x U-Jet_c - 0.36 x T-SP_t. The difference between the projections made by these two models is 0.2°, much smaller than the uncertainty of either statistical model (see below). Based on further cross-validation tests (not shown), the simple model can be expected to be more robust and so it was applied in Figure 5.2b. It incorporates two physically justified constraints: a correction for biases in the climatological jet position and a correction based on the intensity of thermodynamic response to stratospheric ozone loss.

Figure 5.3 shows also the cross validation tests for the mid-range jet projection. As one might expect the RMSE$_{MDER}$ prediction error (0.59 deg) is larger for the mid-21st century case than for the near-term analysis (where it was 0.42 deg), but still more than four times less than the uMMM prediction error (RMSE$_{uMMM}$ = 2.47 deg). Again, the key is that the shifts in the jet stream, even 50 years away, are small relative to the biases in the models historical climatology. As noted in the discussion of Section 5.3.1, the RMSE errors reflect the uncertainty in light of 28 realizations of the future, and do not account for uncertainty in jet associated with a single realization, as will be the case with our one Earth.

From the regression model in Figure 5.2b, the MDER analysis predicts an austral jet stream position for the mid-term climatological mean of 50.6°S, implying a mean shift of 0.2° southward compared to the 2015 - 2034 position of the austral jet (or 0.6° southward from its historical climatology). The uMMM projection, 50.0°S, suggests a small southward shift from the 2015 - 2034 mean as well (Figure 5.4), but only by 0.1°. Note that this is still northward of the jet location in historical reanalysis: naively comparing the future projection with historical reanalysis would give one the opposite trend.

In the near-term application, MDER took the shift in the uMMM projection and bias corrected for the mean jet location. With inclusion of information on stratospheric polar cap temperature trends, MDER modifies the jet trend as well. However, this modification (and the total trends themselves) is very small relative to the 1.5° bias in the models historical jet position climatology. The trends are also small relative to uncertainty in the jet position associated with natural variability; given 1979 - 2005 reanalysis data, it can only be said that the mean jet position was between 50.0 ± 0.5°S with 95% confidence.

5.4   Summary and Discussion on the SH Jet Position

In this study that was published in Wenzel et al. (2016), a multiple diagnostic ensemble regression (MDER) algorithm scenario was used to analyze the austral jet position in projections of the 21st century under the RCP 4.5, a moderate carbon future. MDER allowed to incorporate 20 process-oriented constraints from observations and reanalysis to improve upon the uMMM projection. The method can be interpreted as a re-weighting of models based on biases in their historical climatologies (Karpechko et al., 2013).

First the MDER method was applied to the near-term climatological mean (2015 - 2034) of the austral jet position. The method removed the equatorward bias in the jet stream, suggesting that the best estimate of its future position should be 1.5° southward of that found in the uMMM projection (48.9°S). Second it was focused on a mid-century austral jet stream projection, a target period of 2040 - 2059. In addition to the same need to correct for the climatological jet position bias, MDER found that lower stratospheric polar cap temperature trends over the historical period could be used to effectively discriminate future trends. From a physical standpoint, historical temperature trends are an indicator of the intensity of the ozone hole. It is likely that models with more intense cooling over the historical period of ozone loss will experience more intense warming as ozone recovery, and hence a more equatorward shift in the jet stream as it responds to changes in the upper troposphere/lower stratosphere temperature gradient.

Expected shifts in the jet stream in coming decades are generally small, on the order of 1/10ths of a degree, in part due to cancellation between the impacts of stratospheric ozone recovery and increased greenhouse gas loading (e.g., Perlwitz et al., 2008). Biases in some models climatological jet position, on the other hand, are on the order of degrees, and the multimodel mean position is 1.5 degrees poleward of that found in ERA-Interim reanalysis. Thus, a naive use of the uMMM to project the mean jet position in the near or mid-term places the future jet equatorward of its current position, even though most models project that it should shift slightly poleward over this period. While this bias correction is a fairly straightforward result, it is the first effort to account for this bias in future projections.

Getting the jet in the right place has significant implications. First, it is co-located with the storm track, and so tightly linked with the boundary between the subtropical dry zone and extratropical precipitation maximum. Shifts in the jet have significant impacts on regional precipitation (e.g., Kang et al., 2011; Thompson et al., 2011) and it is critical that regional modeling efforts to downscale climate information from global models account for this bias. Second, the surface wind stress associated with the jet stream plays a key role in the overturning circulation of the ocean (Waugh et al., 2013). Biases in the austral jet position limit our ability to accurately model the heat and carbon uptake of the deep ocean (Swart & Fyfe, 2012).

Given these large model biases, an alternative approach would be to first compute the jet shift from the historical period to the future using the models, and then to simply add this to the historical climatology based on reanalyses (e.g., Räisänen, 2007). MDER effectively led to this result for the near-term projection. This change based approach, however, relies on the explicit assumption that biases in simulated present-day and future climates remain constant (i.e., that the jet shift only depends on the applied forcing and is independent on present jet positions). MDER does not make this assumption, and it did make a difference (albeit a small one) for the mid-term projection.

The regression model for the mid-range jet projection suggests that the historical trend in polar stratospheric temperatures can be used to better estimate the future jet position. Constraining this trend with reanalysis, however, is problematic, as changes in the observational network can lead to spurious trends. Calvo et al. (2012) suggest that Antarctic lower stratospheric cooling due to ozone depletion (T-SP_t) may be underestimated by ERA-Interim by as
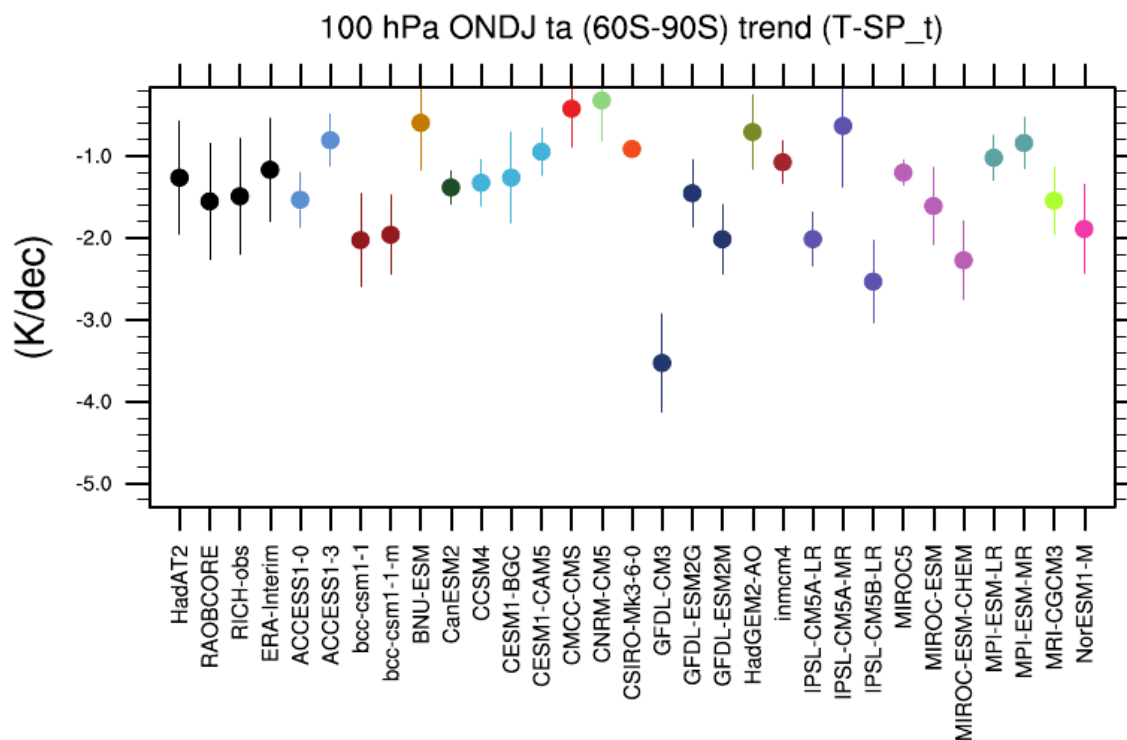
Figure 5.5: Trends in October-November-December-January (ONDJ) temperature anomalies (ta) at 100 hPa over Antarctica for radiosondes data (HadAT2; RAOBCORE; RICH-obs), the ERA-Interim reanalysis and the individual models of the CMIP5 ensemble. Vertical lines indicate the sample standard deviation of the mean value.

much as a factor of 2 compared to radiosonde observations. On the other hand, the interannual variability of the temperatures is so large that the discrepancy between trend estimates based on ERA-Interim and radiosondes is within statistical uncertainty (Calvo et al., 2012).

To test this, Figure 5.5 compares the T-SP$_t$ $diagnostics derived from the CMIP5 models with ERA-Interim data and the radiosonde observations that were analyzed by Younget al. (2013): HadAT2(Hadley$ $obs(Radiosonde Innovation Composite Homogenization(obs), ver.1.5, Haimberger et al. (2012)). For the $ $2005) considered in our study, the mean trend in ERA-Interim is approximately -1.4K/dec, and so slightly$ $1.6 and -2.2K/dec, The ERA-Interim trend, however, is still mostly within the given observational uncer$ $Interim climatology (Figure 5.5) is found to be very similar to the radiosonde climatology.$

The focus of MDER on different time periods provides additional insight into which physical processes are important for projections at the mid-term horizon. In the near term, diagnostics focused on biases in the climatology are most important. At mid-century, uncertainty associated with stratospheric ozone trends also becomes important. Towards the end of the century, when the ozone hole is mostly recovered, uncertainty in tropical warming trends begin to appear in the MDER results (not shown). The tropical warming trends over the historic period give an indication of how sensitive a model is to greenhouse gas warming: models that warm more over the historic period tend to warm more in the future, and so project greater circulation trends. Due to the lack of reliable direct measurements of upper troposphere temperature trends, the results, however, are not presented here. The study thus emphasizes the need for reliable long term climate records, which may prove critical for constraining future model projections.

Chapter 6

Summary, Conclusions and Outlook

6.1 Summary

While evaluation of climate models with observations can be used to build confidence in model fidelity, this does not guarantee the correct response to changed forcings in the future. In the relatively new field of emergent constraints, an apparent relationship between simulated climate sensitivity to anthropogenic forcings and observable features of the Earth's climate system is being used. Within this thesis the uncertainty of biogeochemical and climate feedbacks was investigated for three specific applications: the carbon cycle-climate feedback (Wenzel et al., 2014), the carbon cycle-CO_2 concentration feedback (Wenzel et al., 2015), and the future shift in the Austral Jet Stream (Wenzel et al., 2016).

The first study of this thesis was published in Wenzel et al. (2014) and focuses on the response of the carbon cycle to climate warming. From model simulations it is expected, that future climate change reduces the strength of the terrestrial carbon sink. Warming leads to an increase in soil respiration and therefore a net carbon loss. In a scenario with 1% per year increase in carbon dioxide (CO_2) concentration, CMIP5 ESMs simulate a wide spread in tropical land carbon storage at the time of the quadrupling of atmospheric CO_2, in the order of 252 $\pm$ 112 GtC when carbon climate feedbacks are enabled. Consequently, the spread in the long-term sensitivity of land carbon storage to future climate change (i.e., carbon cycle-climate feedback, γ_{LT}) is large, being in the order of -49 $\pm$ 40 GtC K-1 for the multi model mean. Thus the carbon cycle-climate feedback remains one of the key uncertainties in current ESM projections. A tight correlation in CMIP5 ESMs was found between γ_{LT} and the short-term sensitivity of atmospheric CO_2 to interannual variability in tropical temperature (γ_{IAV}), enabling the carbon cycle-climate feedback to be constrained with an observable quantity. Especially in the tropics the interannual temperature variations between warmer and colder years, caused by the ENSO variability drives the change of CO_2 growth rate, hence having the same physical driver as the long-term sensitivity. This relationship was previously identified by Cox et al. (2013). However, in the study presented in this work the CO_2 growth rate was diagnosed from land and ocean carbon fluxes, rather than directly from atmospheric CO_2 as done by Cox et al. (2013). From this slightly different analysis the observed γ_{IAV} is diagnosed to be -4.9 $\pm$ 0.9 GtC y-1 K-1, which was used to constrain the carbon cycle-climate feedback γ_{LT} to -44 $\pm$ 14 GtC K-1 in the CMIP5 ensemble. Hence a temperature increase of 1 Kelvin reduces the tropical land carbon store by approx. 44 Gt of carbon, constituting a positive feedback to climate by releasing more CO_2 to the atmosphere where it can act as a GHG. When repeating the analysis with C^{4}MIP models, which were used by Cox et al. (2013), this new estimate of the tropical land carbon sink, strongly overlaps with the analysis using CMIP5 models proving the robustness of this relation. Within this work also a mathematical formulation for this particular emergent constraint has been started to be developed, describing the physical connection between the long- and short-term sensitivity of the carbon cycle to climate change.

The second study that is under review (Wenzel et al., 2015) focuses on the carbon cycle response to elevated atmospheric CO_2 concentrations that are projected for the end of the 21st century. Coupled climate-carbon-cycle models generally agree that the uptake of carbon by plants increases with increasing CO_2 concentration, but the magnitude of the sensitivity

remains a key uncertainty among the models. Observed changes in the seasonal cycle of CO_2 are used to constrain the long-term land carbon sensitivity to atmospheric CO_2 increase in an ensemble of ESMs participating in CMIP5. For a doubling of CO_2, the models simulate a wide spread in high latitude Gross Primary Productivity (GPP) in the order of 7.5 ± 7 GtC when climate-carbon cycle feedbacks are enabled. This also leads to a large uncertainty range of 18 - 62% in CO_2 fertilization of future high latitude GPP across the models for a doubling of atmospheric CO_2 concentrations. Combining the diagnosed high latitude GPP increase with trends in the CO_2 seasonal cycle amplitude a tight correlation between long-term sensitivity and short-term trends exists. The growth of the CO_2 seasonal cycle amplitude at Point Barrow, Alaska, is indicative of the fertilization effect of GPP, as it mirrors the net uptake of carbon via increased photosynthesis throughout the year. The observed CO_2 amplitude trend is in the order of 0.06 ± 0.011 ppmv/ppmv and constrains high latitude GPP at the stage of doubling CO_2 concentrations to 39 ± 9%. The presented high latitude constraint on GPP projections is largely free from agriculture influences and therefore presents a clean relation between observable trends and future Earth system sensitivity. The results therefore imply an increased carbon uptake into the high latitudes terrestrial carbon store by about 0.14% per ppmv atmospheric CO_2 increase, constituting a negative feedback to climate by storing more carbon in the terrestrial carbon sink due to elevated atmospheric CO_2. This relation was also tested for a low-latitude measuring site at Mauna Loa, Hawaii, but the CO_2 seasonal cycle at Mauna Loa is also influenced by agriculture and climate variability. To remove the impact of climate variability from the CO_2 seasonal cycle amplitude in order to separate the sole CO_2-effect, a good correlation between the CO_2 seasonal cycle amplitude at Mauna Loa and the first principal component of sea surface temperature in the Atlantic region was used which is known as the Northern Atlantic Oscillation (NAO). Using multiple linear regressions the influence of increasing annual mean CO_2 on the CO_2 seasonal cycle amplitude can be obtained and separated from the influence of the climate variability. This diagnosed CO_2effect helps to constrain the carbon cycle-CO_2 feedback with observations, and is well within the range of the constrained high latitude GPP increase. For a doubling of atmospheric CO_2, the study estimates a 39 ± 9% and 34 ± 10% increase in GPP for high latitude ecosystems and extra-tropics ecosystems, respectively. The results therefore imply an increased carbon uptake into the terrestrial carbon storage by about 0.12% per ppmv CO_2 increase for the extra tropics and 0.14% per ppmv for the high latitudes.

In a third study, a process-oriented Multiple Diagnostic Ensemble Regression (MDER) method was applied to constrain projections of the summer austral jet position. The results from this study were published in Wenzel et al. (2015). MDER is a statistical technique in which prior distributions of model simulations of present-day climatological variables and trends are related to posterior predictive distributions of climate variables in a multiple linear regression. The MDER method has been developed by Karpechko et al. (2013), who constrained future October Antarctic total column ozone projections. This method was now applied to a new scientific question, where the future southern hemispheric jet position is predicted by the model spread of relevant process oriented present-day diagnostics. While stratospheric ozone depletion in the Antarctic polar region in combination with increasing GHGs led to a cooling of the lower stratosphere and upper troposphere in the late 20th century, which strengthened the Austral jet, ozone recovery will now have an opposite effect. Previous studies have shown that ozone recovery might reverse or offset the impact of GHGs on the southern hemispheric jet position. The exact balance between the impact of ozone recovery and increasing GHGs and the effect on the Austral jet position remains a key uncertainty. Observations and process oriented present-day diagnostics of processes that are known to have an impact on the Austral Jet Stream are included in the MDER method to constrain future Austral jet position trends. The position of the westerly jet is calculated from a medium (RCP4.5) GHG scenario, where models simulate a wide spread of 10° of the jet position. The application of the MDER method

to a near term period (2015 - 2034) shows a bias correction compared with the unweighted CMIP5 ensemble mean and moves the weighted mean 1.5° poleward, i.e. a better agreement with observed Austral jet positions. For a mid-term application of the MDER method on the summer austral jet position, an additional correction of the model mean bias was found. While on the near-term time period the CMIP5 ensemble mean bias is larger than any trend, on the mid-term time period also uncertainties in the summer austral jet shift become important. The regression model, generated by the MDER algorithm includes a correction term which implies jet position to be especially sensitive to ozone recovery associated with Antarctic lower stratospheric warming. Also the cross validation in "pseudo reality", where each model in turn represents "pseudo observations", shows an improvement in all cases of the MDER results. The focus of the MDER method on different time periods provides additional insight on the importance of physical processes that might change as the climate forcings evolves.

6.2   Overall Conclusions

The thesis also provided answers to the specific questions posed in Section 1.2:

Q1: How well are selected biogeochemical processes represented in state-of-the-art ESMs that determine the long-term behavior of climate?

- In all three studies, current ESMs from the CMIP5 ensemble simulated a wide range of future projections of the targeted variable (i.e., carbon cycle-climate feedback, carbon cycle-CO_2 feedback, and austral jet position) leading to large uncertainties in corresponding future projections. For the carbon cycle, CMIP5 models simulate a large spread in tropical Net Biosphere Productivity (NBP) and in high latitude GPP. In addition differences in simulated tropical temperature and atmospheric CO_2 concentrations contribute to the large spread for carbon cycle feedbacks. The results suggest that models overestimate the magnitude of the terrestrial carbon sink. For the third study 20 different processes that are known to impact the SH jet stream position were evaluated against observations. Results show that especially the processes that are linked to dynamical biases in the models show a large spread and fall outside the range of observations. Additional work is required for a full assessment of the representation of biogeochemical processes in ESMs, but this thesis gives guidance on a number of processes that are relevant for future projections.

- Not all ESMs with interactive carbon cycle used in the first two studies also include nutrient limitation processes. Nitrogen limitation leads to a reduction of the land carbon uptake. Models that account for nitrogen limitations therefore simulate a larger atmospheric CO_2 growth and climate change than in equivalent models neglecting this process. The nitrogen cycle is one of the reasons for the large spread in the CMIP5 ensemble, as only a few models included it. Improving or including limitation of CO_2 fertilization in ESMs is recommended for model development. Other important processes that differ substantially in ESMs are decomposition of soil organic matter and photosynthesis, where uncertainties increase the model spread.

- In the third study, ESMs showed large uncertainties in southern hemispheric dynamics, leading to biases in the austral jet position. Biases in the current SH jet position arise from climate and circulation sensitivities in response to temperature perturbation. Correcting these biases in ESMs is crucial, since a wrong position in SH jet streams implies incorrect projections of precipitation, storm tracks, ocean carbon and heat uptake and hence other biogeochemical cycles. On the longer term also climate forcings are important for the future jet position, such as stratospheric

ozone recovery and increase in GHGs. But not all models calculated atmospheric chemistry interactively. Prescribed atmospheric chemical concentrations does not decrease the model spread per se, but could eventually lead to an underestimation of the actual uncertainty.

Q2: How can observations be possibly used to narrow the range of plausible climate projections by providing quantitative observationally-based constraints?

- The Climate Response Uncertainty of models can be reduced with observations by using the emergent constraint approach.

- The application of the emergent constraint methods as done in the first two studies on the carbon cycle helps to better understand the sensitivity of the Earth system to climate change. Here, an observable variation (i.e., the interannual variability of the CO_2 growth rate) or trend (i.e., the trend in the CO_2 seasonal cycle amplitude) constrains future carbon cycle feedbacks.

- The MDER approach helps to better understand the underlying processes that force future climate projections (i.e., the austral jet position). In this approach observable process-oriented diagnostics are combined in linear regression to predict future projections of climate variables. But not all diagnostics that are known to influence the projection of the austral jet position will be included in the regression model of observed diagnostics, thus providing additional insight to the most important underlying processes for model evaluation.

Q3: What are the strengths of selected biogeochemical climate feedbacks?

- Narrowing the uncertainty range of carbon cycle feedbacks provides the basis for an improved estimate of the strength of the terrestrial carbon sink as well as a better understanding of the balance between positive and negative carbon cycle feedbacks. For the carbon cycle-climate feedback a response of -44 ± 14 GtC per 1K warming was estimated, reducing the previous model mean uncertainty by half.

- For the carbon cycle-CO_2 feedback a CO_2 fertilization of GPP by about 14% per ppmv for high latitude ecosystems and 12% per ppmv for extra tropical ecosystems was estimated, significantly reducing the previously published model uncertainty. This has important implications for future climate targets, as a reduced uncertainty of the terrestrial carbon sink efficiency also reduces the range of the allowable anthropogenic CO_2 emissions to reach e.g., the 2°C warming target. By reducing the uncertainty in the CO_2 fertilization of GPP the study suggests a lower allowable amount of cumulated anthropogenic CO_2 to be emitted to still be able to reach this target.

- The analysis on the austral jet position effectively reduces the multi-model mean equatorward bias in CMIP5 models. By applying the MDER algorithm on two different time horizons for near-term (2015 - 2034) and mid-term (2040 - 2059) the model mean position of the SH jet stream was corrected to be 1.5° more poleward compared to the unweighted CMIP5 ensemble.

6.3　Outlook

Several promising emergent constraint studies have been published on individual key feedbacks, including the three studies that have been performed as part of this thesis. Emergent constraint analysis can help focusing model development and evaluation onto processes that are crucial for the magnitude and spread of future Earth system changes and remain a promising approach.

Nevertheless some issues have been identified. One example is the interdependence of climate models in multimodel ensembles. Some models share common code or parametrizations as discussed in Chapters 3 and 4. In these two studies on the carbon cycle, two models include the same land model and therefore share the same biases, thus effectively reducing the ensemble size. To tackle this problem, methods need to be developed that consider the dependence of models on an objective basis. The presented emergent constraints should in general also hold for other ensembles of models. Testing the emergent constraints on the next generation of models (e.g., CMIP6) will therefore be essential to further demonstrate robustness and to examine possible scenario dependence.

Another problem is that often spurious correlations between the Earth system sensitivity and an observable feature of the current climate are used as an observational-based emergent constraint. This can be avoided by finding an observable physical explanation to constrain the unobservable Earth system sensitivity as it has been done in the three studies presented in this thesis. The risk in ensemble regression methods that correlate present-day diagnostics or variables to a future climate variable by a statistical significance test is particularly high, since the resulting correlations might only be a statistical artifact rather than a relation based on a convincing physical explanation. To prevent such ensemble regression methods from including too many present-day diagnostics into the regression model, a stopping criterion is used. However, this criterion is subjectively chosen and needs to be questioned for every study. Therefore cross-validation methods as applied here in the study on the austral jet position are crucial and needed to identify such spurious correlations, by comparing the RMSE of the multimodel mean to the constrained quantity.

Emergent constraints mostly rely on correlations between an Earth system sensitivity that is driven by the same process as the variation in the observable quantity. However, these relations mostly preclude abrupt changes of the climate system (i.e., tipping points) because they are not simulated by current climate models. Existing emergent constraints could be tested by comparing the results to perturbed model simulations including tipping elements, such as tropical and boreal forest dieback and permafrost loss in the Tundra and the Arctic oceans.

Many emergent constraint studies also suffer from the lack of robust observations with long enough records to demonstrate a statistically significant observational constraint, where the observed uncertainty is significantly smaller than the ensemble size. Furthermore, in all three studies performed in this thesis, only the observational uncertainties from interannual variability were taken into account. To provide robust observational constraints of Earth system sensitivities and future climate projections, long-term observational records are needed with quantified uncertainties (e.g., measurement error). Especially the third study, presented in Chapter 5, had to rely on reanalysis data, where changes in the observational network could lead to spurious trends, thus leading to an underestimation of the diagnosed present-day trends.

To identify additional emergent constraints on individual feedbacks a careful examination of the underlying physical process is inevitable. If the physical process is known, adequate observations are needed to investigate the same physical process in the current climate. To constrain the overall sensitivity (e.g., ECS, TCR, TCRE) multiple studies of emergent constraints could help to obtain a robust constraint, since these sensitivities depend on multiple physical processes. In addition, theoretical insights on emergent constraints should be further studied that link the sensitivity of climate to external forcing to its internal variability in the spirit of the Fluctuation-Dissipation Theorem.

Emergent constraints are helpful to identify important processes that could reduce the model spread on climate projections for example by improving included parametrizations. Models will also incorporate additional processes so that the model will provide a much more detailed picture of climate change. From such model improvements it is hoped that uncertainties in

climate projections will be reduced. On the other hand other model biases may then govern the spread in emergent constraint.

More specifically, from the constrained carbon cycle feedback studies presented in Chapters 3 and 4 the magnitude of the terrestrial carbon sink in the real world potentially can be inferred. Knowing the terrestrial carbon sink enables future projections of atmospheric CO_2 concentrations to be constrained with observations. However, both presented carbon cycle feedbacks were diagnosed for particular but different regions, where physical mechanisms of the short-term responses are the same as for the long-term response and also observations were available. Constraining these carbon cycle feedbacks for other regions and in particular the global domain remains an open issue and needs further extensive research. For example constraining the carbon cycle-climate feedback in the extra tropics or globally could be difficult since the year to year temperature variations are not as well pronounced as in the tropics. Additionally, other factors, such as dynamical influences, agriculture and land use change may impact the relation between short and long-term sensitivity and might as well influence the observable signal of atmospheric CO_2. The CO_2 fertilization of future GPP increase was constrained in Chapter 4 by using measurements from only two different measuring sites. Extending this study with additional observations from other measuring sites would require further research on the mechanisms that influence the variability of the CO_2 seasonal cycle amplitude. This makes it difficult to effectively constrain the magnitude of terrestrial carbon sink and remains a pressing problem. To assess robustness on the presented emergent constraints on carbon cycle feedbacks in this work, the studies could be repeated using different observations from for instance, the ESA Climate Change Initiative (CCI), creating long-term, homogenized data set of satellite data. Satellite data, once the record is long enough, opens new possibilities for emergent constraint studies in the future.

Extending the analysis on the SH jet position topic in Chapter 5, the impacts of different GHG emission scenarios and their long-term influence on shifts in the SH jet stream together with associated climate impacts could be examined. The MDER algorithm could then be applied to multiple time periods to analyze the impact of changing GHG and ozone forcings on the SH jet shift. The relative importance of observed process-oriented diagnostics for constraints on future austral jet position is expected to change towards the end of the 21st-century, but also by using different RCP scenarios. Constraining the shift in the SH jet stream position enables further evaluation of regional impacts of this shift.

Emergent constraints of the type as presented in this thesis, between observable aspect of the current climate and long-term Earth System Sensitivities or projections of climate variables, offer a very promising approach to reduce the uncertainties in climate change projections. I hope that this work will act as some stimulus for others to search for emergent constraints among the growing ensemble of complex ESMs that are now becoming available for analysis as part of CMIP6.
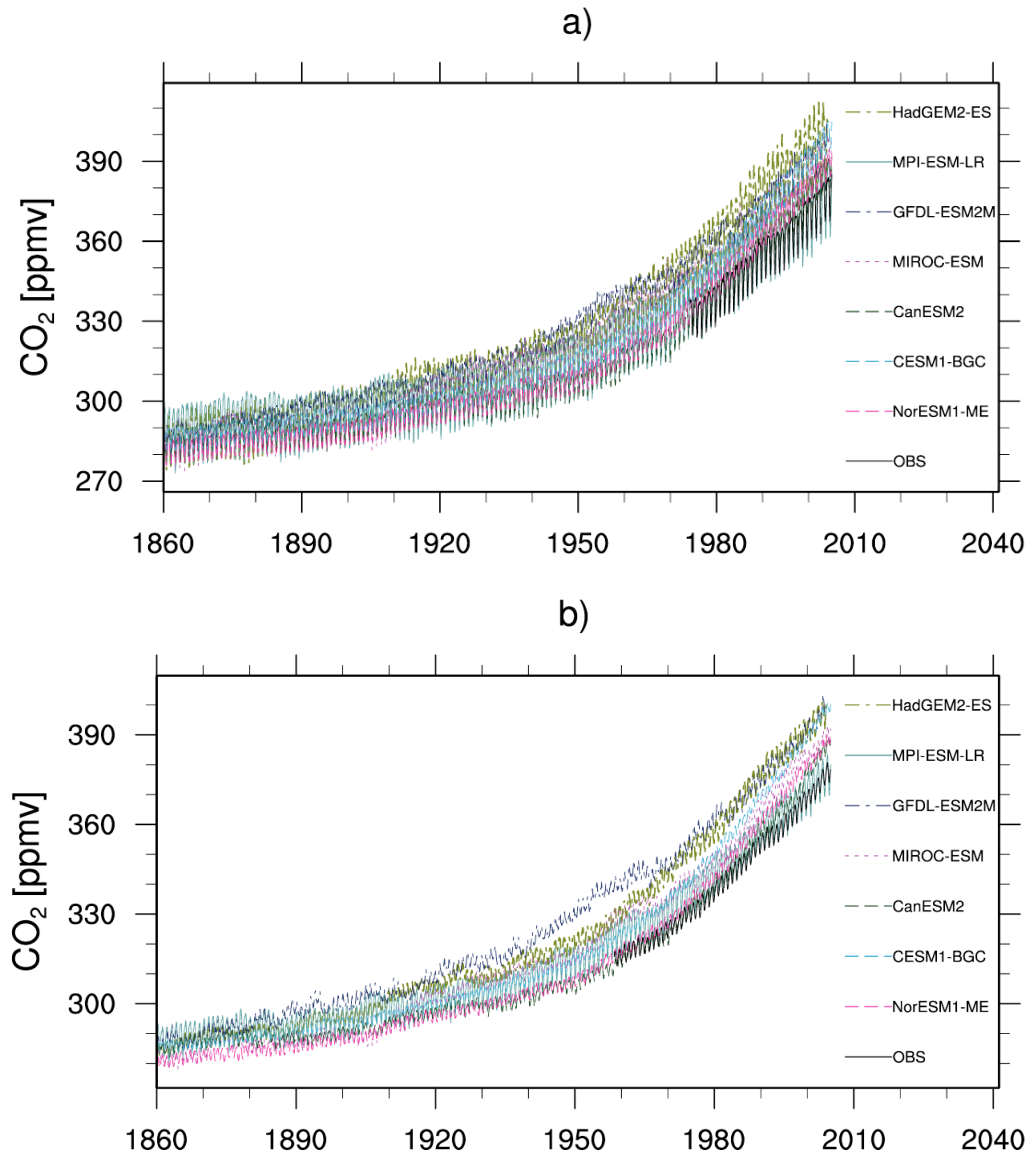
Appendix A

Figure A1: Simulated and observed CO_2 concentrations. Time series of monthly mean atmospheric CO2 between 1860 and 2005 at (a) Poit Barrow and (b) Mauna Loa at surface level, as simulated by the CMIP5 models in the historical simulations and observed (black lines) at each measuring site.
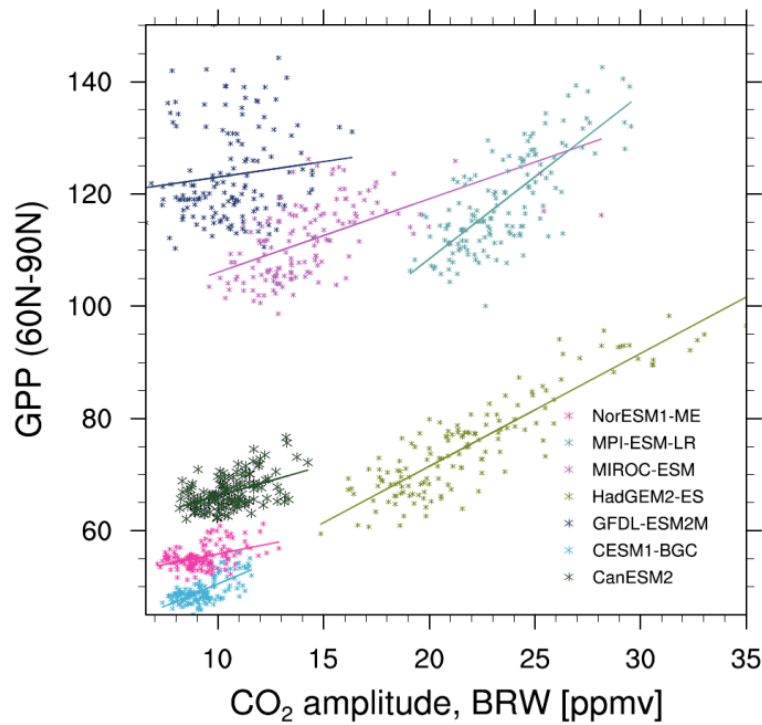
Figure A2: Annual mean high-latitude (60°N-90°N) GPP against the amplitude of the CO_2 seasonal cycle at Point Barrow, for each of the CMIP5 ESMs. Markers show values for the individual years between 1850 and 2005 for the CMIP5 historical simulation and lines show the linear best fit for each model.
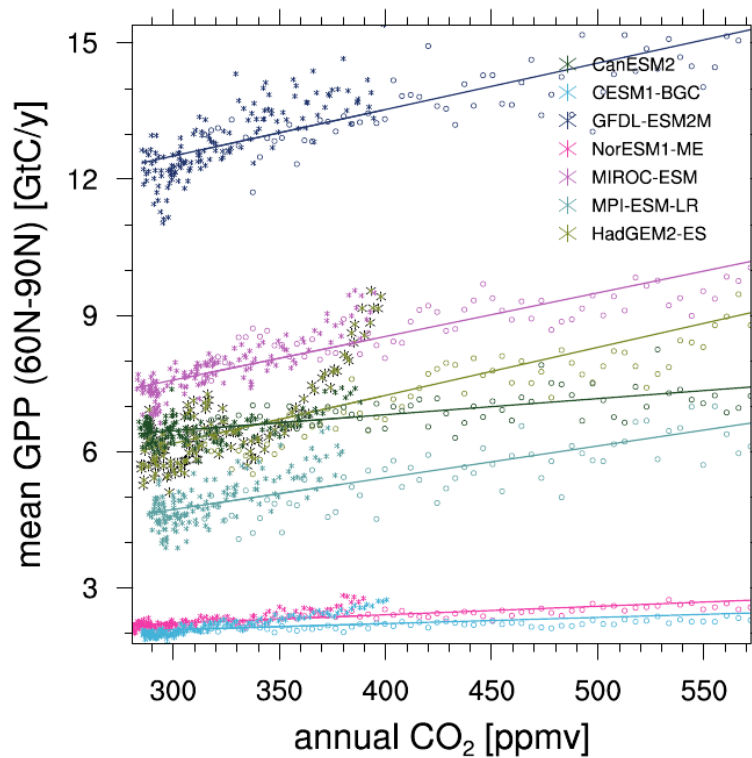
Figure A3: High latitude (60°N-90°N) GPP versus annual mean CO_2 for both the historical (circles) and the 1%BGC (asterisks) CMIP5 model simulations. Markers in show the values for the individual years and lines show the linear best fit for each model.
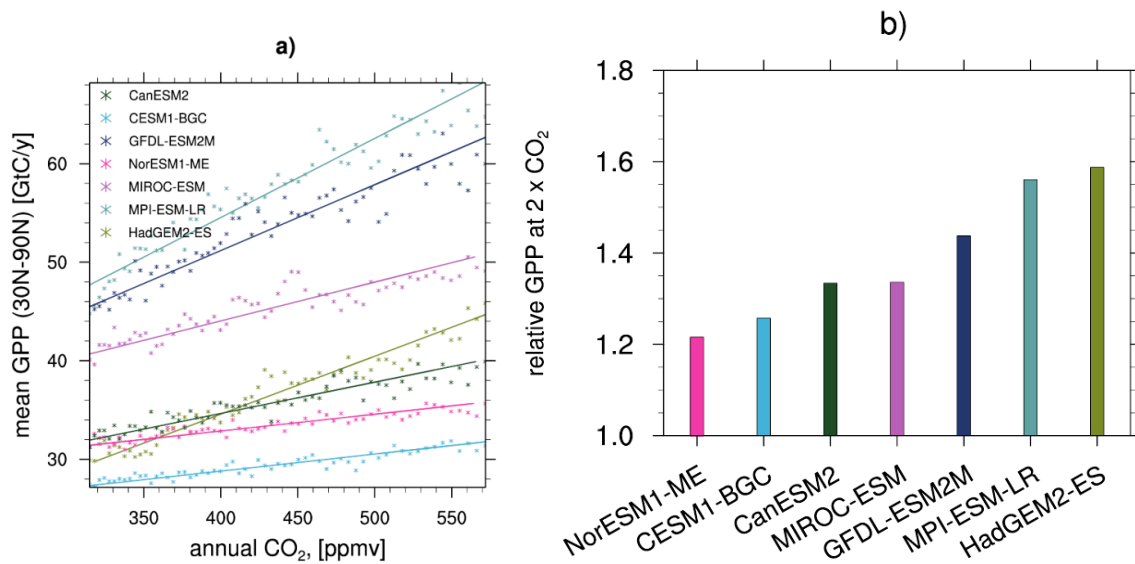
Figure A4: Comparison of simulated extra tropical GPP at a doubling of CO_2 in the 1%BGC simulations. (a) Correlations between the prescribed (1% per year) CO_2 increase and annual mean extratropical (30°N-90°N) GPP. Markers show values for the individual years and lines show the linear best fit for each model. (b) Histogram showing the relative change in the high latitude GPP due to doubling of atmospheric CO_2 (see Methods).
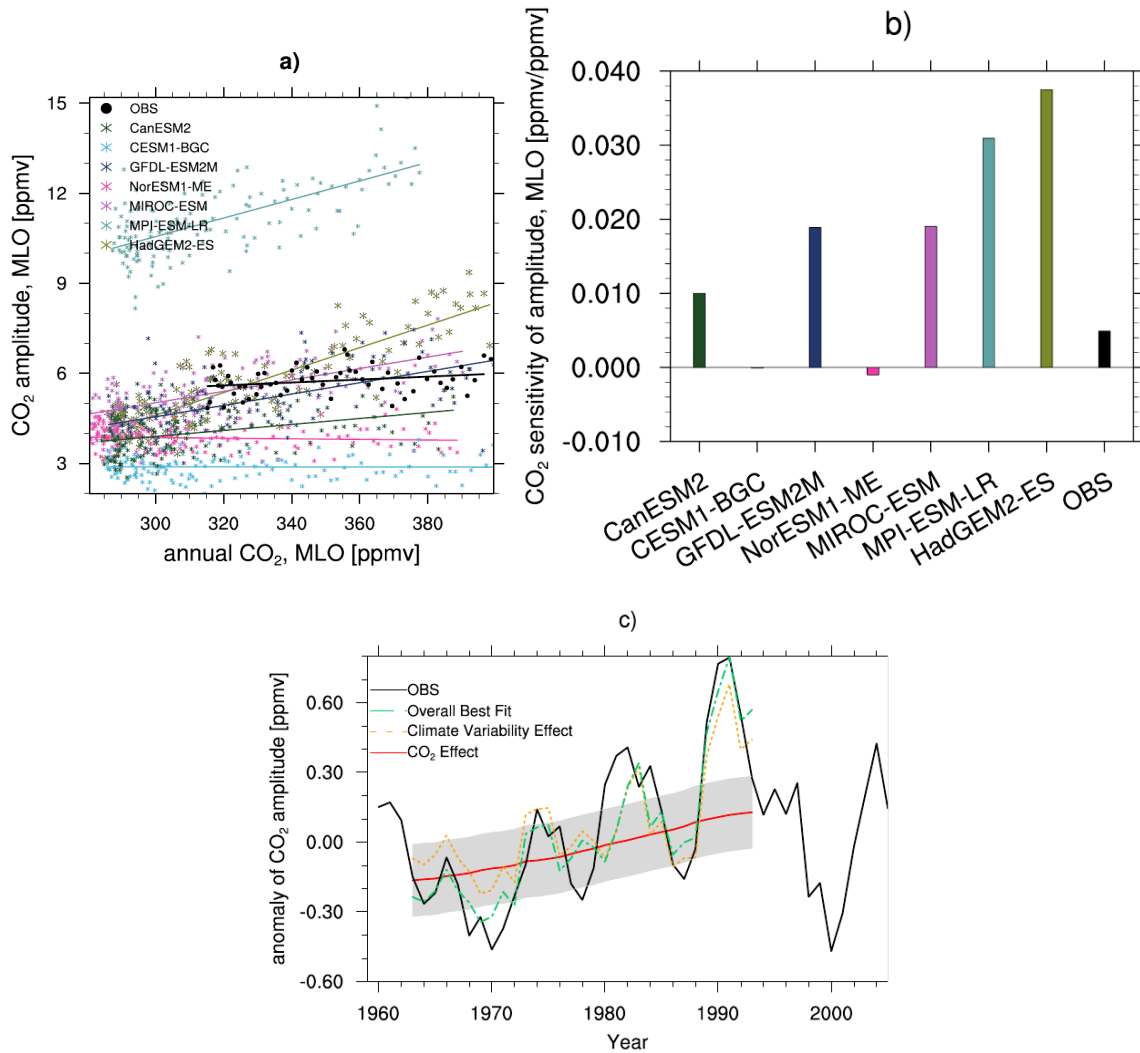
Figure A5: Comparison of observed and simulated CO_2 seasonal cycle amplitudes at MLO. (a) Amplitude of the seasonal cycle at MLO versus annual mean CO_2 for observations (black) and CMIP5 historical simulations (colours). Markers show the values for the individual years and lines show the linear best fit for each model and observations. (b) Histogram showing the gradient of the linear correlations in panel a (see Methods). (c) Comparison of the observed anomaly of the CO_2 amplitude (black), with the estimated sensitivities of the CO2 amplitude to CO_2 (red) and climate variability (orange), from the multiple linear regression. The green line shows the best-fit for the overall regression model. These regressions are performed for years with negative AMO only (see Methods). Grey shading shows the prediction error of the CO_2 sensitivity of the CO_2 amplitude.
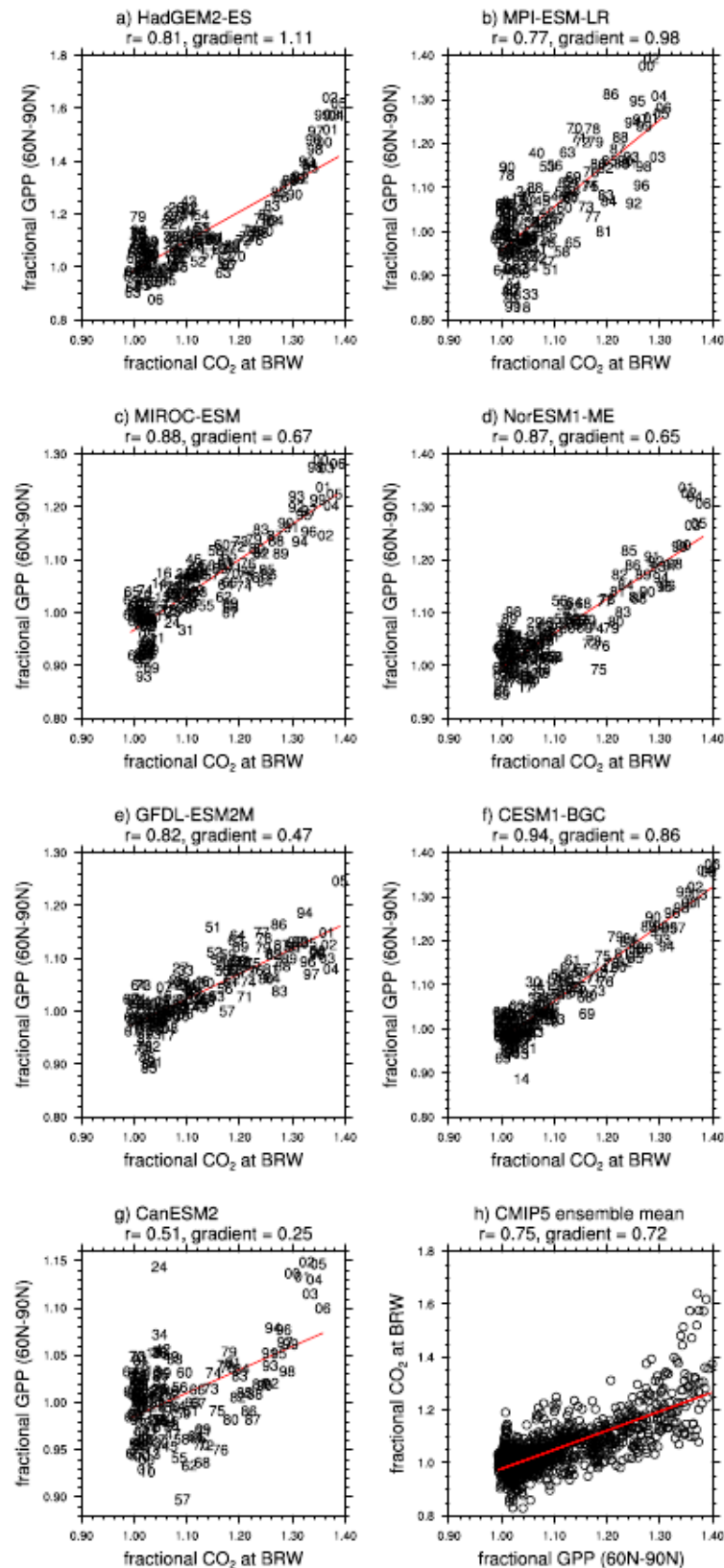
Figure A6: Correlations between fractional changes of CO_2 amplitude at Poit Barrow and mean fractional changes in high-latitude (60°N-90°N) GPP. Panels (a) to (g) show scatter plots for each model between 1850 and 2005 in the historical simulation, and panel (h) shows the ensemble mean. The correlation coefficient and the gradient for the best-fit straight-line are given in the title of each panel.
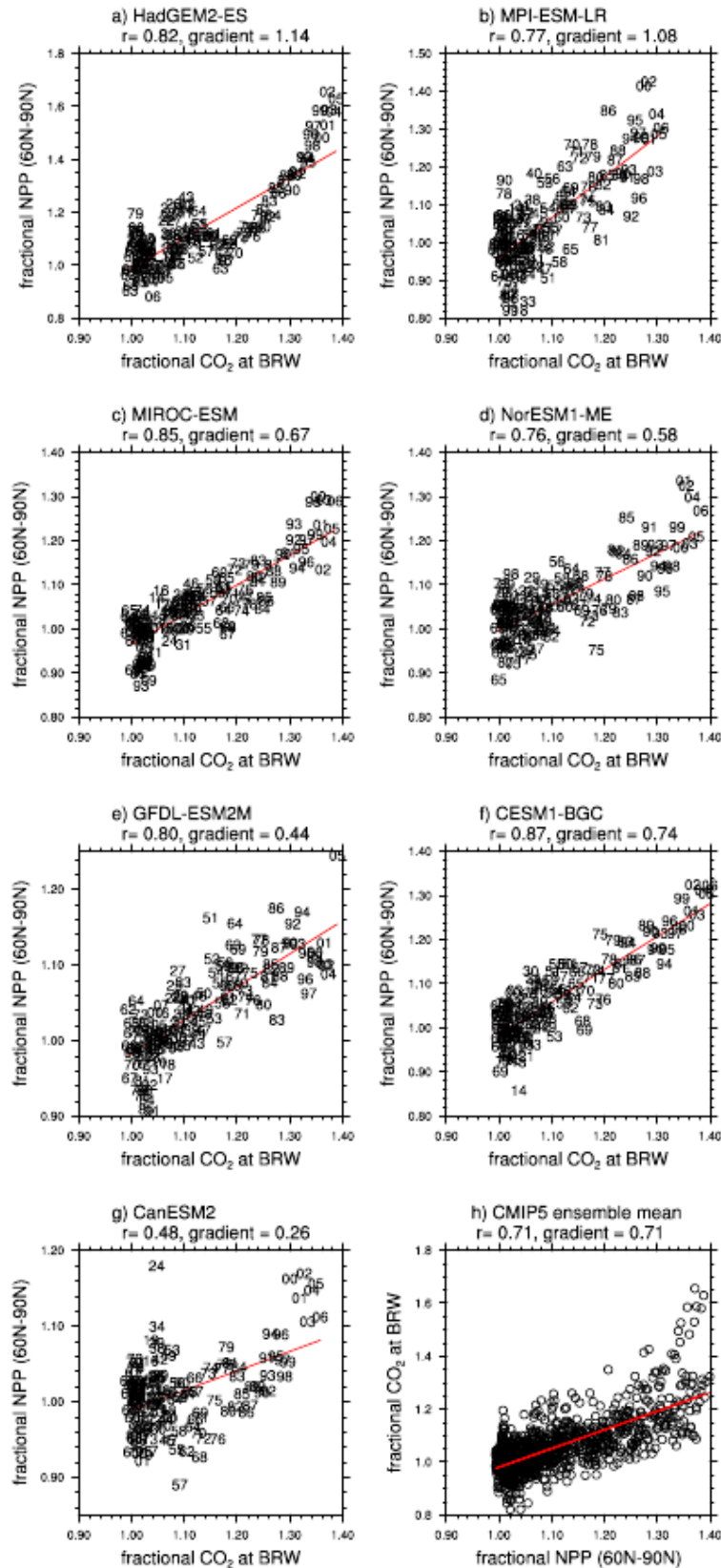
Figure A7: Correlations between fractional changes of CO_2 amplitude at Poit Barrow and mean fractional changes in high-latitude (60°N-90°N) NPP. Panels (a) to (g) show scatter plots for each model between 1850 and 2005 in the historical simulation, and panel (h) shows the ensemble mean. The correlation coefficient and the gradient for the best-fit straight-line are given in the title of each panel.
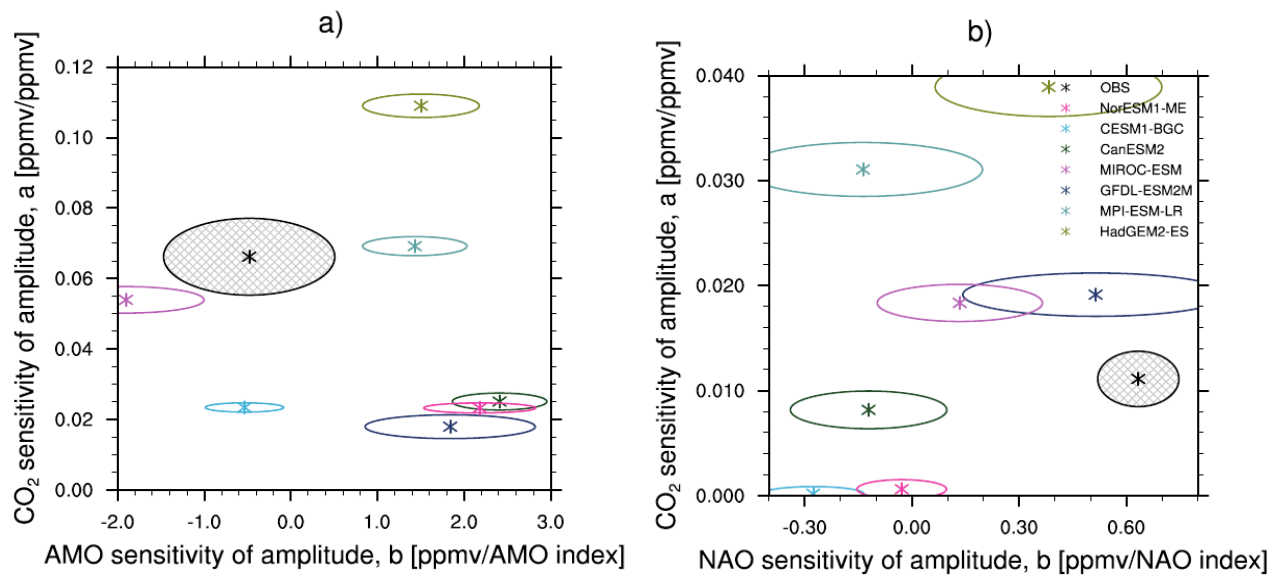
Figure A8: Regression coefficients for the sensitivity of the CO_2 amplitude to CO_2 concentration and climate index, for both models and observations (hatched ellipses). Panel (a) shows values for Point Barrow and Panel (b) shows values for Mauna Loa (see Methods). The ellipses show the uncertainty in the regression coefficients.
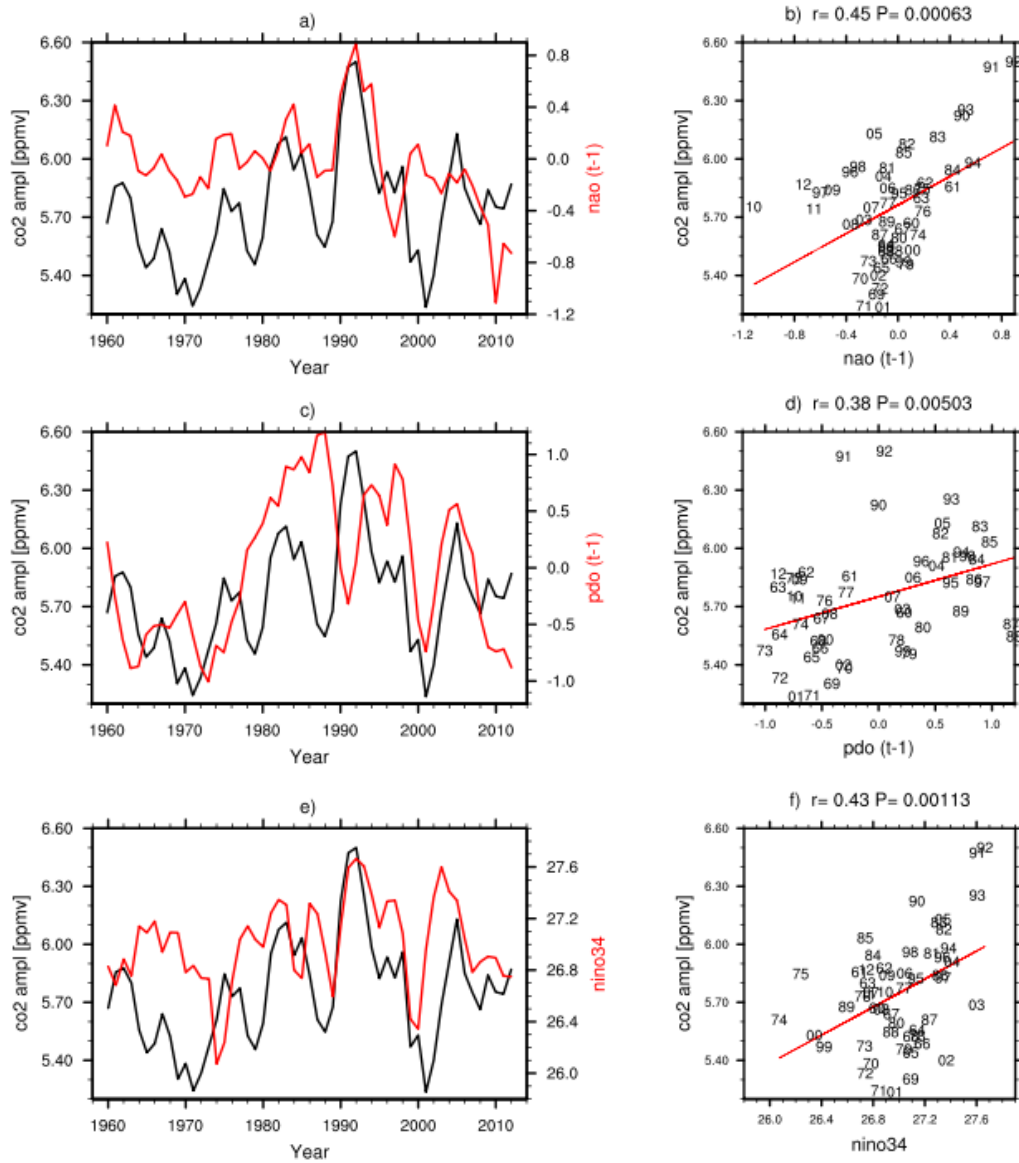
Figure A9: Comparison of observed CO_2 seasonal cycle amplitude at Mauna Loa with observed climate indices. Left panels compare the time series of the CO_2 amplitude against time series of (a) North Atlantic Oscillation (NAO), (c) Pacific Decadal Oscillation (PDO), and (e) NINO3.4. Right panels show the corresponding scatter plots for each climate index with the correlation coefficient given in the title of each panel.
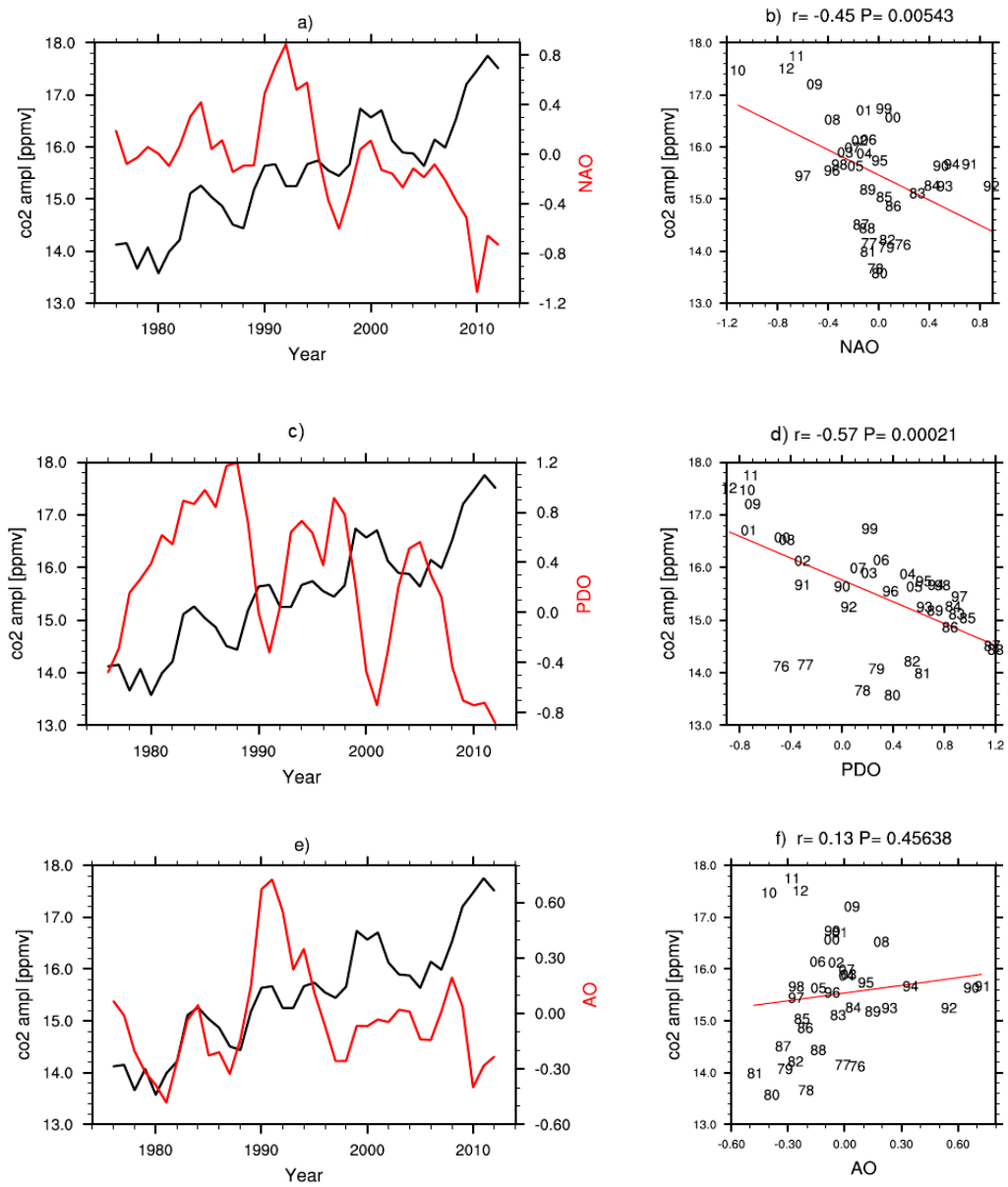
Figure A10: Comparison of observed CO_2 seasonal cycle amplitude at Point Barrow with observed climate indices. Left panels compare the time series of the CO_2 amplitude against time series of (a) North Atlantic Oscillation (NAO), (c) Pacific Decadal Oscillation (PDO), and (e) Arctic Oscillation (AO). Right panels show the corresponding scatter plots for each climate index with the correlation coefficient given in the title of each panel.

Appendix B

The figures in the Appendix B show the results for the individual diagnostics listed in Table 5.2 for all models listed in Table 5.1 In addition, they show the observations or reanalysis data that are used to constrain the projections. This supporting information thus provides a process-oriented evaluation of the representation of the austral jet stream in the CMIP5 ensemble.
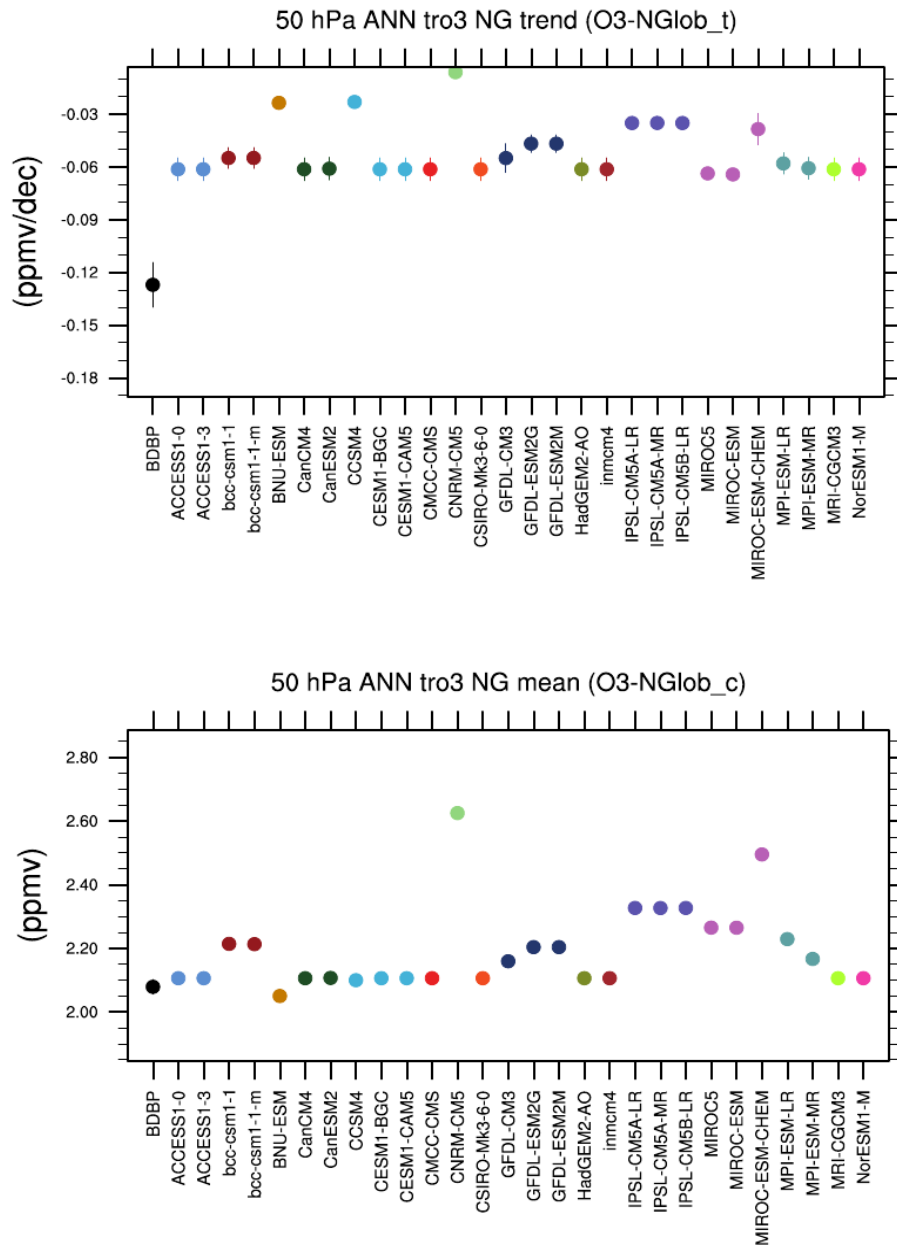

Figure B1: Trends (upper panel) and climatological mean (lower panel) in annual-mean near global (NG, 82.5N-82.5S) ozone (tro3) at 50 hPa. Vertical lines indicate the standard deviation of the mean value.
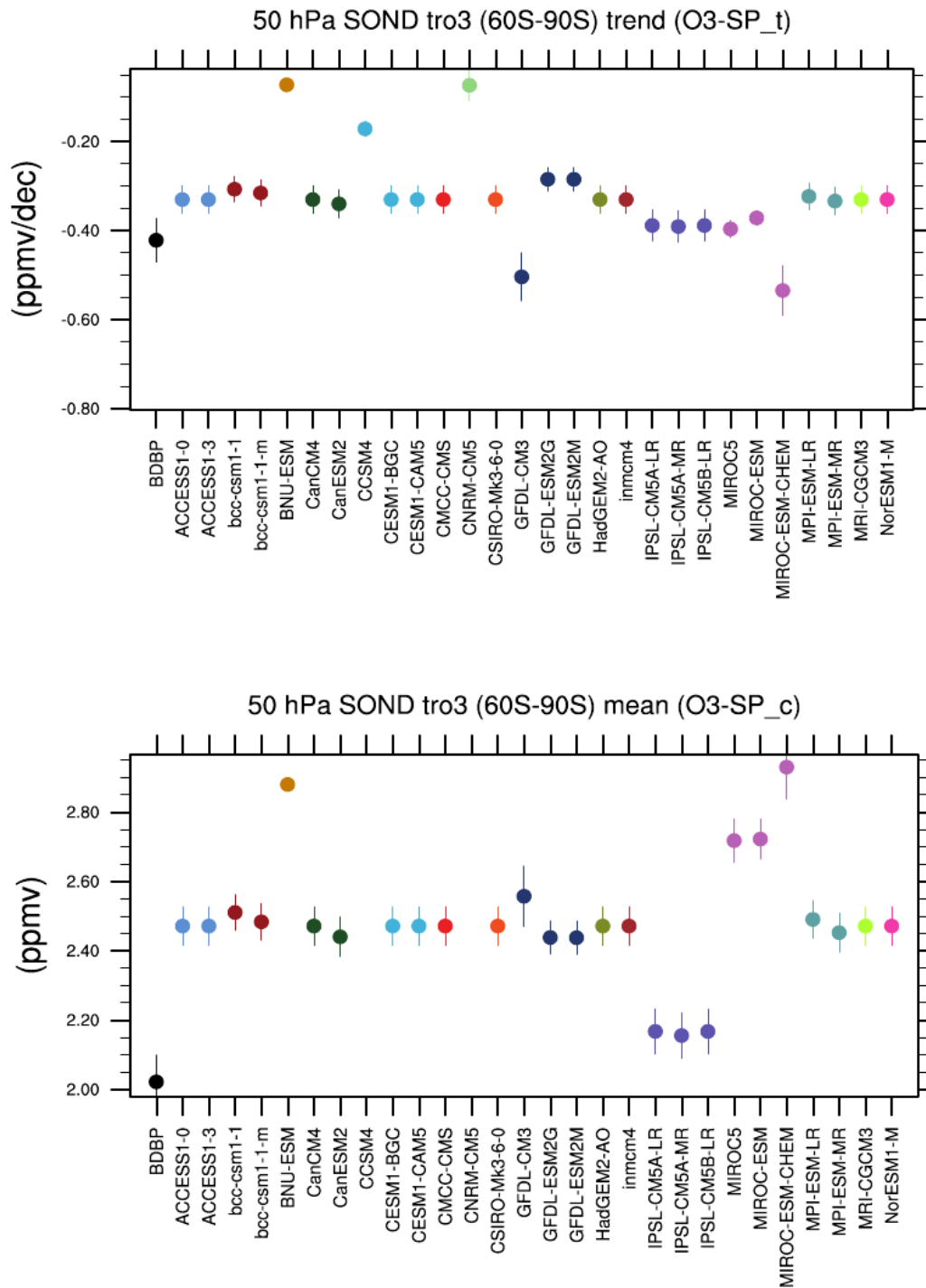
Figure B2: Trends (upper panel) and climatological mean (lower panel) in September-October-November-December (SOND) ozone (tro3) at 50 hPa over Antarctica. Vertical lines indicate the standard deviation of the mean value.
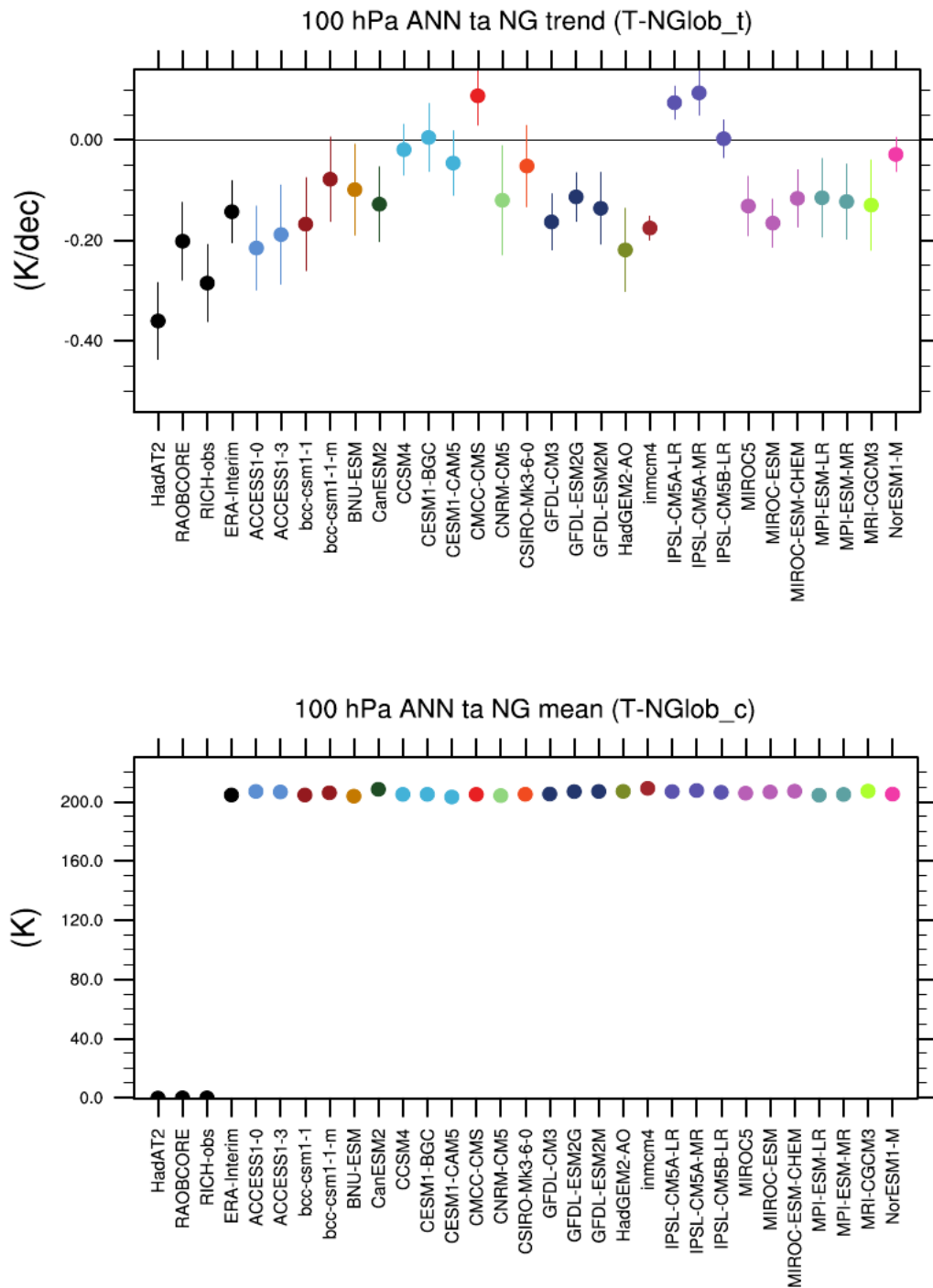
Figure B3: Trends (upper panel) and climatological mean (lower panel) in annual-mean near global (NG, 82.5°N-82.5°S) temperature anomalies (ta) at 100 hPa. Vertical lines indicate the standard deviation of the mean value.
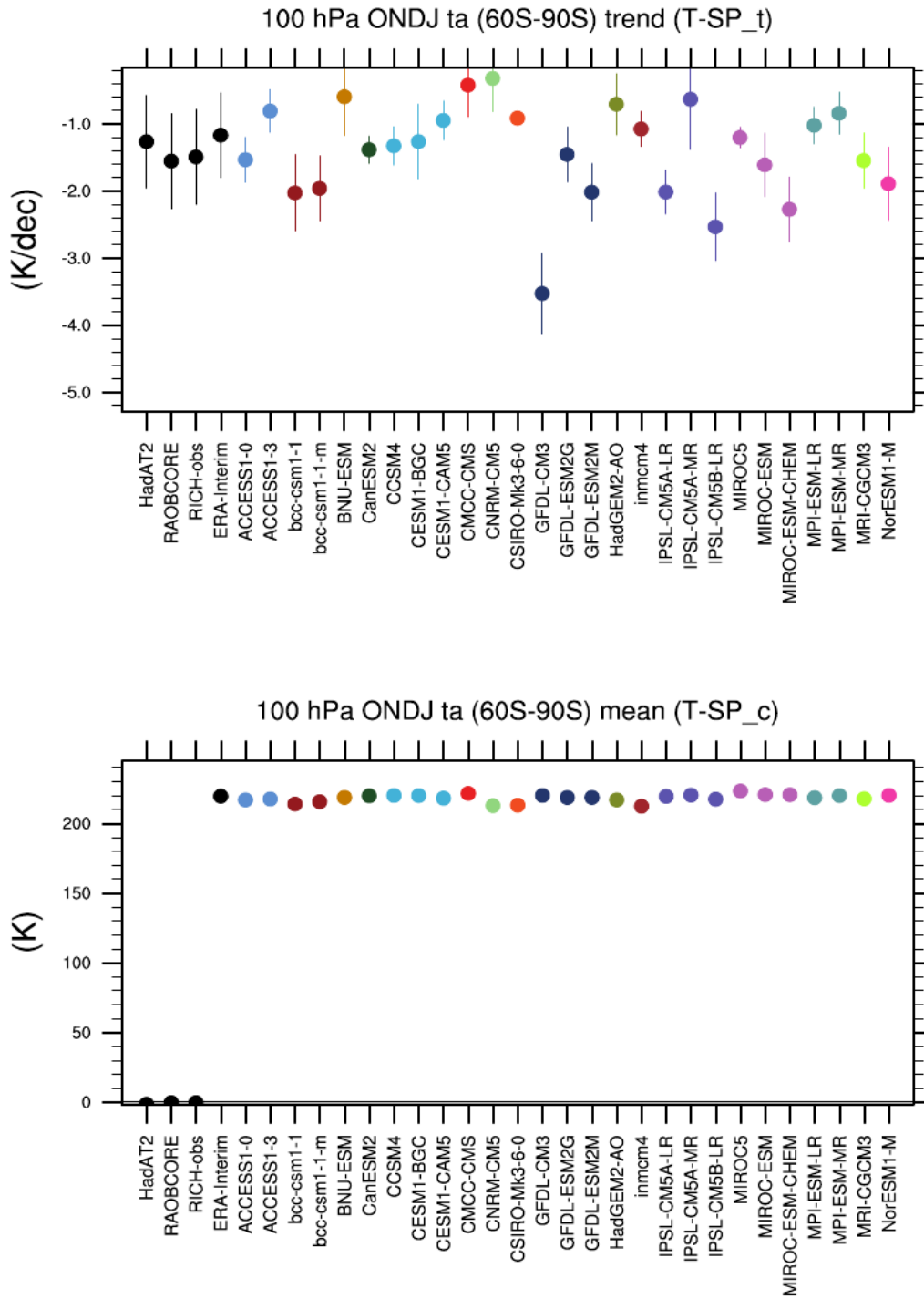
Figure B4: Trends (upper panel) and climatological mean (lower panel) in October-November-December-January (ONDJ) temperature anomalies (ta) at 100 hPa over Antarctica. Vertical lines indicate the standard deviation of the mean value.
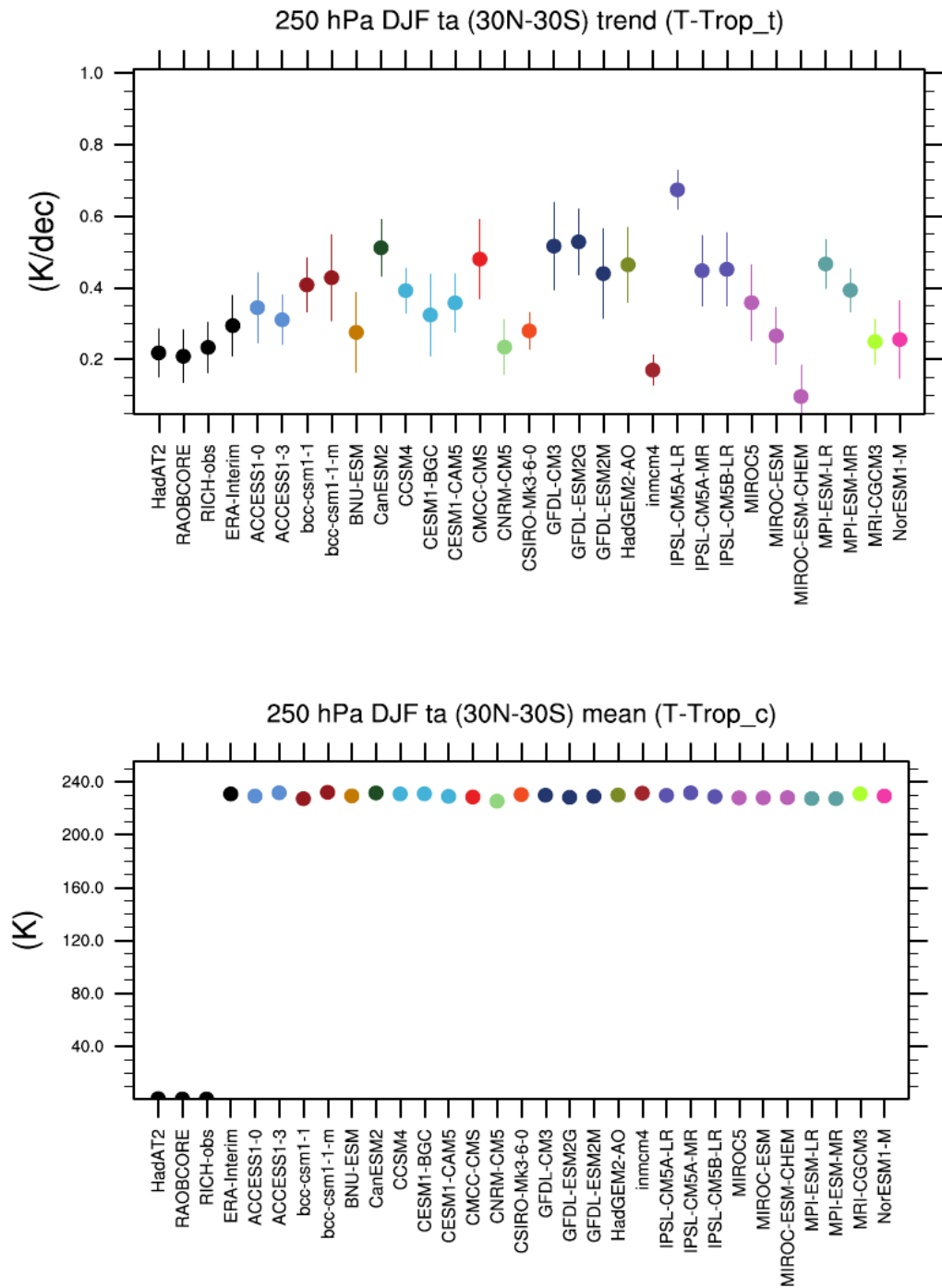
Figure B5: Trends (upper panel) and climatological mean (lower panel) in December-January-February (DJF) tropical (30N-30S) temperature anomalies (ta) at 250hPa. Vertical lines indicate the standard deviation of the mean value.
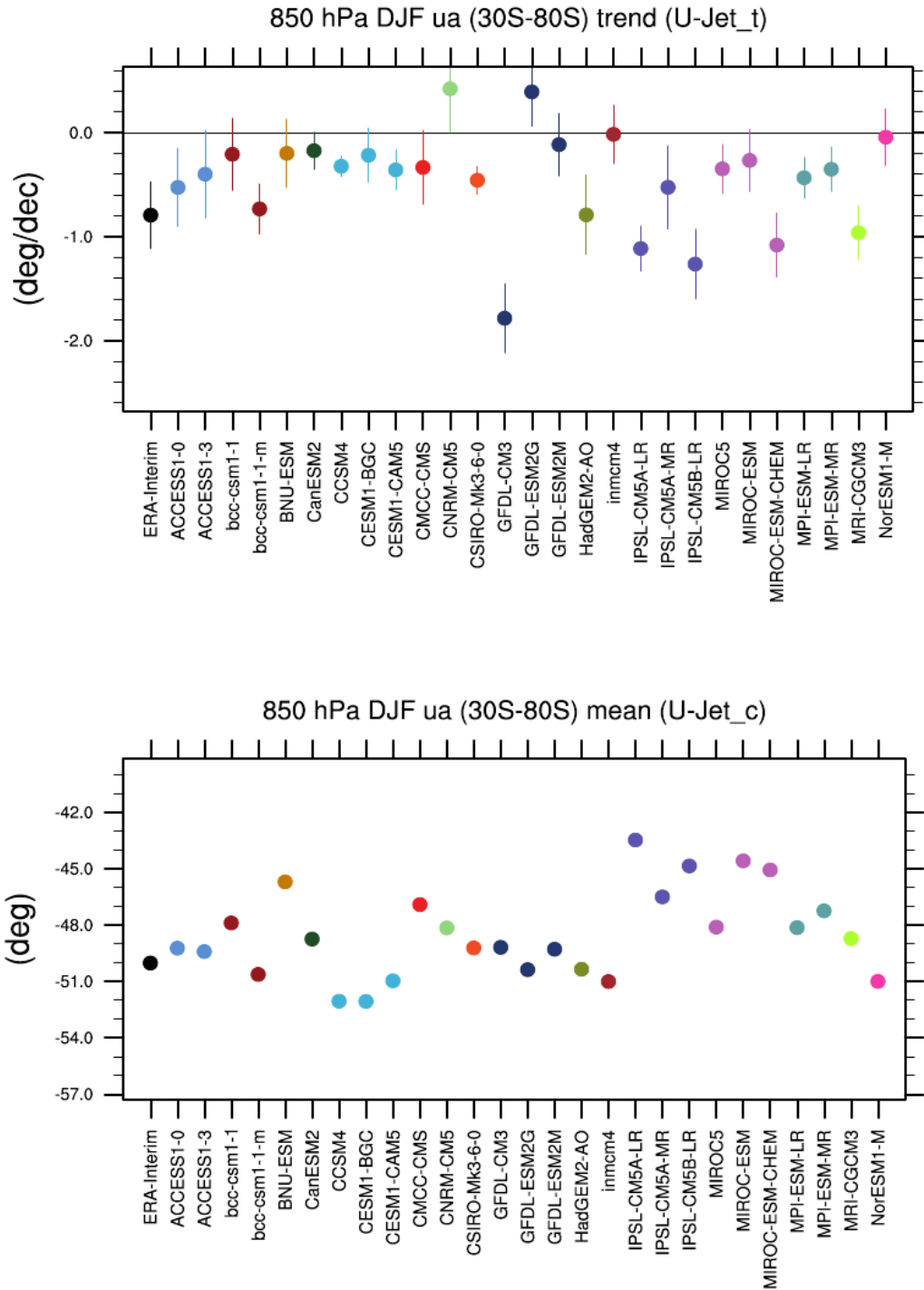
Figure B6: Trends (upper panel) and climatological mean (lower panel) in DJF Jet position at 850hPa. Vertical lines indicate the standard deviation of the mean value.
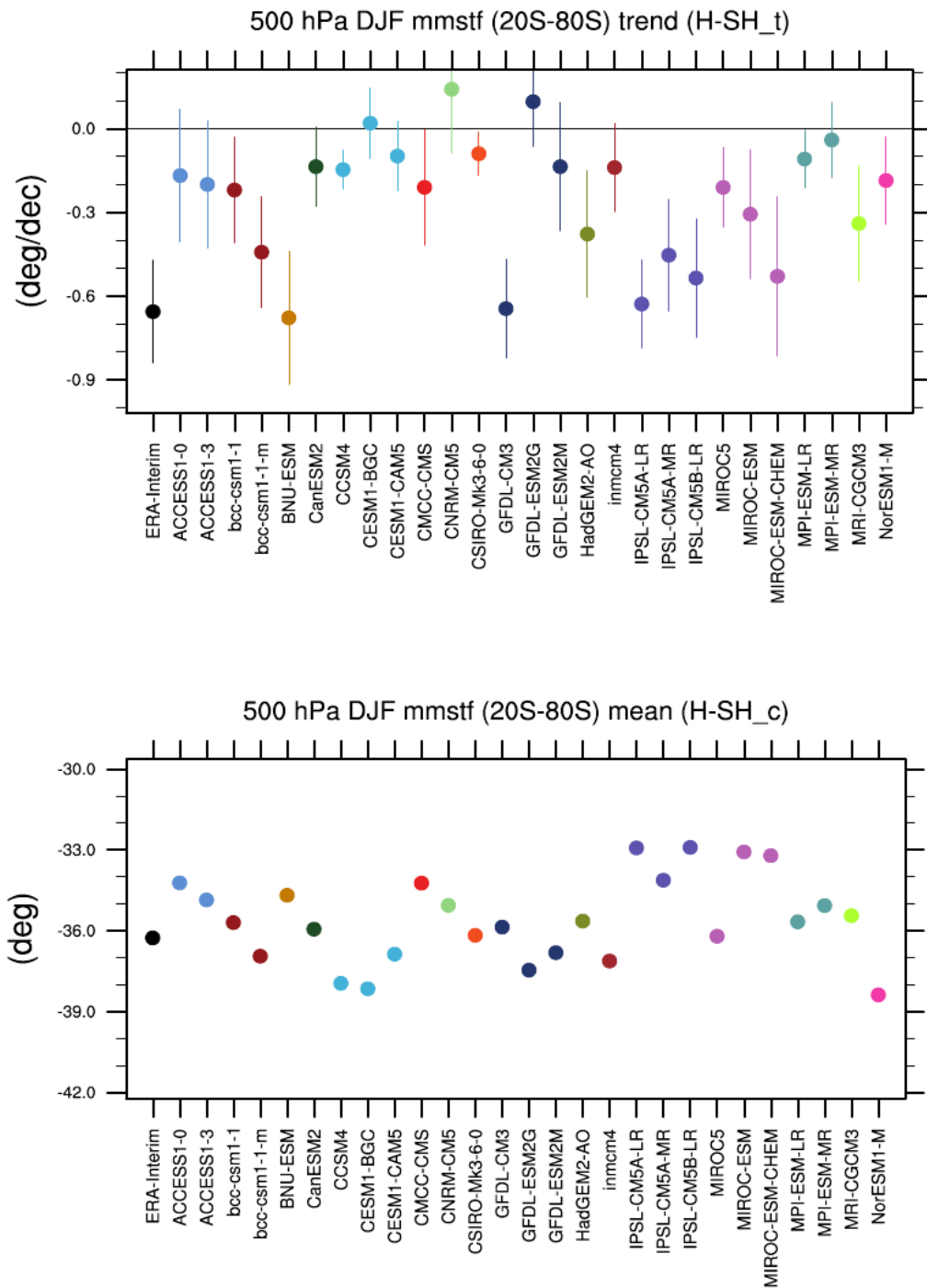
Figure B7: Trends (upper panel) and climatological mean (lower panel) in DJF Hadley cell boundary, defined by zero Ψ (mmstf) at 500 hPa. Vertical lines indicate the standard deviation of the mean value. Figure S8: Trends (upper panel) and climatological mean (lower panel) in DJF extra tropical mean tropopause pressure (tpp) integrals south of 50°S. Vertical lines indicate the standard deviation of the mean value.
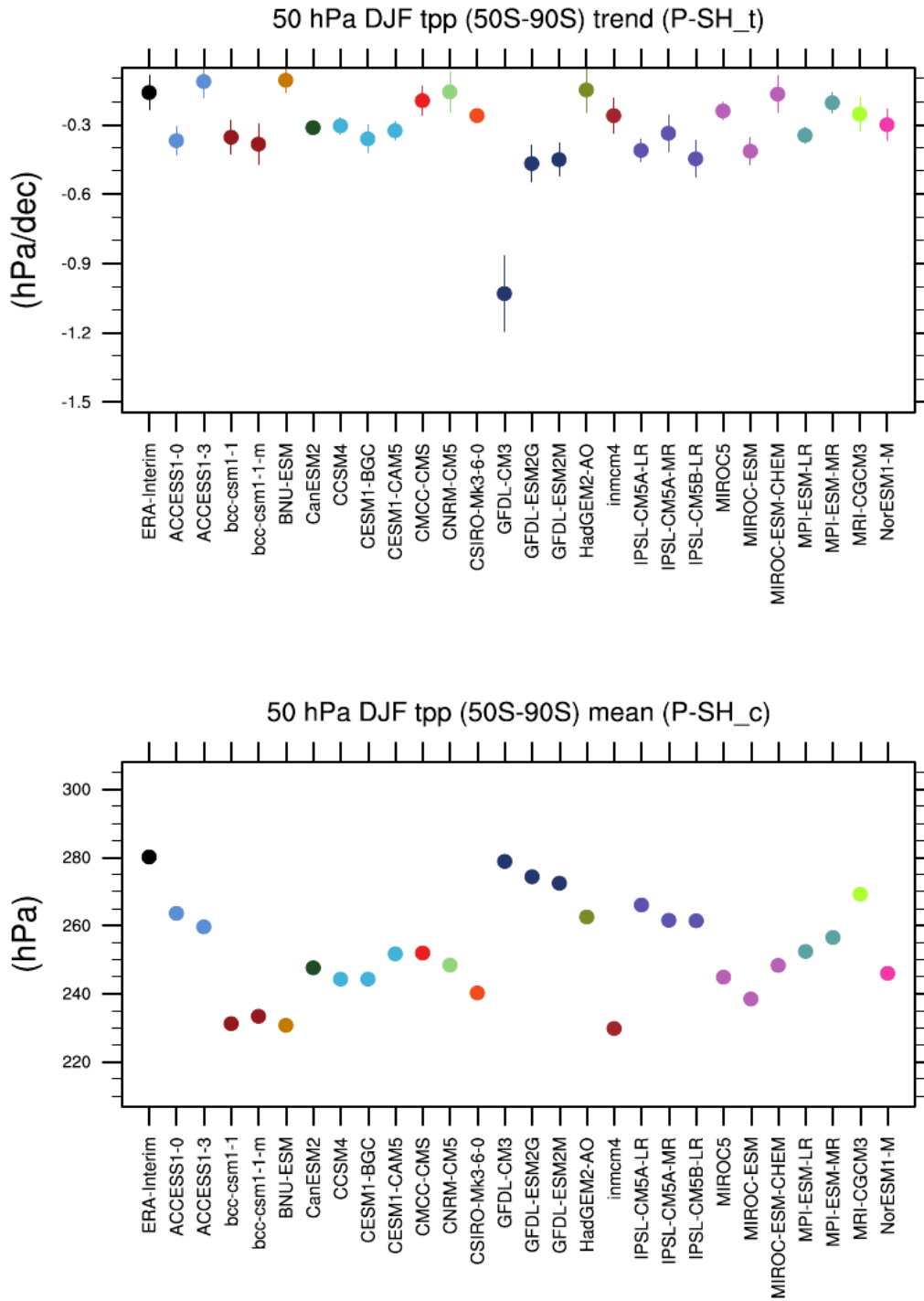
Figure B8: Trends (upper panel) and climatological mean (lower panel) in DJF extra tropical mean tropopause pressure (tpp) integrals south of 50°S. Vertical lines indicate the standard deviation of the mean value.
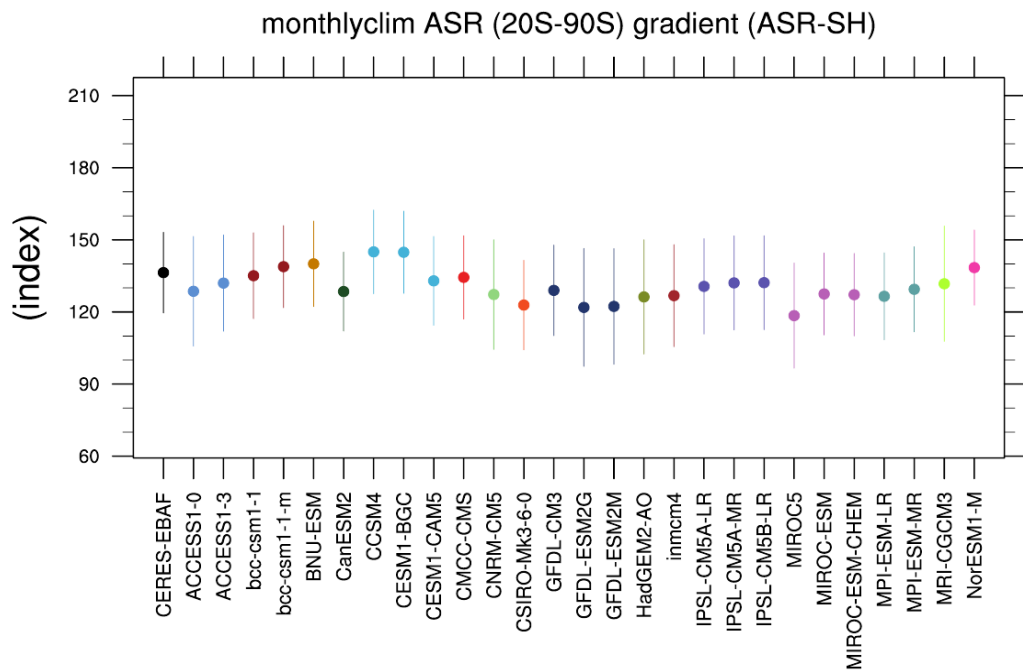
Figure B9: Mean absorbed short wave radiation (ASR = dowelling short wave radiation - upwelling short wave radiation) gradient (20°S-90°S). Vertical lines indicate the standard deviation of the mean value.
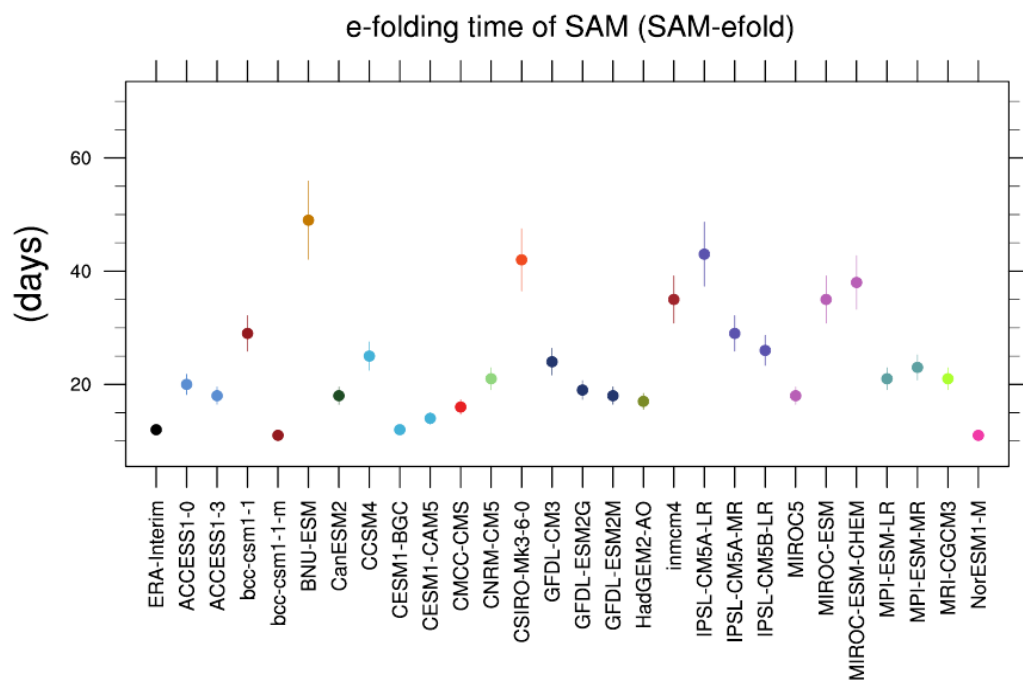
Figure B10: E-folding time of the Southern Annular Mode. Vertical lines indicate the standard deviation of the mean value.
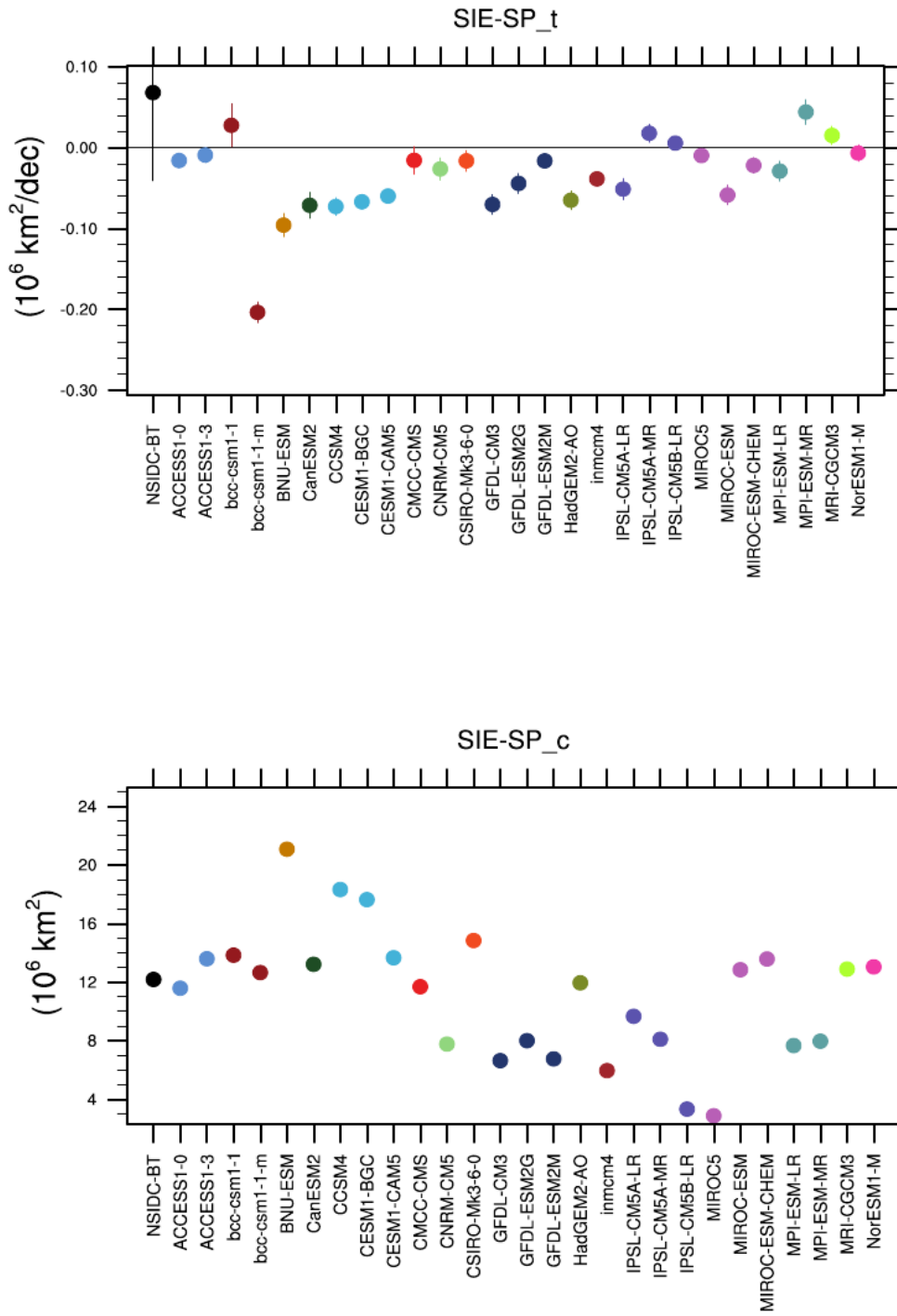
Figure B11: Trends (upper panel) and climatological mean (lower panel) in annual-mean Arctic sea ice extend. Vertical lines indicate the standard deviation of the.

Integrated Author's References

The following peer-reviewed publications were published as part of this thesis or are under review:

Wenzel, S. , Cox, P. M., Eyring, V. & Friedlingstein, P. Emergent constraints on climate-carbon cycle feedbacks in the CMIP5 Earth system models. *J. Geophys. Res. Biogeosciences* 119, 794-807 (2014).

Wenzel, S. , Cox, P. M., Eyring, V. & Friedlingstein, P. Changes in the Carbon Dioxide Seasonal Cycle Constrain Future Increases in the Land Carbon Sink. in review. *Nature.* (2015a)

Wenzel, S. , Eyring, V., Gerber, E. P. & Karpechko, A. Y. Constraining Future Summer Austral Jet Stream Positions in the CMIP5 Ensemble by Process-oriented Multiple Diagnostic Regression. *J. Clim.* (2015b). doi:10.1175/JCLI-D-15-0412.1

This thesis also contributed to the ESMValTool, by implementing diagnostics and providing a standard namelist for the analysis by Wenzel et al. (2014):

Eyring, V., Righi, M., Evaldsson, M., Lauer, A., **Wenzel, S.** et al. ESMValTool (v1.0) - a community diagnostic and performance metrics tool for routine evaluation of Earth System Models in CMIP. *Geosci. Model Dev. Discuss.* 8, 7541-7661 (2015).

References

Allen, M. R. & Ingram, W. J. (2002). Constraints on future changes in climate and the hydrologic cycle. *Nature*, 419(6903), 224–232.

Alley, R., Marotzke, J., Nordhaus, W., Overpeck, J., Peteet, D., Pielke, R. J., Pierrehumbert, R., Rhines, P., Stocker, T., Talley, L., & Wallace, J. M. (2002). *Abrupt Climate Change*. Washington, D.C.: National Academies Press.

Anav, A., Friedlingstein, P., Kidston, M., Bopp, L., Ciais, P., Cox, P., Jones, C., Jung, M., Myneni, R., & Zhu, Z. (2013). Evaluating the land and ocean components of the global carbon cycle in the CMIP5 earth system models. *Journal of Climate*, 26(18), 6801–6843.

Andres, R. J., Boden, T. A., Bréon, F.-M., Ciais, P., Davis, S., Erickson, D., Gregg, J. S., Jacobson, A., Marland, G., Miller, J., Oda, T., Olivier, J. G. J., Raupach, M. R., Rayner, P., & Treanton, K. (2012). A synthesis of carbon dioxide emissions from fossil-fuel combustion. *Biogeosciences*, 9(5), 1845–1871.

Anon, A. (2012). GFDL's ESM2 Global Coupled Climate-Carbon Earth System Models. Part I: Physical Formulation and Baseline Simulation Characteristics. *Journal of Climate*, 25(19), 6646–6665.

Arblaster, J. M. & Meehl, G. A. (2006). Contributions of external forcings to southern annular mode trends. *Journal of Climate*, 19(12), 2896–2905.

Arblaster, J. M., Meehl, G. a., & Karoly, D. J. (2011). Future climate change in the Southern Hemisphere: Competing effects of ozone and greenhouse gases. *Geophysical Research Letters*, 38(2), L02701.

Arora, V. K., Boer, G. J., Friedlingstein, P., Eby, M., Jones, C. D., Christian, J. R., Bonan, G., Bopp, L., Brovkin, V., Cadule, P., Hajima, T., Ilyina, T., Lindsay, K., Tjiputra, J. F., & Wu, T. (2013). Carbon-concentration and carbon-climate feedbacks in CMIP5 earth system models. *Journal of Climate*, 26(15), 5289–5314.

Arora, V. K., Scinocca, J. F., Boer, G. J., Christian, J. R., Denman, K. L., Flato, G. M., Kharin, V. V., Lee, W. G., & Merryfield, W. J. (2011). Carbon emission limits required to satisfy future representative concentration pathways of greenhouse gases. *Geophysical Research Letters*, 38(5), 3–8.

Assmann, K. M., Bentsen, M., Segschneider, J., & Heinze, C. (2010). An isopycnic ocean carbon cycle model. *Geoscientific Model Development*, 3(1), 143–167.

Aumont, O. (2003). An ecosystem model of the global ocean including Fe, Si, P colimitations. *Global Biogeochemical Cycles*, 17(2), 1060.

Barichivich, J., Briffa, K. R., Myneni, R. B., Osborn, T. J., Melvin, T. M., Ciais, P., Piao, S., & Tucker, C. (2013). Large-scale variations in the vegetation growing season and annual cycle of atmospheric CO2 at high northern latitudes from 1950 to 2011. *Global Change Biology*, 19(10), 3167–3183.

Barnes, E. a. & Hartmann, D. L. (2010). Testing a theory for the effect of latitude on the persistence of eddy-driven jets using CMIP3 simulations. *Geophysical Research Letters*, 37(15), 1–5.

Barnes, E. A. & Polvani, L. (2013). Response of the midlatitude jets, and of their variability, to increased greenhouse gases in the CMIP5 models. *Journal of Climate*, 26(18), 7117–7135.

Bell, T. (1980). Climate sensitivity from fluctuation dissipation: Some simple model tests. *Journal of the Atmospheric Sciences*, 37, 1700–1707.

Bengtsson, L., Hodges, K. I., & Roeckner, E. (2006). Storm tracks and climate change. *Journal of Climate*, 19(15), 3518–3543.

Berrisford, P., Dee, D., Poli, P., Brugge, R., Fielding, K., Fuentes, M., Kallberg, P., Kobayashi, S., Uppala, S., & Simmons, A. (2011). *The ERA-Interim archive Version 2.0 Institution ECMWF*. Technical report, ECMWF, Reading.

Bindoff, N., Stott, P., AchutaRao, K., Allen, M., Gillett, N., Gutzler, D., Hansingo, K., Hegerl, G., Hu, Y., Jain, S., Mokhov, I., Overland, J., Perlwitz, J., Sebbari, R., & Zhang, X. (2013). Detection and Attribution of Climate Change: from Global to Regional. In Intergovernmental Panel on Climate Change (Ed.), *Climate Change 2013 - The Physical Science Basis* chapter 10, (pp. 867–952). Cambridge: Cambridge University Press.

Boé, J., Hall, A., & Qu, X. (2009a). Deep ocean heat uptake as a major source of spread in transient climate change simulations. *Geophysical Research Letters*, 36(22), L22701.

Boé, J., Hall, A., & Qu, X. (2009b). September sea-ice cover in the Arctic Ocean projected to vanish by 2100. *Nature Geoscience*, 2(5), 341–343.

Bony, S., Colman, R., Kattsov, V. M., Allan, R. P., Bretherton, C. S., Dufresne, J.-L., Hall, A., Hallegatte, S., Holland, M. M., Ingram, W., Randall, D. A., Soden, B. J., Tselioudis, G., & Webb, M. J. (2006). How Well Do We Understand and Evaluate Climate Change Feedback Processes? *Journal of Climate*, 19(15), 3445–3482.

Bony, S., Dufresne, J.-L., Le Treut, H., Morcrette, J.-J., & Senior, C. (2004). On dynamic and thermodynamic components of cloud changes. *Climate Dynamics*, 22(2-3), 71–86.

Booth, B. B. B., Jones, C. D., Collins, M., Totterdell, I. J., Cox, P. M., Sitch, S., Huntingford, C., Betts, R. a., Harris, G. R., & Lloyd, J. (2012). High sensitivity of future global warming to land carbon cycle processes.

Boucher, O., Randall, D., Artaxo, P., Bretherton, C., Feingold, G., Forster, P., Kerminen, V.-M., Kondo, Y., Liao, H., Lohmann, U., Rasch, P., Satheesh, S., Sherwood, S., Stevens, B., & Zhang, X. (2013). Clouds and Aerosols. In Intergovernmental Panel on Climate Change (Ed.), *Climate Change 2013 - The Physical Science Basis* chapter 7, (pp. 571–658). Cambridge: Cambridge University Press, stocker, t edition.

Bousquet, P., Peylin, P., Ciais, P., Le Quéré, C., Friedlingstein, P., & Tans, P. P. (2000). Regional Changes in Carbon Dioxide Fluxes of Land and Oceans Since 1980. *Science*, 290(5495), 1342–1346.

Bracegirdle, T. J., Bertler, N., Carleton, A. M., Ding, Q., Fogwill, C. J., Fyfe, J. C., Hellmer, H., Karpechko, A. Y., Kusahara, K., Larour, E., Mayewski, P. A., Meier, W. N., Polvani, L. M., Russell, J. L., Stevenson, S. L., Turner, J., van Wessem, J. M., van de Berg, W., & Wainer, I. (2015). A multi-disciplinary perspective on climate model evaluation for Antarctica. *Bulletin of the American Meteorological Society*.

Bracegirdle, T. J. & Stephenson, D. B. (2012). Higher precision estimates of regional polar warming by ensemble regression of climate model projections. *Climate Dynamics*, 39(12), 2805–2821.

Bracegirdle, T. J. & Stephenson, D. B. (2013). On the robustness of emergent constraints used in multimodel climate change projections of arctic warming. *Journal of Climate*, 26(2), 669–678.

Buermann, W., Lintner, B. R., Koven, C. D., Angert, A., Pinzon, J. E., Tucker, C. J., & Fung, I. Y. (2007). The changing carbon cycle at Mauna Loa Observatory. *Proceedings of the National Academy of Sciences of the United States of America*, 104(11), 4249–4254.

Caldwell, P. M., Bretherton, C. S., Zelinka, M. D., Klein, S. A., Santer, B. D., & Sanderson, B. M. (2014). Statistical significance of climate sensitivity predictors obtained by data mining. *Geophysical Research Letters*, 41, 1803–1808.

Calvo, N., Garcia, R. R., Marsh, D. R., Mills, M. J., Kinnison, D. E., & Young, P. J. (2012). Reconciling modeled and observed temperature trends over Antarctica. *Geophysical Research Letters*, 39(16).

Cavalieri, D. J., Parkinson, C. L., Gloersen, P., & Zwally, H. (2006). *Sea Ice Concentrations from Nimbus-7 SMMR and DMSP SSM/I-SSMIS Passive Microwave Data.* Technical report, Boulder, Colorado USA.

Ceppi, P., Zelinka, M. D., & Hartmann, D. L. (2014). The response of the Southern Hemispheric eddy-driven jet to future changes in shortwave radiation in CMIP5. *Geophysical Research Letters*, 41, 3244–3250.

Chang, E. K. M., Guo, Y., & Xia, X. (2012). CMIP5 multimodel ensemble projection of storm track change under global warming. *Journal of Geophysical Research*, 117, D23118.

Chen, G. & Held, I. M. (2007). Phase speed spectra and the recent poleward shift of Southern Hemisphere surface westerlies. *Geophysical Research Letters*, 34(21), L21805.

Ciais, P., Reichstein, M., Viovy, N., Granier, A., Ogée, J., Allard, V., Aubinet, M., Buchmann, N., Bernhofer, C., Carrara, A., Chevallier, F., De Noblet, N., Friend, A. D., Friedlingstein, P., Grünwald, T., Heinesch, B., Keronen, P., Knohl, A., Krinner, G., Loustau, D., Manca, G., Matteucci, G., Miglietta, F., Ourcival, J. M., Papale, D., Pilegaard, K., Rambal, S., Seufert, G., Soussana, J. F., Sanz, M. J., Schulze, E. D., Vesala, T., & Valentini, R. (2005). Europe-wide reduction in primary productivity caused by the heat and drought in 2003. *Nature*, 437(7058), 529–33.

Ciais, P., Sabine, C., Bala, G., Bopp, L., Brovkin, V., Canadell, J., Chhabra, A., DeFries, R., Galloway, J., Heimann, M., Jones, C., Quéré, C. L., Myneni, R., Piao, S., & Thornton, P. (2013). Carbon and Other Biogeochemical Cycles. In T. Stocker, D. Qin, G.-K. Plattner, M. Tignor, S. Allen, J. Boschung, A. Nauels, Y. Xia, V. Bex, & P. Midgley (Eds.), *Climate Change 2013: The Physical Science Basis* chapter 6. Cambridge, United Kingdom and New York, NY, USA.: Cambridge University Press.

Cionni, I., Eyring, V., Lamarque, J. F., Randel, W. J., Stevenson, D. S., Wu, F., Bodeker, G. E., Shepherd, T. G., Shindell, D. T., & Waugh, D. W. (2011). Ozone database in support of CMIP5 simulations: Results and corresponding radiative forcing. *Atmospheric Chemistry and Physics*, 11(21), 11267–11292.

Clark, D. B., Mercado, L. M., Sitch, S., Jones, C. D., Gedney, N., Best, M. J., Pryor, M., Rooney, G. G., Essery, R. L. H., Blyth, E., Boucher, O., Harding, R. J., Huntingford, C., & Cox, P. M. (2011). The Joint UK Land Environment Simulator (JULES), model description. Part 2: Carbon fluxes and vegetation dynamics. *Geoscientific Model Development*, 4(3), 701–722.

Clarke, L., Edmonds, J., Jacoby, H., Pitcher, H., Reilly, J., & Richels, R. (2007). Scenarios of Greenhouse Gas Emissions and Atmospheric Concentrations. In *Sub-report 2.1A of Synthesis and Assessment Product 2.1 by the U.S. Climate Change Science Program and the Subcommittee on Global Change Research* (pp. 154). Department of Energy, Office of Biological & Environmental Research, Washington, 7 DC., USA.

Collins, M., Knutti, R., Arblaster, J. M., Dufresne, J.-L., Fichefet, T., Friedlingstein, P., Gao, X., Jr., W. J. G., Johns, T., Krinner, G., Shongwe, M., Tebaldi, C., Weaver, A. J., & Wehner, M. (2013). Long-term Climate Change: Projections, Commitments and Irreversibility. In: Climate Change 2013: The Physical Science Basis. Contribution of Working Group I to the Fifth Assessment Report of the Intergovernmental Panel on Climate Change [Stocker, T. F., D. *Cambridge, United Kingdom and New York, NY, USA*, in press.

Collins, W. D., Bitz, C. M., Blackmon, M. L., Bonan, G. B., Bretherton, C. S., Carton, J. A., Chang, P., Doney, S. C., Hack, J. J., Henderson, T. B., Kiehl, J. T., Large, W. G., McKenna, D. S., Santer, B. D., & Smith, R. D. (2006). The Community Climate System Model Version 3 (CCSM3). *Journal of Climate*, 19(11), 2122–2143.

Collins, W. J., Bellouin, N., Doutriaux-Boucher, M., Gedney, N., Halloran, P., Hinton, T., Hughes, J., Jones, C. D., Joshi, M., Liddicoat, S., Martin, G., O'Connor, F., Rae, J., Senior, C., Sitch, S., Totterdell, I., Wiltshire, A., & Woodward, S. (2011). Development and evaluation of an Earth-System model - HadGEM2. *Geoscientific Model Development*, 4(4), 1051–1075.

Cox, P. M., Betts, R. A., Collins, M., Harris, P. P., Huntingford, C., & Jones, C. D. (2004). Amazonian forest dieback under climate-carbon cycle projections for the 21st century. *Theoretical and Applied Climatology*, 78(1-3), 137–156.

Cox, P. M., Betts, R. A., Jones, C. D., Spall, S. A., & Totterdell, I. J. (2000). Acceleration of global warming due to carbon-cycle feedbacks in a coupled climate model. *Nature*, 408(6809), 184–187.

Cox, P. M., Pearson, D., Booth, B. B., Friedlingstein, P., Huntingford, C., Jones, C. D., & Luke, C. M. (2013). Sensitivity of tropical carbon to climate change constrained by carbon dioxide variability. *Nature*, 494(7437), 341–344.

Crook, J. A. & Forster, P. M. (2014). Comparison of surface albedo feedback in climate models and observations. *Geophysical Research Letters*, 41(5), 1717–1723.

Cubasch, U., Wuebbles, D., Chen, D., Faccini, M. C., Frame, D., Mahowald, N., & J.-G., W. (2013). Introduction. In *Climate Change 2013 - The Physical Science Basis. Contribution of Workinggroup I to the Fith Assessment Report of the Intergovernmental Panel on Climate Change* chapter 1, (pp. 119–158). Cambridge University Press.

Dee, D. P., Uppala, S. M., Simmons, A. J., Berrisford, P., Poli, P., Kobayashi, S., Andrae, U., Balmaseda, M. A., Balsamo, G., Bauer, P., Bechtold, P., Beljaars, A. C. M., van de Berg, L., Bidlot, J., Bormann, N., Delsol, C., Dragani, R., Fuentes, M., Geer, A. J., Haimberger, L., Healy, S. B., Hersbach, H., Hólm, E. V., Isaksen, L., Kållberg, P., Köhler, M., Matricardi, M., McNally, A. P., Monge-Sanz, B. M., Morcrette, J.-J., Park, B.-K., Peubey, C., de Rosnay, P., Tavolato, C., Thépaut, J.-N., & Vitart, F. (2011). The ERA-Interim reanalysis: configuration and performance of the data assimilation system. *Quarterly Journal of the Royal Meteorological Society*, 137(656), 553–597.

Denman, K. L., Brasseur, G., Chidthaisong, A., Ciais, P., Cox, P. M., Dickinson, R. E., Hauglustaine, D., Heinze, C., Holland, E., Jacob, D., Lohmann, U., Ramachandran, S., da Silva Dias, P., Wofsy, S. C., & Zhang, X. (2007). Couplings Between Changes in the Climate System and Biogeochemistry. In: Climate Change 2007: The Physical Science Basis. Contribution of Working Group I to the Fourth Assessment Report of the Intergovernmental Panel on Climate Change [Solomon, S., D. Qin. *Cambridge, United Kingdom and New York, NY, USA*, (pp. 499–587).

Deser, C., Alexander, M. A., Xie, S.-P., & Phillips, A. S. (2010). Sea surface temperature variability: patterns and mechanisms. *Annual review of marine science*, 2, 115–143.

Dix, M., Vohralik, P., Bi, D., Rashid, H., Marsland, S., Farrell, S. O., Uotila, P., Hirst, T., Kowalczyk, E., Sullivan, A., Yan, H., Franklin, C., Sun, Z., Watterson, I., Collier, M., Noonan, J., Rotstayn, L., Stevens, L., Uhe, P., & Puri, K. (2013). The ACCESS coupled model: documentation of core CMIP5 simulations and initial results. *Australian Meteorological and Oceanographic Journal*, 63(1), 83–99.

Dlugokencky, E. & Tans, P. (2014). NOAA/ESRL.

Doelling, D. R., Loeb, N. G., Keyes, D. F., Nordeen, M. L., Morstad, D., Nguyen, C., Wielicki, B. A., Young, D. F., & Sun, M. (2013). Geostationary enhanced temporal interpolation for CERES flux products. *J. Atmos. Oceanic Technol*, 30, 1072–1090.

Donner, L. J., Wyman, B. L., Hemler, R. S., Horowitz, L. W., Ming, Y., Zhao, M., Golaz, J.-C., Ginoux, P., Lin, S.-J., Schwarzkopf, M. D., Austin, J., Alaka, G., Cooke, W. F., Delworth, T. L., Freidenreich, S. M., Gordon, C. T., Griffies, S. M., Held, I. M., Hurlin, W. J., Klein, S. A., Knutson, T. R., Langenhorst, A. R., Lee, H.-C., Lin, Y., Magi, B. I., Malyshev, S. L., Milly, P. C. D., Naik, V., Nath, M. J., Pincus, R., Ploshay, J. J., Ramaswamy, V., Seman, C. J., Shevliakova, E., Sirutis, J. J., Stern, W. F., Stouffer, R. J., Wilson, R. J., Winton, M., Wittenberg, A. T., & Zeng, F. (2011). The Dynamical Core, Physical Parameterizations, and Basic Simulation Characteristics of the Atmospheric Component AM3 of the GFDL Global Coupled Model CM3. *Journal of Climate*, 24(13), 3484–3519.

Dufresne, J.-L., Foujols, M.-A., Denvil, S., Caubel, A., Marti, O., Aumont, O., Balkanski, Y., Bekki, S., Bellenger, H., Benshila, R., Bony, S., Bopp, L., Braconnot, P., Brockmann, P., Cadule, P., Cheruy, F., Codron, F., Cozic, A., Cugnet, D., Noblet, N., Duvel, J.-P., Ethé, C., Fairhead, L., Fichefet, T., Flavoni, S., Friedlingstein, P., Grandpeix, J.-Y., Guez, L., Guilyardi, E., Hauglustaine, D., Hourdin, F., Idelkadi, A., Ghattas, J., Joussaume, S., Kageyama, M., Krinner, G., Labetoulle, S., Lahellec, A., Lefebvre, M.-P., Lefevre, F., Levy, C., Li, Z. X., Lloyd, J., Lott, F., Madec, G., Mancip, M., Marchand, M., Masson, S., Meurdesoif, Y., Mignot, J., Musat, I., Parouty, S., Polcher, J., Rio, C., Schulz, M., Swingedouw, D., Szopa, S., Talandier, C., Terray, P., Viovy, N., & Vuichard, N. (2013). Climate change projections using the IPSL-CM5 Earth System Model: from CMIP3 to CMIP5. *Climate Dynamics*, 40(9-10), 2123–2165.

Dunne, J. P., John, J. G., Shevliakova, S., Stouffer, R. J., Krasting, J. P., Malyshev, S. L., Milly, P. C. D., Sentman, L. T., Adcroft, A. J., Cooke, W., Dunne, K. a., Griffies, S. M., Hallberg, R. W., Harrison, M. J., Levy, H., Wittenberg, A. T., Phillips, P. J., & Zadeh, N. (2013). GFDL's ESM2 global coupled climate-carbon earth system models. Part II: Carbon system formulation and baseline simulation characteristics. *Journal of Climate*, 26(7), 2247–2267.

Eyring, V., Arblaster, J. M., Cionni, I., Sedláček, J., Perlwitz, J., Young, P. J., Bekki, S., Bergmann, D., Cameron-Smith, P., Collins, W. J., Faluvegi, G., Gottschaldt, K. D., Horowitz, L. W., Kinnison, D. E., Lamarque, J. F., Marsh, D. R., Saint-Martin, D., Shindell, D. T., Sudo, K., Szopa, S., & Watanabe, S. (2013). Long-term ozone changes and associated climate impacts in CMIP5 simulations. *Journal of Geophysical Research: Atmospheres*, 118(10), 5029–5060.

Eyring, V., Harris, N. R. P., Rex, M., Shepherd, T. G., Fahey, D. W., Amanatidis, G. T., Austin, J., Chipperfield, M. P., Dameris, M., Forster, P. M. D. F., Gettelman, A., Graf, H. F., Nagashima, T., Newman, P. A., Pawson, S., Prather, M. J., Pyle, J. A., Salawitch, R. J., Santer, B. D., & Waugh, D. W. (2005). A Strategy for Process-Oriented Validation of Coupled Chemistry-Climate Models. *Bulletin of the American Meteorological Society*, 86(8), 1117–1133.

Eyring, V., Righi, M., Evaldsson, M., Lauer, A., Wenzel, S., Jones, C., Anav, A., Andrews, O., Cionni, I., Davin, E. L., Deser, C., Ehbrecht, C., Friedlingstein, P., Gleckler, P., Gottschaldt, K.-D., Hagemann, S., Juckes, M., Kindermann, S., Krasting, J., Kunert, D., Levine, R., Loew, A., Mäkelä, J., Martin, G., Mason, E., Phillips, A., Read, S., Rio, C., Roehrig, R., Senftleben, D., Sterl, A., van Ulft, L. H., Walton, J., Wang, S., & Williams, K. D. (2015). ESMValTool (v1.0) - a community diagnostic and performance metrics tool for routine evaluation of Earth System Models in CMIP. *Geoscientific Model Development Discussions*, 8(9), 7541–7661.

Eyring, V., Waugh, D. W., Bodeker, G. E., Cordero, E., Akiyoshi, H., Austin, J., Beagley, S. R., Boville, B. A., Braesicke, P., Brühl, C., Butchart, N., Chipperfield, M. P., Dameris, M., Deckert, R., Deushi, M., Frith, S. M., Garcia, R. R., Gettelman, A., Giorgetta, M. A., Kinnison, D. E., Mancini, E., Manzini, E., Marsh, D. R., Matthes, S., Nagashima, T., Newman, P. A., Nielsen, J. E., Pawson, S., Pitari, G., Plummer, D. A., Rozanov, E., Schraner, M., Scinocca, J. F., Semeniuk, K., Shepherd, T. G., Shibata, K., Steil, B., Stolarski, R. S., Tian, W., & Yoshiki, M. (2007). Multimodel projections of stratospheric ozone in the 21st century. *Journal of Geophysical Research*, 112(D16), D16303.

Fasullo, J. T., Sanderson, B. M., & Trenberth, K. E. (2015). Recent Progress in Constraining Climate Sensitivity With Model Ensembles. *Current Climate Change Reports*, 1(4), 268–275.

Fasullo, J. T. & Trenberth, K. E. (2012). A less cloudy future: the of subtropical subsidence in climate sensitivity. *Science*, (338), 792–794.

Flato, G., Marotzke, J., Kattsov, V., Federation, R., Reason, C., Africa, S., Uk, A. A., Uk, T. A., Baehr, J., Uk, A. B.-s., Catto, J., Canada, J. S., & Uk, A. S. (2013). Evaluation of Climate Models. In T. Stocker, D. Qin, G.-K. Plattner, M. Tignor, S. Allen, J. Boschung, A. Nauels, Y. Xia, V. Bex, & P. Midgley (Eds.), *Climate Change 2013: The Physical Science Basis* chapter 9. Cambridge, United Kingdom and New York, NY, USA: Cambridge University Press, contributi edition.

Flato, G. M. (2011). Earth system models: an overview. *Wiley Interdisciplinary Reviews: Climate Change*, 2(6), 783–800.

Francey, R. J., Tans, P. P., Allison, C. E., Enting, I. G., White, J. W. C., & Trolier, M. (1995). Changes in oceanic and terrestrial carbon uptake since 1982. *Nature*, 373(6512), 326–330.

Friedlingstein, P., Bopp, L., Ciais, P., Dufresne, J.-l., Fairhead, L., Monfray, P., & Orr, J. (2001). Positive feedback between future climate change and the carbon cycle Climate Impact on Land Uptake. *Geophysical Research Letters*, 28(8), 1543–1546.

Friedlingstein, P., Cox, P., Betts, R., Bopp, L., Brovkin, V., Cadule, P., Doney, S., Eby, M., Fung, I., Bala, G., John, J., Jones, C., Joos, F., Kato, T., Kawamiya, M., Knorr, W., Lindsay, K., Matthews, H. D., Raddatz, T., Rayner, P., Reick, C., Roeckner, E., Schnitzler, K. G., Schnurr, R., Strassmann, K., Thompson, S., J Weaver, A., Yoshikawa, C., Zeng, N., Von Bloh, W., Schnur, R., & Weaver, A. J. (2006). Climate - Carbon Cycle Feedback Analysis: Results from the C4MIP Model Intercomparison. *Journal of Climate*, 19(14), 3337–3353.

Friedlingstein, P., Dufresne, J., Cox, P., & Rayner, P. (2003). How positive is the feedback between climate change and the carbon cycle? *Tellus B*, 55, 692–700.

Friedlingstein, P., Meinshausen, M., Arora, V. K., Jones, C. D., Anav, A., Liddicoat, S. K., & Knutti, R. (2014). Uncertainties in CMIP5 climate projections due to carbon cycle feedbacks. *Journal of Climate*, 27(2), 511–526.

Fröhlich, C. & Lean, J. (2004). Solar radiative output and its variability: evidence and mechanisms. *The Astronomy and Astrophysics Review*, 12(4), 273–320.

Fujino, J., Nair, R., Kainuma, M., Masui, T., & Matsuoka, Y. (2006). *Multi-gas mitigation analysis on stabilization scenarios using AIM global model. Multigas Mitigation and Climate Policy.* Number The Energy Journal Special Issue.

Garfinkel, C. I., Waugh, D. W., & Gerber, E. P. (2013). The effect of tropospheric jet latitude on coupling between the stratospheric polar vortex and the troposphere. *Journal of Climate*, 26(6), 2077–2095.

Gastineau, G. & Soden, B. J. (2009). Model projected changes of extreme wind events in response to global warming. *Geophysical Research Letters*, 36(10), L10810.

Gent, P. R., Danabasoglu, G., Donner, L. J., Holland, M. M., Hunke, E. C., Jayne, S. R., Lawrence, D. M., Neale, R. B., Rasch, P. J., Vertenstein, M., Worley, P. H., Yang, Z.-L., & Zhang, M. (2011). The Community Climate System Model Version 4. *Journal of Climate*, 24(19), 4973–4991.

Gerber, E. P., Polvani, L. M., & Ancukiewicz, D. (2008a). Annular mode time scales in the intergovernmental panel on climate change fourth assessment report models. *Geophysical Research Letters*, 35(22), L22707.

Gerber, E. P. & Son, S. W. (2014). Quantifying the summertime response of the Austral jet stream and hadley cell to stratospheric ozone and greenhouse gases. *Journal of Climate*, 27(14), 5538–5559.

Gerber, E. P., Voronin, S., & Polvani, L. M. (2008b). Testing the Annular Mode Autocorrelation Time Scale in Simple Atmospheric General Circulation Models. *Monthly Weather Review*, 136(4), 1523–1536.

Gillett, N. & Thompson, D. (2003). Simulation of recent Southern Hemisphere climate change. *Science*, 302(October), 273–276.

Gillett, N. P. (2015). Weighting climate model projections using observational constraints. *Philosophical transactions. Series A, Mathematical, physical, and engineering sciences*, 373(2054).

Gillett, N. P., Arora, V. K., Matthews, D., & Allen, M. R. (2013). Constraining the ratio of global warming to cumulative CO2 emissions using CMIP5 simulations. *Journal of Climate*, 26(18), 6844–6858.

Giorgetta, M. A., Jungclaus, J. H., Reick, C. H., Legutke, S., Bader, J., Böttinger, M., Brovkin, V., Crueger, T., Esch, M., Fieg, K., Glushak, K., Gayler, V., Haak, H., Hollweg, H.-D., Ilyina, T., Kinne, S., Kornblueh, L., Matei, D., Mauritsen, T., Mikolajewicz, U., Mueller, W., Notz, D., Pithan, F., Raddatz, T., Rast, S., Redler, R., Roeckner, E., Schmidt, H., Schnur, R., Segschneider, J., Six, K. D., Stockhause, M., Timmreck, C., Wegner, J., Widmann, H., Wieners, K.-H., Claussen, M., Marotzke, J., & Stevens, B. (2013). Climate and carbon cycle changes from 1850 to 2100 in MPI-ESM simulations for the coupled model intercomparison project phase 5. *Journal of Advances in Modeling Earth Systems*, 5(3), 572–597.

Gordon, N. D., Jonko, A. K., Forster, P. M., & Shell, K. M. (2013). An observationally based constraint on the water-vapor feedback. *Journal of Geophysical Research: Atmospheres*, 118(22), 12,435–12,443.

Gordon, N. D. & Klein, S. A. (2014). Low-cloud optical depth feedback in climate models. *Journal of Geophysical Research: Atmospheres*, 119(10), 6052–6065.

Graven, H. D., Keeling, R. F., Piper, S. C., Patra, P. K., Stephens, B. B., Wofsy, S. C., Welp, L. R., Sweeney, C., Tans, P. P., Kelley, J. J., Daube, B. C., Kort, E. A., Santoni, G. W., & Bent, J. D. (2013). Enhanced Seasonal Exchange of CO2 by Northern Ecosystems Since 1960. *Science*, 341(6150), 1085–1089.

Gray, J. M., Frolking, S., Kort, E. a., Ray, D. K., Kucharik, C. J., Ramankutty, N., & Friedl, M. a. (2014). Direct human influence on atmospheric CO2 seasonality from increased cropland productivity. *Nature*, 515(7527), 398–401.

Griffies, S. M., Harrison, M. J., Pacanowski, R. C., & Rosati, A. (2004). A Technical Guide to MOM4. GFDL Ocean Group Technical Report No. 5. *Princeton, NJ: NOAA/Geophysical Fluid Dynamics Laboratory*, (pp. 342 pp).

Grise, K. M. & Polvani, L. M. (2014). Southern Hemisphere Cloud-Dynamics Biases in CMIP5 Models and Their Implications for Climate Projections. *Journal of Climate*, 27(15), 6074–6092.

Gupta, A. S. & England, M. H. (2006). Coupled Ocean-Atmosphere-Ice Response to Variations in the Southern Annular Mode. *Journal of Climate*, 19(18), 4457–4486.

Haimberger, L., Tavolato, C., & Sperka, S. (2008). Toward Elimination of the Warm Bias in Historic Radiosonde Temperature Records-Some New Results from a Comprehensive Intercomparison of Upper-Air Data. *Journal of Climate*, 21(18), 4587–4606.

Haimberger, L., Tavolato, C., & Sperka, S. (2012). Homogenization of the Global Radiosonde Temperature Dataset through Combined Comparison with Reanalysis Background Series and Neighboring Stations. *Journal of Climate*, 25(23), 8108–8131.

Hall, A. & Qu, X. (2006). Using the current seasonal cycle to constrain snow albedo feedback in future climate change. *Geophysical Research Letters*, 33(3), 1–4.

Hassler, B., Bodeker, G. E., Cionni, I., & Dameris, M. (2009). A vertically resolved, monthly mean, ozone database from 1979 to 2100 for constraining global climate model simulations. *International Journal of Remote Sensing*, 30(15-16), 4009–4018.

Held, I. M. (2005). The Gap between Simulation and Understanding in Climate Modeling. *Bulletin of the American Meteorological Society*, 86(11), 1609–1614.

Hibbard, K. A., Meehl, G. A., Cox, P. M., & Friedlingstein, P. (2007). A strategy for climate change stabilization experiments. *Eos, Transactions American Geophysical Union*, 88(20), 217–221.

Hijioka, Y., Matsuoka, Y., Nishimoto, H., Masui, M., & Kainuma, M. (2008). Global GHG emissions scenarios under GHG concentration stabilization targets. *Journal of Global Environmental Engineering*, 13, 97–108.

Huang, P. & Ying, J. (2015). A Multimodel Ensemble Pattern Regression Method to Correct the Tropical Pacific SST Change Patterns under Global Warming. *Journal of Climate*, 28(12), 4706–4723.

Huber, M., Mahlstein, I., Wild, M., Fasullo, J., & Knutti, R. (2011). Constraints on climate sensitivity from radiation patterns in climate models. *Journal of Climate*, 24(4), 1034–1052.

Huntingford, C. & Cox, P. M. (2000). An analogue model to derive additional climate change scenarios from existing GCM simulations. *Climate dynamics*, 16(8), 575–586.

Huntingford, C., Zelazowski, P., Galbraith, D., Mercado, L. M., Sitch, S., Fisher, R., Lomas, M., Walker, A. P., Jones, C. D., Booth, B. B. B., Malhi, Y., Hemming, D., Kay, G., Good, P., Lewis, S. L., Phillips, O. L., Atkin, O. K., Lloyd, J., Gloor, E., Zaragoza-Castells, J., Meir, P., Betts, R., Harris, P. P., Nobre, C., Marengo, J., & Cox, P. M. (2013). Simulated resilience of tropical rainforests to CO2-induced climate change. *Nature Geoscience*, 6(4), 268–273.

Hurrell, J. W. (1995). Decadal trends in the north atlantic oscillation: regional temperatures and precipitation. *Science (New York, N.Y.)*, 269(5224), 676–679.

IPCC (2013). *Climate Change 2013 - The Physical Science Basis.* Cambridge University Press.

IPCC (2014). Summary for Policymakers. In T. Stocker, D. Qin, G.-K. Plattner, M. Tignor, S. Allen, J. Boschung, A. Nauels, Y. Xia, V. Bex, & P. Midgley (Eds.), *Climate Change 2013 - The Physical Science Basis. Contribution of Working Group I to the Fifth Assessment Report of the Intergonvernmental Panel on CLimate Change* chapter SPM, (pp. 1–30). Cambridge University Press.

Iversen, T., Bentsen, M., Bethke, I., Debernard, J. B., Kirkevåg, A., Seland, Ø., Drange, H., Kristjánsson, J. E., Medhaug, I., Sand, M., & Seierstad, I. a. (2012). The Norwegian Earth System Model, NorESM1-M - Part 2: Climate response and scenario projections. *Geoscientific Model Development Discussions*, 5(3), 2933–2998.

Jones, C. & Cox, P. (2005). On the significance of atmospheric CO2 growth rate anomalies in 2002-2003. *Geophysical research letters*, 32(14), 2001–2004.

Jung, M., Reichstein, M., Margolis, H. A., Cescatti, A., Richardson, A. D., Arain, M. A., Arneth, A., Bernhofer, C., Bonal, D., Chen, J., Gianelle, D., Gobron, N., Kiely, G., Kutsch, W., Lasslop, G., Law, B. E., Lindroth, A., Merbold, L., Montagnani, L., Moors, E. J., Papale, D., Sottocornola, M., Vaccari, F., & Williams, C. (2011). Global patterns of land-atmosphere fluxes of carbon dioxide, latent heat, and sensible heat derived from eddy covariance, satellite, and meteorological observations. *Journal of Geophysical Research*, 116, G00J07.

Jupp, T. E., Cox, P. M., Rammig, A., Thonicke, K., Lucht, W., & Cramer, W. (2010). Development of probability density functions for future South American rainfall. *New Phytologist*, 187(3), 682–693.

Kang, S. M., Polvani, L. M., Fyfe, J. C., & Sigmond, M. (2011). Impact of polar ozone depletion on subtropical precipitation. *Science (New York, N.Y.)*, 332(6032), 951–954.

Karpechko, A. Y., Maraun, D., & Eyring, V. (2013). Improving Antarctic Total Ozone Projections by a Process-Oriented Multiple Diagnostic Ensemble Regression. *Journal of the Atmospheric Sciences*, 70(12), 3959–3976.

Keeling, C., Whorf, T., Wahlen, M., & Plicht, J. (1995). Interannual extremes in the rate of rise of atmospheric carbon dioxide since 1980. *Nature*, 375(June), 666 – 670.

Keeling, C. D., Bacastow, R. B., Bainbridge, A. E., Ekdahl Jr., C. A., Guenther, P. R., Waterman, L. S., & Chin, J. F. S. (1976). Atmospheric carbon dioxide variations at Mauna Loa Observatory, Hawaii. *Tellus A.*

Keeling, C. D., Chin, J. F. S., & Whorf, T. P. (1996). Increased activity of northern vegetation inferred from atmospheric CO2 measurements. *Nature*, 382(11 July), 146–149.

Keeling, C. D., Piper, S. C., & Heimann, M. (1989). A three-dimensional model of atmospheric CO2 transport based on observed winds: 4. Mean annual gradients and interannual variations, in Aspects of Climate Variability in the Pacific and the Western Americas. *Geophys. Monogr. Ser.*, 55(AGU, Washington, D. C.), 305–363.

Kidston, J. & Gerber, E. P. (2010). Intermodel variability of the poleward shift of the austral jet stream in the CMIP3 integrations linked to biases in 20th century climatology. *Geophysical Research Letters*, 37(9).

Kirk-Davidoff, D. B. (2009). On the diagnosis of climate sensitivity using observations of fluctuation. *Atmos. Chem. Phys.*, (pp. 813–822).

Kirtman, B., Power, S., Adedoyin, J., Boer, G., Bojariu, R., Camilloni, I., Doblas-Reyes, F., Fiore, A., Kimoto, M., Meehl, G., Prather, M., Sarr, A., Schär, C., Sutton, R., van Oldenborgh, G., Vecchi, G., & Wang, H. (2013). Near-term Climate Change: Projections and Predictability. In P. Stocker, T.F. and Qin, D. and Plattner, G.-K. and Tignor, M. and Allen, S.K. and Boschung, J. and Nauels, A. and Xia, Y. and Bex, V. and Midgley (Ed.), *Climate Change 2013 - The Physical Science Basis* chapter 11, (pp. 953–1028). Cambridge: Cambridge University Press.

Klein, S. A. & Hall, A. (2015). Emergent Constraints for Cloud Feedbacks. *Current Climate Change Reports*.

Knight, J. R., Folland, C. K., & Scaife, A. a. (2006). Climate impacts of the Atlantic multidecadal oscillation. *Geophysical Research Letters*, 33(17), 2–5.

Knorr, W. (2000). Annual and interannual CO2 exchanges of the terrestrial biosphere: process-based simulations and uncertainties. *Global Ecology and Biogeography*, 9(3), 225–252.

Knutti, R., Abramiwitz, G., Collins, M., Eyring, V., Gleckler, P. J., Hewitson, B., & Mearns, L. (2010a). *Good Practice Guidance Paperon on Assessing and Combining Multi Model Climate Projections. In: Meeting Report of the IPCC Expert Meeting on Assessing and Combining Multi Model Climate Projections*. Technical report.

Knutti, R., Furrer, R., Tebaldi, C., Cermak, J., & Meehl, G. a. (2010b). Challenges in combining projections from multiple climate models. *Journal of Climate*, 23(10), 2739–2758.

Knutti, R., Masson, D., & Gettelman, A. (2013). Climate model genealogy: Generation CMIP5 and how we got there. *Geophysical Research Letters*, 40(6), 1194–1199.

Krinner, G. (2005). A dynamic global vegetation model for studies of the coupled atmosphere-biosphere system. *Global Biogeochemical Cycles*, 19(1), GB1015.

Kushner, P. & Polvani, L. (2004). Stratosphere-troposphere coupling in a relatively simple AGCM: The role of eddies. *Journal of climate*, (pp. 629–639).

Kushner, P. J., Held, I. M., & Delworth, T. L. (2001). Southern Hemisphere atmospheric circulation response to global warming. *Journal of Climate*, 14, 2238–2249.

Lawrence, D. M., Oleson, K. W., Flanner, M. G., Thornton, P. E., Swenson, S. C., Lawrence, P. J., Zeng, X., Yang, Z.-L., Levis, S., Sakaguchi, K., Bonan, G. B., & Slater, A. G. (2011). Parameterization improvements and functional and structural advances in Version 4 of the Community Land Model. *Journal of Advances in Modeling Earth Systems*, 3(3), M03001.

Le Quéré, C., Andres, R. J., Boden, T., Conway, T., Houghton, R. a., House, J. I., Marland, G., Peters, G. P., Van Der Werf, G. R., Ahlström, A., Andrew, R. M., Bopp, L., Canadell, J. G., Ciais, P., Doney, S. C., Enright, C., Friedlingstein, P., Huntingford, C., Jain, a. K., Jourdain, C., Kato, E., Keeling, R. F., Klein Goldewijk, K., Levis, S., Levy, P., Lomas, M., Poulter, B., Raupach, M. R., Schwinger, J., Sitch, S., Stocker, B. D., Viovy, N., Zaehle, S., & Zeng, N. (2013). The global carbon budget 1959-2011. *Earth System Science Data*, 5(1), 165–185.

Leakey, A. D. B., Ainsworth, E. a., Bernacchi, C. J., Rogers, A., Long, S. P., & Ort, D. R. (2009). Elevated CO2 effects on plant carbon, nitrogen, and water relations: six important lessons from FACE. *Journal of experimental botany*, 60(10), 2859–76.

Leith, C. (1975). Climate response and fluctuation dissipation. *Journal of the Atmospheric Sciences*, 32, 2022–2026.

Lenton, T. M., Held, H., Kriegler, E., Hall, J. W., Lucht, W., Rahmstorf, S., & Schellnhuber, H. J. (2008). Tipping elements in the Earth's climate system. *Proceedings of the National Academy of Sciences of the United States of America*, 105(6), 1786–93.

LeTreuth, H., Somerville, U., Cubasch, U., Ding, Y., Mauritzen, C., Mokssit, A., Peterson, T., & Prather, M. (2013). Historical Overview of Climate Change. In *he Physical Science Basis. Contribution of Working Group I to the Fourth Assessment Report of the Intergovernmental Panel on Climate Change* (pp. Solomon, S.,D. Quin, M.Manning, Z. Chen, M. Marqui). Cambridge, United Kingdom and New York, NY, USA: Cambridge University Press.

Li, L., Lin, P., Yu, Y., Wang, B., Zhou, T., Liu, L., Liu, J., Bao, Q., Xu, S., Huang, W., Xia, K., Pu, Y., Dong, L., Shen, S., Liu, Y., Hu, N., Liu, M., Sun, W., Shi, X., Zheng, W., Wu, B., Song, M., Liu, H., Zhang, X., Wu, G., Xue, W., Huang, X., Yang, G., Song, Z., & Qiao, F. (2013). The flexible global ocean-atmosphere-land system model, Grid-point Version 2: FGOALS-g2. *Advances in Atmospheric Sciences*, 30(3), 543–560.

Lintner, B. R., Buermann, W., Koven, C. D., & Fung, I. Y. (2006). Seasonal circulation and Mauna Loa CO_2 variability. *Journal of Geophysical Research: Atmospheres*, 111(13), 1–18.

Lorenz, D. J. & DeWeaver, E. T. (2007). Tropopause height and zonal wind response to global warming in the IPCC scenario integrations. *Journal of Geophysical Research: Atmospheres*, 112(10).

Lorenz, D. J. & Hartmann, D. L. (2001). Eddy-Zonal Flow Feedback in the Southern Hemisphere. *Journal of the Atmospheric Sciences*, 58(21), 3312–3327.

Mahlstein, I. & Knutti, R. (2010). Regional climate change patterns identified by cluster analysis. *Climate Dynamics*, 35(December 2008), 587–600.

Marshall, G. J. (2003). Trends in the Southern Annular Mode from Observations and Reanalyses. *Journal of Climate*, 16(24), 4134–4143.

Martin, G. M., Bellouin, N., Collins, W. J., Culverwell, I. D., Halloran, P. R., Hardiman, S. C., Hinton, T. J., Jones, C. D., McDonald, R. E., McLaren, A. J., O'Connor, F. M., Roberts, M. J., Rodriguez, J. M., Woodward, S., Best, M. J., Brooks, M. E., Brown, A. R., Butchart, N., Dearden, C., Derbyshire, S. H., Dharssi, I., Doutriaux-Boucher, M., Edwards, J. M., Falloon, P. D., Gedney, N., Gray, L. J., Hewitt, H. T., Hobson, M., Huddleston, M. R., Hughes, J., Ineson, S., Ingram, W. J., James, P. M., Johns, T. C., Johnson, C. E., Jones, A., Jones, C. P., Joshi, M. M., Keen, A. B., Liddicoat, S., Lock, A. P., Maidens, A. V., Manners, J. C., Milton, S. F., Rae, J. G. L., Ridley, J. K., Sellar, A., Senior, C. A., Totterdell, I. J., Verhoef, A., Vidale, P. L., & Wiltshire, A. (2011). The HadGEM2 family of Met Office Unified Model climate configurations. *Geoscientific Model Development*, 4(3), 723–757.

Massonnet, F., Fichefet, T., Goosse, H., Bitz, C. M., Philippon-Berthier, G., Holland, M. M., & Barriat, P. Y. (2012). Constraining projections of summer Arctic sea ice. *Cryosphere*, 6(6), 1383–1394.

McKinley, G. a., Takahashi, T., Buitenhuis, E., Chai, F., Christian, J. R., Doney, S. C., Jiang, M. S., Lindsay, K., Moore, J. K., Le Quéré, C., Lima, I., Murtugudde, R., Shi, L., & Wetzel, P. (2006). North Pacific carbon cycle response to climate variability on seasonal to decadal timescales. *Journal of Geophysical Research: Oceans*, 111, 1–22.

Meehl, G. A., Washington, W. M., Arblaster, J. M., Hu, A., Teng, H., Tebaldi, C., Sanderson, B. N., Lamarque, J.-F., Conley, A., Strand, W. G., & White, J. B. (2012). Climate System Response to External Forcings and Climate Change Projections in CCSM4. *Journal of Climate*, 25(11), 3661–3683.

Michaelsen, J. (1987). Cross-validation in statistical climate forecast models. *Jurnal of Aapplied Meteorologie*, (26), 1589 – 1600.

Moses, M. (2012). Biogeochemical cycles.

Moss, R. H., Edmonds, J. A., Hibbard, K. A., Manning, M. R., Rose, S. K., van Vuuren, D. P., Carter, T. R., Emori, S., Kainuma, M., Kram, T., Meehl, G. A., Mitchell, J. F. B., Nakicenovic, N., Riahi, K., Smith, S. J., Stouffer, R. J., Thomson, A. M., Weyant, J. P., & Wilbanks, T. J. (2010). The next generation of scenarios for climate change research and assessment. *Nature*, 463(7282), 747–756.

Myhre, G., Shindell, D., Breon, F.-M., Collins, W., Fuglestvedt, J., Huang, J., Koch, D., Lamarque, J.-F., Lee, D., Mendoza, B., Nakajima, T., Robock, A., Stephens, G., Takemura, T., & Zhang, H. (2013). Anthropogenic and Natural Radiative Forcing. In P. Stocker, T.F. and Qin, D. and Plattner, G.-K. and Tignor, M. and Allen, S.K. and Boschung, J. and Nauels, A. and Xia, Y. and Bex, V. and Midgley (Ed.), *Climate Change 2013 - The Physical Science Basis* chapter 8, (pp. 659–740). Cambridge University Press.

Naik, V., Horowitz, L. W., Fiore, A. M., Ginoux, P., Mao, J., Aghedo, A. M., & Levy, H. (2013). Impact of preindustrial to present-day changes in short-lived pollutant emissions on atmospheric composition and climate forcing. *Journal of Geophysical Research: Atmospheres*, 118(14), 8086–8110.

Nakicenovic, N., Davidson, O., Davis, G., Grübler, A., Kram, T., Rovere, E. L. L., Metz, B., Morita, T., Pepper, W., Pitcher, H., Sankovski, A., Shukla, P., Swart, R., Watson, R., & Dadi, Z. (2000). *Emissions Scenarios: Summary for Policymakers*. Technical report.

Norby, R. J., Delucia, E. H., Gielen, B., Calfapietra, C., Giardina, C. P., King, J. S., Ledford, J., McCarthy, H. R., Moore, D. J. P., Ceulemans, R., De Angelis, P., Finzi, A. C., Karnosky, D. F., Kubiske, M. E., Lukac, M., Pregitzer, K. S., Scarascia-Mugnozza, G. E., Schlesinger, W. H., & Oren, R. (2005). Forest response to elevated CO2 is conserved across a broad range of productivity. *Proceedings of the National Academy of Sciences of the United States of America*, 102(50), 18052–18056.

O'Gorman, P. (2012). Sensitivity of tropical precipitation extremes to climate change. *Nature Geoscience*, n/a(5), 697–700.

Orr, A., Bracegirdle, T. J., Hosking, J. S., Jung, T., Haigh, J. D., Phillips, T., & Feng, W. (2012). Possible Dynamical Mechanisms for Southern Hemisphere Climate Change due to the Ozone Hole. *Journal of the Atmospheric Sciences*, 69(10), 2917–2932.

Perlwitz, J., Pawson, S., Fogt, R. L., Nielsen, J. E., & Neff, W. D. (2008). Impact of stratospheric ozone hole recovery on Antarctic climate. *Geophysical Research Letters*, 35(8).

Phillips, A. S., Deser, C., & Fasullo, J. (2014). Evaluating Modes of Variability in Climate Models. *Eos, Transactions American Geophysical Union*, 95(49), 453–455.

Piao, S., Sitch, S., Ciais, P., Friedlingstein, P., Peylin, P., Wang, X., Ahlström, A., Anav, A., Canadell, J. G., Cong, N., Huntingford, C., Jung, M., Levis, S., Levy, P. E., Li, J., Lin, X., Lomas, M. R., Lu, M., Luo, Y., Ma, Y., Myneni, R. B., Poulter, B., Sun, Z., Wang, T., Viovy, N., Zaehle, S., & Zeng, N. (2013). Evaluation of terrestrial carbon cycle models for their response to climate variability and to CO2 trends. *Global Change Biology*.

Polvani, L. M., Previdi, M., & Deser, C. (2011). Large cancellation, due to ozone recovery, of future Southern Hemisphere atmospheric circulation trends. *Geophysical Research Letters*, 38(4), n/a–n/a.

Pritchard, H. D., Arthern, R. J., Vaughan, D. G., & Edwards, L. A. (2009). Extensive dynamic thinning on the margins of the Greenland and Antarctic ice sheets. *Nature*, 461(7266), 971–975.

Qu, X. & Hall, A. (2014). On the persistent spread in snow-albedo feedback. *Climate Dynamics*, 42(1-2), 69–81.

Raddatz, T. J., Reick, C. H., Knorr, W., Kattge, J., Roeckner, E., Schnur, R., Schnitzler, K. G., Wetzel, P., & Jungclaus, J. (2007). Will the tropical land biosphere dominate the climate-carbon cycle feedback during the twenty-first century? *Climate Dynamics*, 29(6), 565–574.

Räisänen, J. (2007). How reliable are climate models? 59(1), 2–29.

Räisänen, J., Ruokolainen, L., & Ylhäisi, J. (2010). Weighting of model results for improving best estimates of climate change. *Climate Dynamics*, 35(2), 407–422.

Rammig, A., Jupp, T., Thonicke, K., Tietjen, B., Heinke, J., Ostberg, S., Lucht, W., Cramer, W., & Cox, P. (2010). Estimating the risk of Amazonian forest dieback. *New Phytologist*, 187(3), 694–706.

Reichstein, M., Ciais, P., Papale, D., Valentini, R., Running, S., Viovy, N., Cramer, W., Granier, A., Ogée, J., Allard, V., Aubinet, M., Bernhofer, C., Buchmann, N., Carrara, A., Grünwald, T., Heimann, M., Heinesch, B., Knohl, A., Kutsch, W., Loustau, D., Manca, G., Matteucci, G., Miglietta, F., Ourcival, J. M., Pilegaard, K., Pumpanen, J., Rambal, S., Schaphoff, S., Seufert, G., Soussana, J. F., Sanz, M. J., Vesala, T., & Zhao, M. (2007). Reduction of ecosystem productivity and respiration during the European summer 2003 climate anomaly: A joint flux tower, remote sensing and modelling analysis. *Global Change Biology*, 13(3), 634–651.

Riahi, K., Gruebler, A., & N., N. (2007). cenarios of long-term socio-economic and environmental development under climate stabilization. *Technological Forecasting and Social Change*, 7(74), 887–935.

Ring, M. J. & Plumb, R. A. (2008). The Response of a Simplified GCM to Axisymmetric Forcings: Applicability of the Fluctuation-Dissipation Theorem. *Journal of the Atmospheric Sciences*, 65(12), 3880–3898.

Rotstayn, L. D., Jeffrey, S. J., Collier, M. A., Dravitzki, S. M., Hirst, A. C., Syktus, J. I., & Wong, K. K. (2012). Aerosol- and greenhouse gas-induced changes in summer rainfall and circulation in the Australasian region: a study using single-forcing climate simulations. *Atmospheric Chemistry and Physics*, 12(14), 6377–6404.

Russell, J. L. & Wallace, J. M. (2004). Annual carbon dioxide drawdown and the Northern Annular Mode. *Global Biogeochemical Cycles*, 18, 1–8.

Sanderson, B. M., Knutti, R., & Caldwell, P. (2015). A Representative Democracy to Reduce Interdependency in a Multimodel Ensemble. *Journal of Climate*, 28(13), 5171–5194.

Sansom, P. G., Stephenson, D. B., Ferro, C. a. T., Zappa, G., & Shaffrey, L. (2013). Simple uncertainty frameworks for selecting weighting schemes and interpreting multimodel ensemble climate change experiments. *Journal of Climate*, 26(12), 4017–4037.

Sato, H., Itoh, A., & Kohyama, T. C. A. C. D. C. N. P. (2007). SEIB-DGVM: A new Dynamic Global Vegetation Model using a spatially explicit individual-based approach. *EcologicalÂ Modelling*, 200(3-4), 279–307 ST – SEIB–DGVM: A new Dynamic Global Vege.

Schaller, N., Mahlstein, I., Cermak, J., & Knutti, R. (2011). Analyzing precipitation projections: A comparison of different approaches to climate model evaluation. *Journal of Geophysical Research*, 116(D10), D10118.

Schneising, O., Reuter, M., Buchwitz, M., Heymann, J., Bovensmann, H., & Burrows, J. P. (2014). Terrestrial carbon sink observed from space: variation of growth rates and seasonal cycle amplitudes in response to interannual surface temperature variability. *Atmospheric Chemistry and Physics*, 14(1), 133–141.

Shepherd, T. G. (2014). Atmospheric circulation as a source of uncertainty in climate change projections. *Nature Geoscience.*

Sherwood, S. C., Bony, S., & Dufresne, J.-L. (2014). Spread in model climate sensitivity traced to atmospheric convective mixing. *Nature*, 505, 37–42.

Sherwood, S. C., Meyer, C. L., Allen, R. J., & Titchner, H. A. (2008). Robust tropospheric warming revealed by iteratively homogenized radiosonde data. *Journal of Climate*, 21(20), 5336–5350.

Simpkins, G. R. & Karpechko, A. Y. (2012). Sensitivity of the southern annular mode to greenhouse gas emission scenarios. *Climate Dynamics*, 38(3-4), 563–572.

Simpson, I. R., Hitchcock, P., Shepherd, T. G., & Scinocca, J. F. (2013). Southern Annular Mode Dynamics in Observations and Models. Part I: The Influence of Climatological Zonal Wind Biases in a Comprehensive GCM. *Journal of Climate*, 26(11), 3953–3967.

Smith, S. & Wigley, T. (2006). Multi-Gas Forcing Stabilization with the MiniCAM. *Energy Journal*, (3), 373–391.

Smith, T. M., Reynolds, R. W., Peterson, T. C., & Lawrimore, J. (2008). Improvements to NOAA's Historical Merged Land & Ocean Surface Temperature Analysis. *Journal of Climate*, 21(10), 2283–2296.

Soden, B. J. & Vecchi, G. A. (2011). The vertical distribution of cloud feedback in coupled ocean-atmosphere models. *Geophysical Research Letters*, 38(12), n/a–n/a.

Son, S. W., Gerber, E. P., Perlwitz, J., Polvani, L. M., Gillett, N. P., Seo, K. H., Eyring, V., Shepherd, T. G., Waugh, D., Akiyoshi, H., Austin, J., Baumgaertner, A., Bekki, S., Braesicke, P., Brühl, C., Butchart, N., Chipperfield, M. P., Cugnet, D., Dameris, M., Dhomse, S., Frith, S., Garny, H., Garcia, R., Hardiman, S. C., Jöckel, P., Lamarque, J. F., Mancini, E., Marchand, M., Michou, M., Nakamura, T., Morgenstern, O., Pitari, G., Plummer, D. a., Pyle, J., Rozanov, E., Scinocca, J. F., Shibata, K., Smale, D., Teyssdre, H., Tian, W., & Yamashita, Y. (2010). Impact of stratospheric ozone on Southern Hemisphere circulation change: A multimodel assessment. *Journal of Geophysical Research: Atmospheres*, 115(19), D00M07.

Son, S.-W., Polvani, L. M., Waugh, D. W., Akiyoshi, H., Garcia, R., Kinnison, D., Pawson, S., Rozanov, E., Shepherd, T. G., & Shibata, K. (2008). The impact of stratospheric ozone recovery on the Southern Hemisphere westerly jet. *Science (New York, N.Y.)*, 320(5882), 1486–1489.

Stephenson, D. B., Collins, M., Rougier, J. C., & Chandler, R. E. (2012). Statistical problems in the probabilistic prediction of climate change. *Environmetrics*, 23(5), 364–372.

Stroeve, J. C., Kattsov, V., Barrett, A., Serreze, M., Pavlova, T., Holland, M., & Meier, W. N. (2012). Trends in Arctic sea ice extent from CMIP5, CMIP3 and observations. *Geophysical Research Letters*, 39(16), L16502.

Sundquist, E. T. (1986). Geologic analogs: Teir value and limitations in the carbon dioxide research. In J. R. T. Reichle & D. E. (Eds.), *The Changing Carbon Cycle* (pp. 371–402). New York: Springer-Verlag.

Swart, N. C. & Fyfe, J. C. (2012). Observed and simulated changes in the Southern Hemisphere surface westerly wind-stress. *Geophysical Research Letters*, 39(16).

Taylor, K. E., Stouffer, R. J., & Meehl, G. A. (2012). An overview of CMIP5 and the experiment design. *Bulletin of the American Meteorological Society*, 93(4), 485–498.

Thompson, D. W. J. & Solomon, S. (2002). Interpretation of recent Southern Hemisphere climate change. *Science (New York, N.Y.)*, 296(5569), 895–899.

Thompson, D. W. J., Solomon, S., Kushner, P. J., England, M. H., Grise, K. M., & Karoly, D. J. (2011). Signatures of the Antarctic ozone hole in Southern Hemisphere surface climate change. *Nature Geoscience*, 4(11), 741–749.

Thorne, P. W., Parker, D. E., Tett, S. F. B., Jones, P. D., McCarthy, M., Coleman, H., & Brohan, P. (2005). Revisiting radiosonde upper air temperatures from 1958 to 2002. *Journal of Geophysical Research D: Atmospheres*, 110(18), 1–17.

Thornton, P. E., Doney, S. C., Lindsay, K., Moore, J. K., Mahowald, N., Randerson, J. T., Fung, I., Lamarque, J.-F., Feddema, J. J., & Lee, Y.-H. (2009). Carbon-nitrogen interactions regulate climate-carbon cycle feedbacks: results from an atmosphere-ocean general circulation model. *Biogeosciences*, 6(10), 2099–2120.

Thornton, P. E., Lamarque, J. F., Rosenbloom, N. a., & Mahowald, N. M. (2007). Influence of carbon-nitrogen cycle coupling on land model response to CO2 fertilization and climate variability. *Global Biogeochemical Cycles*, 21(4), n/a–n/a.

Tian, B. (2015). Spread of model climate sensitivity linked to double-Intertropical Convergence Zone bias. *Geophysical Research Letters*, 42(10), 4133–4141.

van Vuuren, D., den Elzen, M., Lucas, P., Eickhout, B., Strengers, B., van Ruijven, B., Wonink, S., & van Houdt, R. (2007). Stabilizing greenhouse gas concentrations at low levels: an assessment of reduction strategies and costs. *Climatic Change*.

van Vuuren, D. P., Edmonds, J., Kainuma, M., Riahi, K., Thomson, A., Hibbard, K., Hurtt, G. C., Kram, T., Krey, V., Lamarque, J.-F., Masui, T., Meinshausen, M., Nakicenovic, N., Smith, S. J., & Rose, S. K. (2011). The representative concentration pathways: an overview. *Climatic Change*, 109(1-2), 5–31.

Verseghy, D. L., McFarlane, N. A., & Lazare, M. (1993). Class - A Canadian land surface scheme for GCMS, II. Vegetation model and coupled runs. *International Journal of Climatology*, 13(4), 347–370.

Vichi, M., Manzini, E., Fogli, P. G., Alessandri, A., Patara, L., Scoccimarro, E., Masina, S., & Navarra, A. (2011). Global and regional ocean carbon uptake and climate change: sensitivity to a substantial mitigation scenario. *Climate Dynamics*, 37(9-10), 1929–1947.

Voldoire, A., Sanchez-Gomez, E., Salas y Mélia, D., Decharme, B., Cassou, C., Sénési, S., Valcke, S., Beau, I., Alias, A., Chevallier, M., Déqué, M., Deshayes, J., Douville, H., Fernandez, E., Madec, G., Maisonnave, E., Moine, M.-P., Planton, S., Saint-Martin, D., Szopa, S., Tyteca, S., Alkama, R., Belamari, S., Braun, A., Coquart, L., & Chauvin, F. (2013). The CNRM-CM5.1 global climate model: description and basic evaluation. *Climate Dynamics*, 40(9-10), 2091–2121.

Volodin, E. M., Dianskii, N. A., & Gusev, A. V. (2010). Simulating present-day climate with the INMCM4.0 coupled model of the atmospheric and oceanic general circulations. *Izvestiya, Atmospheric and Oceanic Physics*, 46(4), 414–431.

von Storch, H. & Zwiers, F. W. (1999). *Statistical Analysis in Climate Research*.

Wallace, J. & Hobbs, P. (2006). *Atmospheric Science: An Introductory Survey*, volume 92.

Watanabe, S., Hajima, T., Sudo, K., Nagashima, T., Takemura, T., Okajima, H., Nozawa, T., Kawase, H., Abe, M., Yokohata, T., Ise, T., Sato, H., Kato, E., Takata, K., Emori, S., & Kawamiya, M. (2011). MIROC-ESM: model description and basic results of CMIP5-20c3m experiments. *Geoscientific Model Development Discussions*, 4(2), 1063–1128.

Waugh, D. W. & Eyring, V. (2008). Quantitative performance metrics for stratospheric-resolving chemistry-climate models. *Atmospheric Chemistry and Physics Discussions*, 8(3), 10873–10911.

Waugh, D. W., Primeau, F., Devries, T., & Holzer, M. (2013). Recent changes in the ventilation of the southern oceans. *Science (New York, N.Y.)*, 339(6119), 568–70.

Wenzel, S., Cox, P. M., Eyring, V., & Friedlingstein, P. (2014). Emergent constraints on climate-carbon cycle feedbacks in the CMIP5 Earth system models. *Journal of Geophysical Research: Biogeosciences*, 119(5), 794–807.

Wenzel, S., Cox, P. M., Eyring, V., & Friedlingstein, P. (2015). Changes in the Carbon Dioxide Seasonal Cycle Constrain Future Increases in the Land Carbon Sink. *Nature*, in review.

Wenzel, S., Eyring, V., Gerber, E. P., & Karpechko, A. Y. (2016). Constraining Future Summer Austral Jet Stream Positions in the CMIP5 Ensemble by Process-oriented Multiple Diagnostic Regression. *Journal of Climate*, (pp. 151106131957005).

Wilcox, L. J., Charlton-Perez, a. J., & Gray, L. J. (2012). Trends in Austral jet position in ensembles of high- and low-top CMIP5 models. *Journal of Geophysical Research: Atmospheres*, 117(13), 1–10.

Wise, M., Calvin, K., Thomson, A., Clarke, L., Bond-Lamberty, B., Sands, R., Smith, S., Janetos, A., & Edmonds, J. (2009). Implications of Limiting CO2 Concentrations for Land Use and Energy. *Science*, 29(324), 1183–1186.

Wu, T. W. (2012). A mass-flux cumulus parameterization scheme for large-scale models: Description and test with observations. *Clim. Dyn.*, 38(3-4), 725–744.

Yin, J. H. (2005). A consistent poleward shift of the storm tracks in simulations of 21st century climate. *Geophysical Research Letters*, 32(18), 1–4.

Young, P. J., Butler, A. H., Calvo, N., Haimberger, L., Kushner, P. J., Marsh, D. R., Randel, W. J., & Rosenlof, K. H. (2013). Agreement in late twentieth century southern hemisphere stratospheric temperature trends in observations and ccmval-2, CMIP3, and CMIP5 models. *Journal of Geophysical Research: Atmospheres*, 118(2), 605–613.

Yukimoto, S., Adachi, Y., Hosaka, M., SAKAMI, T., Yoshimura, H., Hirabara, M., Tanaka, T. Y., Shindo, E., Tsujino, H., Deushi, M., Mizuta, R., Yabu, S., Obata, A., Nakano, H., Koshiro, T., Ose, T., & Kitoh, A. (2012). A New Global Climate Model of the Meteorological Research Institute: MRI-CGCM3 ^|^mdash;Model Description and Basic Performance^|^mdash;. *Journal of the Meteorological Society of Japan*, 90A, 23–64.

Zaehle, S., Friend, A. D., Friedlingstein, P., Dentener, F., Peylin, P., & Schulz, M. (2010). Carbon and nitrogen cycle dynamics in the O-CN land surface model: 2. Role of the nitrogen cycle in the historical terrestrial carbon balance. *Global Biogeochemical Cycles*, 24(1), 1–14.

Zaehle, S., Medlyn, B. E., De Kauwe, M. G., Walker, A. P., Dietze, M. C., Hickler, T., Luo, Y., Wang, Y. P., El-Masri, B., Thornton, P., Jain, A., Wang, S., Warlind, D., Weng, E., Parton, W., Iversen, C. M., Gallet-Budynek, A., Mccarthy, H., Finzi, A., Hanson, P. J., Prentice, I. C., Oren, R., & Norby, R. J. (2014). Evaluation of 11 terrestrial carbon-nitrogen cycle models against observations from two temperate Free-Air CO2 Enrichment studies. *New Phytologist*, 202(3), 803–822.

Zahariev, K., Christian, J. R., & Denman, K. L. (2008). Preindustrial, historical, and fertilization simulations using a global ocean carbon model with new parameterizations of iron limitation, calcification, and N2 fixation. *Progress in Oceanography*, 77(1), 56–82.

Zeng, N., Zhao, F., Collatz, G. J., Kalnay, E., Salawitch, R. J., West, T. O., & Guanter, L. (2014). Agricultural Green Revolution as a driver of increasing atmospheric CO2 seasonal amplitude. *Nature*, 515(7527), 394–397.

Zhao, F. & Zeng, N. (2014). Continued increase in atmospheric CO_2 seasonal amplitude in the 21st century projected by the CMIP5 Earth system models. *Earth System Dynamics*, 5(2), 423–439.

Acknowledgments

First of all I would like to thank PD Dr Veronika Eyring, as my scientific supervisor and first evaluator, for giving me the possibility to write my PhD thesis in her group at the Deutsches Zentrum für Luft- und Raumfahrt (DLR), for her great support and helpful advice during my thesis. I would also like to thank her for giving me the opportunity to visit the University of Exeter during a three month stay and meet other great scientists during a number of conferences and workshops. I also would like to thank Prof George Craig for being my second evaluator.

I would like to thank Prof Pierre Friedlingstein, as my second scientific supervisor and Prof Peter Cox, for hosting me during many visits at the University of Exeter, for their advice on my thesis and especially for taking time to explain the mechanisms of the carbon cycle to me, which I greatly appreciate. Both I would like to thank for being my co-authors on the first two studies about emergent constraints on carbon cycle feedbacks presented in this work, for their great support and patience.

Furthermore, I would like to thank my co-authors from my third publication about emergent constraints on the future SH jet stream positions, Prof Edwin Gerber and Prof Alexey Y. Karpecko for their support and their great collaboration.

A special thanks goes to Dr Mattia Righi for his technical support with NCL and the ESMValTool and for helpful discussions. I also would like to thank Dr Axel Lauer for helpful discussion and his feedback on my work. I thank the whole Earth System Model Evaluation Group, under the lead of PD Dr Veronika Eyring, and the colleagues from the Earth System Model Department at the Institute of Atmospheric Physics for helpful discussions. I also would like to acknowledge Dr Chris Jones and Dr Eddy Robertson for providing me HadGEM-ES model data and giving me good advices on how to use it best; and Dr Viktor Brovkin for giving me advice on MPI-ESM-LR model data.

A very special thanks goes to my family and friends, for keeping me grounded and relieving me from any worries.

And last, I would like to thank Thorsten for everything.